Modeling and Multi-objective Optimization of a Photovoltaic-Thermal Based Multigeneration System

By

Hassan Rabbani

A Thesis Submitted as Partial Fulfillment
of the Requirements for the degree of Masters of Applied Science
in
Electrical and Computer Engineering

Faculty of Engineering and Applied Science
University of Ontario Institute of Technology

Oshawa, Ontario, Canada, 2015

Abstract

In this thesis, a novel multi generation integrated system is introduced, analyzed and optimized. It consists of GaAs based PV (Photo-Voltaic) arrays connected in series. Light is being concentrated on those arrays using lenses or mirrors. Concentrated light increases the cell temperature significantly. The cell is cooled down using a heat transfer fluid. This heat is being transferred to an organic Rankine cycle which not only produces electricity but also produces hot water for domestic applications. The organic Rankine cycle is also coupled with quadruple ammonia water absorption chiller. A part of the net electricity is used a PEM electrolyzer which produces hydrogen. So, using a single heat source, four useful commodities are produced, namely electricity, hot water, cooling, and hydrogen.

An integrated thermal model is developed to analyze this system. Five parameters, namely pressure in primary loop, pressure and temperature of organic Rankine cycle, pressure and temperature of ammonia water chiller system are varied in order to investigate their effects on energy and exergy efficiencies, cost of electricity, enviro economic parameter and on different exergoenvironmental factors. The results indicate that the PV array should be tilted at 30^o this will give maximum radiation intensity on the surface of PV array. I-V (Current and Volt) curves shows that increasing the radiation intensity increases both the current and voltage. For sake of analysis, the system is developed for Toronto, ON, Canada. At a concentration factor of 15 in a 100 cell PV array, 196.2 V and 8 A can be achieved at a radiation intensity of 1000 W/m^2. Similarly, increasing the radiation intensity can increase the cell temperature up to 700 K. The maximum calculated energy and exergy efficiencies are 46% and 40.5%, respectively.

Three objective functions are developed using the data obtained from parametric study namely exergy efficiency, cost of electricity ($/kWs) and exergoenvironmental impact coefficient. These objective functions were optimized using a genetic algorithm called NSGA-II. I have a multiple solutions which is called Pareto-front. The results shows that the optimum efficiency is 38.14%, optimum cost of coefficient of electricity is 13.4 cents/kWh and optimized exergoenvironmental impact coefficient is 2.6.

The multigeneration energy system discussed in this thesis and similar other alternatives (with renewable energy sources) can significantly contribute in addressing world energy needs and related challenges (e.g., human wealth, human welfare and environmental impact).

Keywords: Solar energy, Photovoltaics, PVT systems, Optimization, Energy, Exergy, Efficiency, Multigeneration, Cost assessment, Exergoeconomics, Exergoenvironmental analysis.

Acknowledgements

I would like to express my sincere gratitude to my supervisor Dr. Shahryar Rahnamayan and my co-supervisor Dr. Ibrahim Dincer for giving me this opportunity to work on this interesting project at UOIT. I also appreciate their unwavering guidance, steady encouragement and moral support throughout my graduate study.

I am also thankful to my parents and siblings for their constant encouragement and support throughout my Master's Degree. In addition, I would like to thank my elder brother Dr. Musharaf Rabbani for his kind attention and help throughout my research endeavours.

Furthermore, I would like to extend my gratitude to Ms. Amanda Hass for proofreading and editing my thesis.

Lastly, the financial support provided by Natural Sciences and Engineering Research Council of Canada (NSERC) is gratefully acknowledged.

Table of Contents

Table of Contents 5
List of Tables 8
List of Figures 9
Nomenclature 12
Greek Symbols 13
Chapter 1: Introduction 15
1.1 Overview 15
1.2 Objectives 19
1.3 Thesis Organization 21
Chapter 2: Literature Review 22
2.1 PV/T System 24
2.2 Absorption Chiller 28
2.3 PEM Electrolyzer 30
2.4 Optimization 31
2.4.1 Classical optimization 31
2.4.2 Numerical method optimization 32
2.4.4 Multi-objective optimization and Non-dominated sorted genetic algorithm (NSGA-II) 33
Chapter 3: System Description 39
3.1 System Details 39
3.1.1 Primary Loop 40
3.1.2 Secondary Loop 42
3.1.3 Cooling Loop 43
3.1.4 Hydrogen production 43
Chapter 4: System Modeling 45
4.1 System Modeling 46
4.1.1 Radiation Model 46
4.1.2 I-V Model 52
4.1.3 PVT Thermal Model 54

4.1.4 Thermodynamic Modeling 58
4.1.4.1 Thermodynamic Analysis 58
4.1.5 Exergoeconomic Modeling 65
4.1.6 Efficiency Analysis 69
4.1.7 Exergoenvironmental Modeling 70
4.1.7.1 Exergoenvironmental impact factor 70
4.1.7.2 Exergoenvironmental impact coefficient 70
4.1.7.3 Exergoenvironmental impact index 71
4.1.7.4 Exergoenvironmental impact improvement 71
4.1.7.5 Exergetic stability factor 71
4.1.7.6 Exergetic sustainability index 71
4.1.8 Evniroeconomic (environmental cost) analysis 72
4.1.8 Optimization 72
Chapter 5: Results and Discussion 77
5.1 Radiation Modeling Results 77
5.1.1 Radiation Intensity 77
5.1.2 Effect of Tilt Angle on Radiation Intensity 79
5.2 I-V Modeling Results 81
5.2.1 I-V Characteristic Curve 81
5.2.2 Effect of Solar Concentration and Radiation Intensity 82
5.2.3 Dynamic I-V Model 85
5.3 PVT Thermal Model Results 88
5.4 Thermodynamic Efficiency Analysis Results 90
5.4.1 Effect of Ambient Temperature 90
5.4.2 Effect of Pressure and Temperature of Secondary Cycle 91
5.4.3 Effect of Pressure of Absorption Chiller 93
5.5 Environmental Impact Accessibility Results 94
5.5.1 Effect of Ambient Temperature 95
5.5.2 Effect of Secondary Loop Pressure 95

5.6 Exergoeconomic and Enviroeconomics Results....96
5.6.1 Effect of Ambient Temperature....96
5.6.2 Effect of Pressure and Temperature of Secondary Cycle....97
5.6.3 Effect of Pressure of Absorption Chiller....99
5.7 Optimization Results....100
5.7.1 Sensitivity Analysis Results....106
Chapter 6: Conclusions and Recommendations....113
Reference....115

List of Tables

Table 2.1: NSGA-II Algorithm 36
Table 4.2: Typical values of β1 [74]. 49
Table 4.3: Typical values of ρg [74-76] 50
Table 4.4: GaAs Module Parameters 54
Table 4.5: Decision variable ranges (called box-constraints) 74
Table 4.6: Maximum acceptable difference for the objective function 75
Table 5.1: Calculated and/or assumed values for different parameters used in radiation modeling 78
Table 5.2: Optimized points of interest 101
Table 5.3: Thermodynamic characteristics of three different points on the Pareto frontier 103

List of Figures

Figure 1.1: World energy consumption by 2013 15
Figure 1.2: Heliostat based power plant 18
Figure 1.3: Parabolic trough based system 19
Figure 2.1: Cell structure for producing electricity and heat.....25
Figure 2.2: Flow chart representing different steps involved in NSGA-II optimization 34
Figure 2.3: NSGA-II Algorithm 35
Figure 3.1: Multi Commodities Energy System 42
Figure 5.1: Radiation intensity from 8:00 A.M to 4:00 P.M throughout the year in Toronto, ON, Canada, for a clear sky 80
Figure 5.2: Radiation intensity at different tilt angles 81
Figure 5.3: Radiation intensity at different tilt angles 81
Figure 5.4: Effect of radiation intensity on I-V characteristic of GaAs photovoltaics array. 82
Figure 5.5: Effect of radiation intensity and concentration factor on photovoltaic module output current. 83
Figure 5.6: Effect of radiation intensity and concentration factor on photovoltaic module output voltage. 83
Figure 5.7: Effect of radiation intensity and concentration factor on photovoltaic module maximum voltage. 84
Figure 5.8: Effect of radiation intensity and concentration factor on photovoltaic module maximum current. 84
Figure 5.9: Photovoltaic module voltage between 8:00 A.M to 4:00 P.M throughout the year for a clear sky. 86
. Figure 5.10: Photovoltaic module current between 8:00 A.M to 4:00 P.M throughout the year for a clear sky. 86
Figure 5.11: Photovoltaic maximum module voltage between 8:00 A.M to 4:00 P.M throughout the year for a clear sky. 87
Figure 5.12: Photovoltaic maximum module current between 8:00 A.M to 4:00 P.M throughout the year for a clear sky. 88
Figure 5.13: Effect of radiation intensity and concentration factor on cell temperature.....90

Figure 5.14: Temperature at the exit of PV arrays from 8:00 A.M to 4:00 P.M throughout the year. 91
Figure 5.15: Effect of ambient temperature on energy, exergy and network output (kW)..... 92
Figure 5.16: Effect of pressure of organic Rankine cycle on energy efficiency at different cycle temperatures……...93

Figure 5.17: Effect of pressure of organic Rankine cycle on exergy efficiency at different organic Rankine cycle temperatures……93

Figure 5.18: Effect of pressure of organic Rankine cycle on network output at different organic Rankine cycle temperatures. 93
Figure 5.19: Effect of pressure of the ammonia water quadruple absorption chiller on energy efficiency, exergy efficiency and network output..... 94
Figure 5.20: Effect of ambient temperature on exergoenvironmental impact factor, exergo environmental impact improvement and exergetic sustainability index..... 95
Figure 5.21: Effect of pressure of the ammonia water quadruple absorption chiller on exergo environmental impact factor, exergoenvironmental impact improvement and exergetic sustainability index. 96
Figure 5.22: Effect of ambient temperature on enviroeconomic parameter, cost coefficient of hydrogen and cost coefficient of network output……98

Figure 5.23: Effect of pressure of organic Rankine cycle on enviro economic parameter at different organic Rankine cycle temperatures. 98
Figure 5.24: Effect of pressure of organic Rankine cycle on network cost coefficient at different organic Rankine cycle temperatures. 100
Figure 5.25: Effect of pressure of the ammonia water quadruple absorption chiller on enviro economic parameter and cost coefficient of cold water……101

Figure 5.26: Results of all evaluations during 1400 generations using genetic algorithm. Exergy efficiency on x-axis, Electricity cost coefficient ($/kWh) on y-axis and exergoenvironmental impact coefficient on z-axis. 102
Figure 5.27: Pareto frontier solutions for exergy efficiency and cost coefficient of work..... 103

Figure 5.28: Pareto frontier solutions for exergoenvironmental impact factor and cost coefficient of work 103
Figure 5.29: Pareto frontier solutions for exergoenvironmental impact factor and exergy efficiency 104
Figure 5.30: Scattered distribution of decision variables with population in Pareto frontier for pressure in primary loop……..…105
Figure 5.31: Scattered distribution of decision variables with population in Pareto frontier for pressure in secondary loop 104
Figure 5.32: Scattered distribution of decision variables with population in Pareto frontier for temperature in secondary loop 105
Figure 5.33: Scattered distribution of decision variables with population in Pareto frontier for pressure in absorption chiller 105
Figure 5.34: Scattered distribution of decision variables with population in Pareto frontier for temperature in absorption chiller. 106
Figure 5.35 Effect of primary loop pressure on all three objective functions 107
Figure 5.36: Effect of secondary loop pressure on all three objective functions..... 108
Figure 5.37: Effect of secondary loop temperature on all three objective functions 109
Figure 5.38: Effect of absorption chiller pressure on all three objective functions 110
Figure 5.39: Effect of absorption chiller temperature on all three objective functions 110
Figure 5.40: Effect of variation of all five decision variables on all three objective functions.. 111

Nomenclature

A	Anode; Area (m^2)
$\dot{C}$	Cost rate ($/s)
$\dot{D}$	Diffuse irradiance (W/m^2)
E	Open circuit voltage (V); Eccentricity correction factor
ex	Specific exergy (kJ/kg)
$\dot{E}x$	Exergy rate (kW)
F	Faraday constant (sA/mol); Scattering fraction
$\dot{G}$	Gibbs free energy rate (kW)
g	Specific Gibbs free energy (kJ/kg)
$\dot{H}$	Enthalpy rate (kW)
h	Specific enthalpy (kJ/kg)
I	Current (A); Irradiance (W/m^2); Thickness of tadler photovoltaic (mm)
i	Current density (A/m^2)
K	Electrical conductivity ($ohm^{-1}m^{-1}$)
L	Distance (m)
m	Mass (kg)
$\dot{m}$	Mass flow rate (kg/s)
M	Molar mass (kg/kmol)
Mo	Molality (kmol/1,000kg water)
N	Number of levels; Day number in the year
n	Number of moles (kmol)
P	Pressure (kPa)
$\dot{Q}$	Heat transfer rate (kW)
R	Universal gas constant (kJ/kmol-K)
$\dot{S}$	Entropy rate (kW)
s	Specific entropy (kJ/kg-K)
t	Time (s)
T	Temperature (^oC)
$\bar{U}$	Molar internal energy (kJ/kmol)

u	Specific internal energy (kJ/kg)
v	Specific volume, m^3/kg
V	Visibility (km); voltage (V)
W	Water vapour thickness (cm)
X	Mass fraction
$\dot{Z}$	Equipment cost rate ($/s)

Subscripts and superscripts

A	Aerosols; Air mass at actual pressure
b	Beam
c	Forward scattering of total scattering
ch	Chemical
d	Diffuse
dew	Dew point
g	Generation
Ho	Heliostat
is	Horizontal
m-	Broadband
n	Normal
oz	Vertical ozone layer
o	Standard; reference state
PV	Photovoltaic
r	Rayleigh; air mass standard at local pressure
Reactor	Reactor
Ro	Rayleigh optical
sc	Solar constant (1367 W/m^2)
sol	Solution
xd	Destruction
$'$	Actual conditions

Greek Symbols

α	Solar angle (degrees)
Δ	Change

σ	Membrane thickness
σ	Stefan-Boltzmann constant ($5.67x10^{-8}$W m^{-2} K^{-4})
Ω	Morality (kmol/m^3)
λ	Wavelength (μm)
η	Efficiency
ϕ	Tilt angle
θ	Angle of incidence; angle between normal to surface (degrees)
θ_z	Zenith angle (degrees)
ρ_a	Albedo of the cloudless sky (dimensionless)
ρ_c	Albedo of cloud (dimensionless)
ρ_g	Albedo of ground (dimensionless)
β_1, β_2	Angstrom turbidity-parameters (dimensionless)
ρ	Density (kg/m^3)
Γ	Day angle (in radians)
δ	Declination, north positive (degrees)
δ_c	Declination of characteristics days, north positive (degrees)
τ	Scattering transmittances (dimensionless)
τ_{aa}	Transmittance of direct radiation due to aerosol absorptance (dimensionless)
τ_{as}	Transmittance of direct radiation due to aerosol scattering (dimensionless)
T	Temperature (^oC)
γ	Activity coefficient
ω	Hour angle, solar noon being zero and the morning is positive (degrees)
ω_1	Hour angle at the middle of an hour (degrees)
ω_o	Single-scattering albedo (dimensionless)
ω_s	Sunset-hour angle for a horizontal surface (degrees)
χ	Reflectivity of the ground
φ	Dummy variable
ζ	Tilt angle of a surface measured from the horizontal (degrees)
ψ	Latitude

Chapter 1: Introduction

1.1 Overview

Energy is directly related to our daily life. Nowadays, most of the electricity generation is from fossil fuels or from nuclear power plants. Power production from fossil and nuclear raises both ecological and safety risk and concerns, especially after nuclear power plant disaster in Japan. Demands for the green energy sources based co-generation systems are growing. The fast growing demands of energy over the past decades and getting in a proper and clean becomes challenging. In the past 50 years, demand has been increased tremendously. Even if the use of renewable energies triples over the next 25 years, the world is likely still to depend on fossil fuels for at least 50 percent of its energy need.

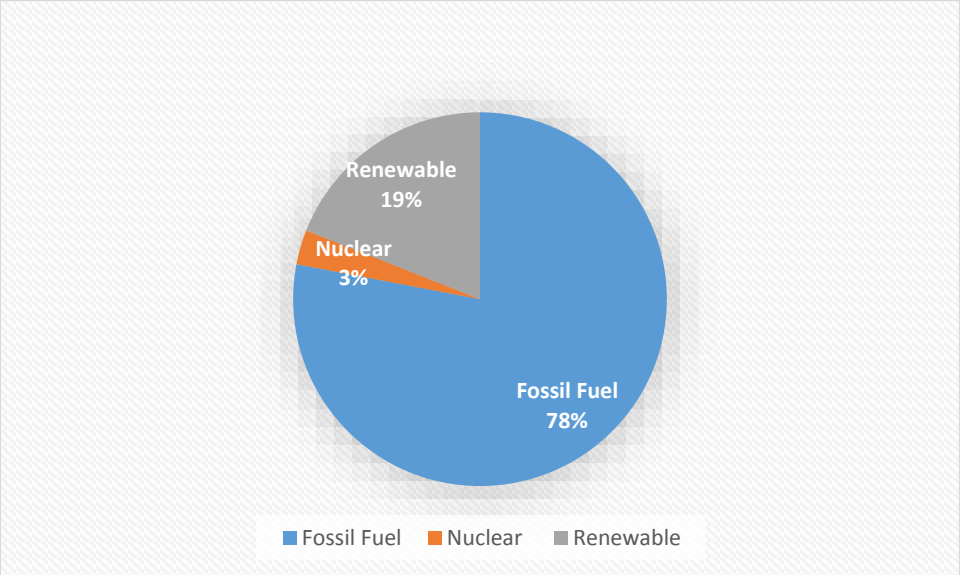

Figure 1.1: World energy consumption by 2013 (data from IEA [1]).

Figure 1.1 shows that most of the world energy is coming from hydrocarbons. As stated earlier, the problem with the hydrocarbon based fuels is that they produce carbon gases which are not environmentally benign.

The technology development has been enhanced up by introducing of multi generation energy systems. Energy is the basic part for many commercial and social activates nowadays. The use of fossil fuels with higher energy content has brought about massive growth and developments in the world. This industrial revolution started in the 18^{th} and 19^{th} centuries when the fuel evolution changed from wood to coal initially and then from coal to petroleum products in 20^{th} century.

Sustainable development is a process of developing land, cities, businesses, communities, etc. that "meet(s) the needs of the present time without effecting the ability of future peers to meet their own needs." When one kilogram of gasoline (a fossil fuel) is burned, it produces 3.2 kg of CO_2 and 1.0 kg of H_2O. The mining and burning of fossil fuels is the main threat to the environment. This is because of land damage, smog, acid rain and changes in the global environment temperature. Hydrocarbons have extraordinary value as the source of chemicals used to produce goods and other useful commodities, such as electricity, heat, cooling and hydrogen [2, 3].

According to the Biogenic Theory, dense energy fuels for example shale oil, coal, petroleum, and natural gas were formed because of high temperatures and pressure from biological remainders over millions of years. In our present time, hydrocarbons are not maintainable. This is because the majority of our societies use fossil fuels for number of different activities. It is important to note that large amounts of solar energy is stored in numerous forms of nature. In 1859, the commercial drilling of oil produced approximately 15-20 barrels of oil per day. Today, the oil industry is producing approximately 0.9 billion barrels of petroleum products per day while the demand is 105 barrels per day. With continuous increase in population, it is estimated that the petroleum production will reach 10 billion barrels within next 30 years.

Upon obtaining the petroleum products, the energy input for new oil extraction continues to surge. In some cases, 50% of the inherent energy in a barrel of oil is used required to obtain a barrel of represents. The total natural gas reserves is assessed to be about 1.4×10^{14} m^3 with production of an approximately 2.4×10^{12} m^3 annually. The fossil reserves are in reality depleted rapidly [2, 4]. The coal reserves is evaluated at 9.1×10^{11} tons and per year usage is projected to be 5×10^{9} tons. While it is predicted that the world has sufficient 'harvestable free' coal for energy use for approx. natural gas for 60 years, 250 years, nuclear fuel for another 200 years, the proverbial "devil" appears to be in the details upon consideration of rate of use of our economically recoverable reserves [3].

There is a drawback linked with hydrocarbon fuels and that is environmental pollution [2, 5]. In 1896, Arrhenius [6] showed concern that CO_2 production from petroleum products or other fossil fuels burning could increase the infrared opacity of the atmosphere enough to increase the temperature of the earth [7]. CO_2 is a greenhouse gas which traps long wavelength radiations (heat) emitted by earth. Hence, more carbon dioxide in the air, temperature of the atmosphere will

increase, and vice versa. Earth's baseline temperature at which living beings (especially humans) are comfortable with is finely balanced. Just a small tilt of earth in one direction and it is 90°F in Pennsylvania, tilt the earth in a similarly in opposite direction and it is 10°F in Pennsylvania (around twenty five years before the balance was approx.. 75°F to -10°F, but things are quite hot here now). Every year, around 6 billion tons of CO_2 is produced by human activities, 80% of which is due to the burning of fossil fuels. Coal produces approximately 430 grams of CO_2/kWh of energy, while natural gas produces 190 g of CO_2/kWh of energy. Current CO_2 level is measured and future level precisely forecasted by simple arithmetic: consuming so many tons of coal produces so many tons of carbon dioxide. In 18^{th} century, in start of the industrial revolution, the atmospheric CO_2 level was 270 ppm (the level which held steadily for millions of years). This level of CO_2 was increased to 370 ppm within the 20^{th} century and reached to 383 ppm in 2007 [3]. Different climate models predict that CO_2 level of 550 ppm would lead to a magnitude of warming equivalent to that of the cooling seen in the last ice age. So rather than an ice age, it seems we may soon have a 'steam age'. Similar to ice age, one may think that humans will continue to survive; however, one can also predict significant and unpleasant disruptions.

From 1990 to 2004, the world's carbon dioxide production increased by 24.4% [2, 8]. If current situation continues then we will easily and soon surpass 550 ppm of CO_2 in atm. - bringing rates well into the upper 600 ppm levels [2, 6].

As supply now surpasses demand, large-energy users are able to willingly meet energy requirements by means of importation of petroleum products. In the United States today, approximately 66% of the petroleum products consumed are imported from other countries; 66% of this oil consumption is spent on transportation, out of which 66%, used to enable cars and light trucks [9- 10].

The world's most respected body of climate scientists determined that approximately 55.85% decline in greenhouse gas emissions (specially CO_2) are essential to stabilize atmospheric concentrations of those gases [2, 10]. To eradicate anthropogenic carbon dioxide emissions, non-carbon-emitting energy sources are required. It is significant to mention that the earth receives 3×10^{24} joules/ year of solar energy. This is 10,000 times more than our present global energy demand. Furthermore, there is an abundant unused desert lands (19.2×10^6 km^2) [11] that would be ideally suitable for capturing solar energy in a sustainable way for the use of our society.

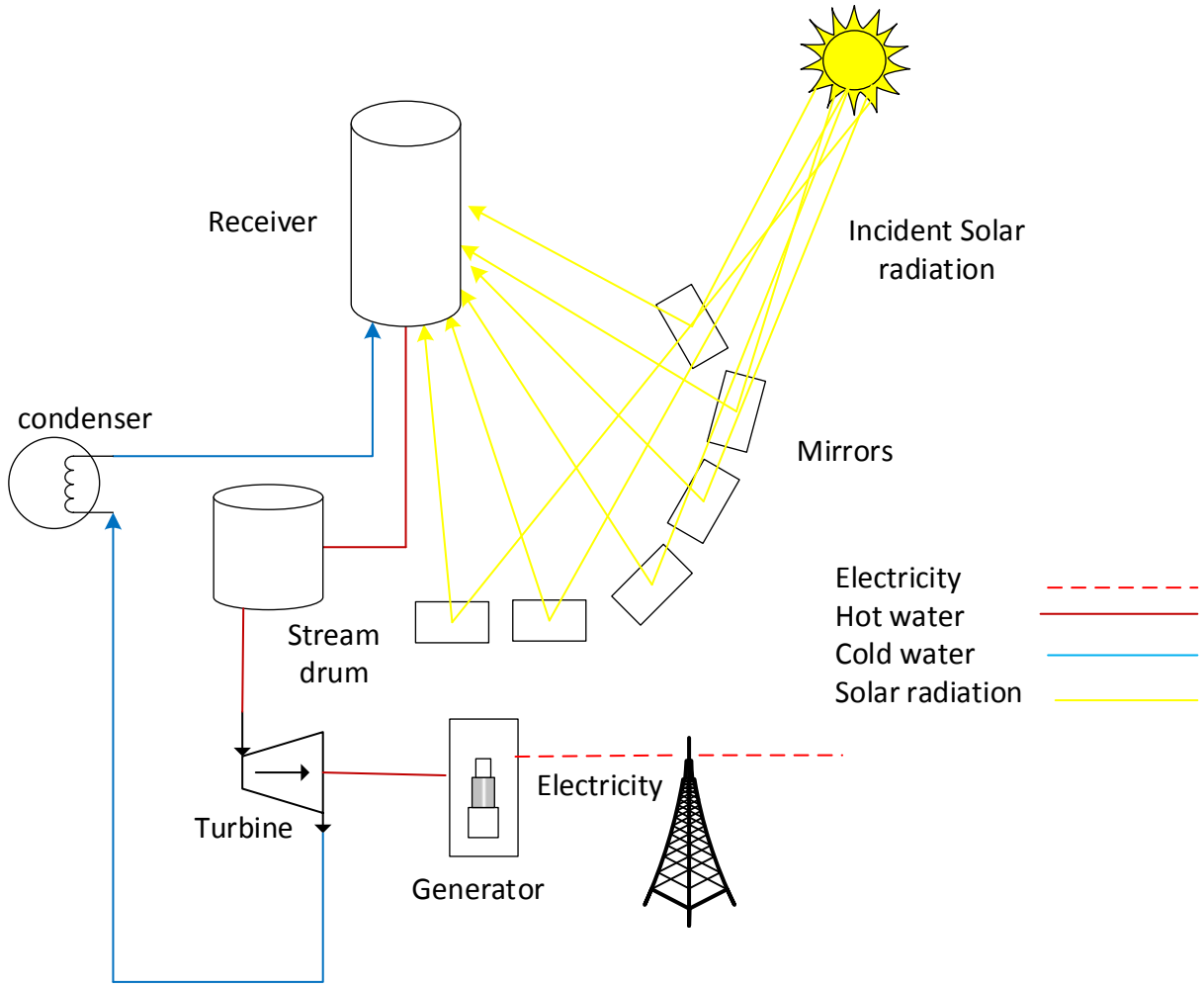

Figure 1.2: Heliostat based power plant

There are various sources of renewable energy which include but not limited to solar, wind, hydro and biomass. There are different ways by which energy can be harnessed from solar and converted into electricity and other different useful commodities. For example, using heliostat technology, in which light is reflected using number of different heliostats onto a tower. The concentrated solar irradiation then heat the molten salt which run the Rankine cycle and produce electricity. Figure 1.2 shows the heliostat based power plant.

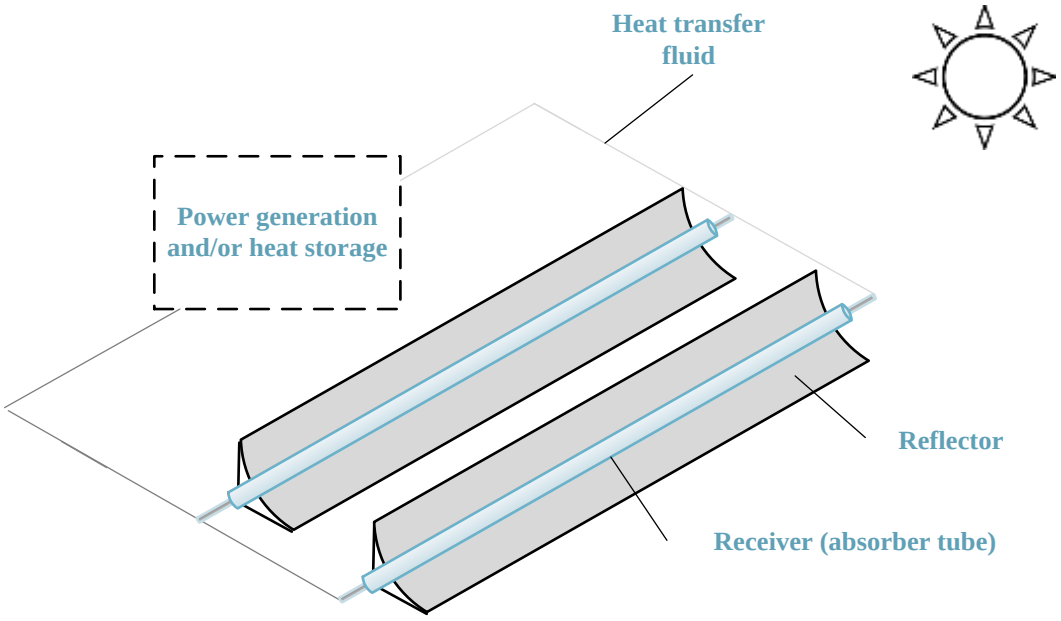

Figure 1.3: Parabolic trough based system

Another method of harnessing the solar energy is using parabolic collector's technology (PCT). In PCT, light is being concentrated on to the fluid using a parabolic solar collector. This concentrated solar irradiation heats up the fluid flowing through the collector tube. This heated fluid is then used to transfer heat to the water or organic fluid depending upon the type of cycle being used. Figure 1.3 shows the parabolic trough based system. Another process of harnessing the solar energy is by using PV panels. Recently a lot of research is focused on developing such solar panels which can withstand high temperatures. Generally silicon made PV cells are rated maximum for 1000W/m^2. As the intensity increases, it increases the cell temperature which results in decreasing in efficiency of the system. The efficiencies of the GaAs (Gallium Arsenide) cells are relatively high and very stable at cell temperatures and high irradiance intensity. This provides an alternative to the heliostat and parabolic dish technology.

1.2 Objectives

The main objective of this study is to design and optimize a multigeneration energy system which is able to produce electricity, heat, cooling, and hydrogen using a single input and without any significant environmental impact. In present research, a system is being developed which uses GaAs based PV cells. Light is being focused on the cells using mirrors and lenses. This increases the input light intensity on the cell surface and ultimately results high cell temperature. Therminoll-

66 is used to cool down the cell and extract the heat from the heated cell. It then transfer the heat to n-octane which is the working fluid for the organic Rankine cycle. The organic Rankine cycle produces heat, electricity and act as an input for the quadruple ammonia water chiller.

The analysis is carried out by using all the balance equations mass, energy, entropy and exergy and solve them using Engineering Equation Solver (EES) software. This software is a potential tool because of its large thermodynamic properties database of all the substances. For the optimization studies, the Matlab ® programming tool is used.

The specific objectives of this thesis research include the following studies.

a) Development of Radiation Model: As this is a solar based system, therefore it is necessary to predict solar irradiance at any given time. In present study the Iqbal model has been used to accurately predict solar irradiance anywhere in the world at any given time. For sake of analysis, the system is developed for Toronto, ON, Canada.
b) Development of I-V Model: This model is used to find the I-V characteristics of used solar panel used. The input of the models are solar irradiance and other manufacturing characters and this model can calculate how much power output is produced by the PV panel.
c) Development of PVT Thermal Model : As the light is been concentrated on the PV module which eventually is used to heat the working fluid, a PVT model is developed which predict the outlet temperature of the fluid coming out from series of PV modules.
d) Development of Thermodynamic Model: Based on 1^{st} and 2^{nd} law thermodynamic principles, this model presents the mass balance, energy balance, entropy balance and exergy balance across different system components. This model also helps us to find the effect of different processing conditions on system performance.
e) Development of Exergoeconomic Model: Based on 2^{nd} law analysis, exergoeconomic model presents cost of different streams by taking in account capital cost, interest rate, inflation rate and other different parameters.
f) Development of Performance Assessment: based on thermodynamic modeling and system boundary, energy and exergy efficiencies of the system are defined.
g) Development of Exergoenvironmental Analysis: Based on 2^{nd} law analysis different exergo environmental parameters are defined. These parameters actually represent the impact of system performance on environment.

h) Development of Enviroeconomic Analysis: This model represents cost of environmental impact of the PVT system when compared to an equivalent coal based system.

1.3 Thesis Organization

The thesis is organized the following five chapters:

Chapter 2 provides the necessary background and literature review. It initially discusses basic thermodynamic analysis followed by the PVT system, absorption chillers, PEM electrolyzer, and NSGA-II multi-objective optimization algorithm.

Chapter 3 provides detail modeling and analysis. It include radiation modeling, I-V model of the PV system, 1^{st} and 2^{nd} analysis of the each component and overall system, Efficiency analysis of the overall system, exergoenvironmental analysis and enviro-economics analysis.

Chapter 4 entails results and discussion.

Chapter 5 includes summary of the research and future recommendations.

Chapter 2: Literature Review

In this chapter, the background information related to energy and exergy analyses of different co-generation energy systems will be explained and discussed accordingly.

While designing an energy system it is important to consider those irreversibilities in the system. Higher values of irreversibilities lead to lower efficiency and lower performance of the system and vice-versa. There is no exist a reversible system. This basically means, there will always be irreversibilities in any energy system. The main objective of the designer should be minimization those irreversibilities. Second law of thermodynamics is also called law of exergy. Different researchers have done enormous work on energy and exergy analysis of different thermodynamic systems. Dincer and Rosen [12] studied various energy systems and showed that exergy analysis point out the locations where the most of the energy destruction takes place. Using this approach one can improve the operation of existing and new technologies. Hermann et al. [13] defined exergy as the theoretical maximum extractable work from energy resource.

Ganapathy et al. [14] performed exergy analysis of the 50 MW combined power plant (CPP) in India. He determined irreversibilities in different plant components and that major exergy loss take place in combustor. He also suggested number of modifications in combustor to minimize those losses. Orhan et al. [15] conducted the exergy analysis of three different fossil fuel based power plants. He also found that high exergy loss takes place in combustion chamber. Dincer et al. [16-22] also discussed the exergy analysis and sustainability of various systems in different processes and system components. They showed that different resources with different properties may exhibit different exergy at a given temperature and pressure. The difference can be physical, chemical and nuclear exergy. Sue et al. [23] have presented the application of exergy analysis of the gas turbine power generation system. His results show that exergy analysis is more accurate assessment of plant efficiency rather than energy analysis. They also discuss the relationship between pressure ratio and exergy destruction. They concluded that exergy destruction during combustion decreases by increasing the pressure ratio.

Gas turbine power plant with solid oxide fuel cell is studied by Haseli et al. [24]. Theis results showed that increase in the inlet temperature of compressor decrease both energy and exergy efficiencies for both conventional and with solid oxide fuel cell (SOFC) power plant. But

exergy efficiency of power plant with SOFC is improved 26.5%. Haungfu et al. [25] evaluated the performance of micro-scale building, cooling, heating and power (BCHP) with adsorption chiller under different conditions. His results show that there is a linear relationship between chiller capacity and the change in hot water inlet temperature. They verified his results with two different models. Tatiana et al. [26] analyzed the open gas turbine cycle exergetically. They also presented how to avoid the exergy destruction in different components of the system by adjusting processing parameters.

Ebrahimi et al. [27] conducted energy and exergy analyses of micro steam CCPH cycle for residential building. In order to provide the cooling load in the building, they used an ejector refrigeration system; his utilized Tri-generation energy system consists of steam turbine. His results show that major exergy destruction take place in the steam generator for summer and winter both seasons. Khaliq et al. [28] carried out exergy analysis of a tri-generation system. They have used gas turbine cycle, a single heat recovery steam generator for heating purpose and single effect LiBr absorption chiller to provide cooling. He find out the exergy destruction across the system component. He also find out energy and exergy efficiency of the system. The exergy analysis result shows that maximum exergy destruction takes place in the combustion chamber and steam generation process which makes 80% of the total exergy destruction. Tsatsaronis et al. [29] demonstrated how exergy related variable reduced the cost. These variable include but not limited to exergy efficiency, rates of exergy destruction, exergy loss, exergy destruction ratio, cost rate associated with exergy destruction, capital investment, operating and maintenance costs, relative cost difference of unit costs and exergoeconomic factor.

Dincer and Rosen [30] detailed the difference between energy and exergy and also drew the boundary between them. They also suggested that exergy analysis gives us more information about the system, when compared to energy analysis, and one can understand the system and their performance in a better way by considering exergy. Exergy analysis deals with both irreversibilities, internal and external, and also gives idea about how to improve the system. Gao et al. [31] performed exergy analysis on coal base multigeneration system for power and chemical production. His results show improvement in efficiency and cost when compared to individual systems. He also indicated around 3.9% cost saving when both power and chemical process are combined. Gao states that the “synthesis on the basis of thermal energy cascade utilization is the

main contribution to the performance benefit of the polygeneration system". Moreover the cascade utilization of chemical exergy is important for multigeneration system. Azouma et al. [32] showed from their calculations that exergy analysis and gas emission analysis are necessary to accommodate the environmental concern and engine efficiency. Therefore, exergetic efficiency takes into account not only by considering the quantity but also quality of energy flows.

2.1 PV/T System

Photovoltaic (PV) cells are used to produce electricity with no carbon emissions during their operational life. Mainly, PV cells are made with silicon which absorb a certain part of the incoming solar radiation. The absorbed energy is high enough to push the electron from valance band to conduction band. This free electron then travels through the circuit/load. Due to the flow of electrons electricity is generated. Due to the large gap between valance and conduction band, only low wavelength and high energy portion of the incident energy is utilized. Earth receive solar radiations in range of 280 nm to 4000 nm. While the energy of high wavelength portion is not high enough to excite the electron or to push the electron to its conduction band. Silicon PV cells usually work between 280 nm to 1100 nm. This reduces the efficiency of the cells. To date average efficiency of the PV cell is around 12 %.

In order to consider different materials with smaller band gap, silicon is under investigation for construction of PV cells. GaAs is one of the candidate materials. The costs of those materials are comparatively higher than silicon cells. Alta devices (a GaAs solar cell manufacturer) have reported an efficiency of 28.8% at STC (at 25^{o}C and at a solar radiation of 1000 W/m^{2}). Increasing the radiation intensity increases the short circuit current and decreases the open circuit voltage of the cell. Because of increase in temperature of the cell, overall production efficiency decreases with increase in solar radiation.

The heat travels through different layers of the cell and increases its temperature. This heat can be used to heat-up the fluid and use it for domestic heating application for combined heat and electricity production. This boost up the thermal efficiency of the system. Such system are refereed as PV/T system.

It has been proposed to convert solar energy to heat and then use this heat to generate steam and run a Rankine power plant to produce mechanical work output. This mechanical work output

can then be converted into electricity using an electrical generator. Due to the high cost of production, it has been proposed to concentrated solar radiation using lenses or mirrors to the PV panel. Resulting high power density makes it is difficult to remove heat from previously used silicon cells. This results in ubrupt reduction in performance as the efficiency of the silicon cells decreases abruptly with increase in cell temperature. GaAs is an alternative and a potential solution for that problem. It maintains a good conversation efficiency even at high cell temperature. Bell et al. [23] studied a system in which light is been focused on GaAs cells using lenses. This increased the cell temperature which were extracted by a heat transfer fluid. This heat transfer fluid then produced steam and run a small Rankine cycle. There was about 4% efficiency loss because of high temperature of the cell. However, this loss of efficiency compared to the efficiency gained due to the power output from the Rankine cycle.

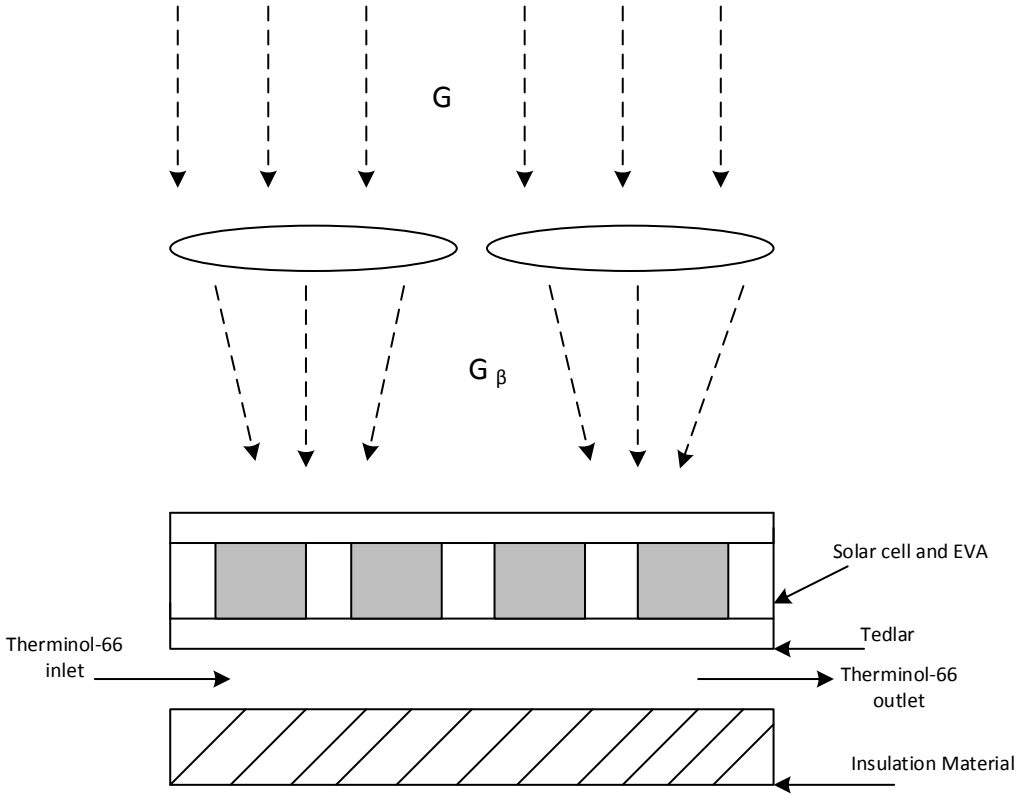

Figure 2.1: Cell structure for producing electricity and heat

Figure 2.1 shows a PV/T system in which solar radiation (G) is being focused using lenses (Gβ) on to a GaAs cell. Heat travels through different layers of the cell and heat-up the heat transfer fluid (Therminol-66 as shown below). This heat gained by the fluid can later on be used to produce

steam and eventually run a Rankine or organic Rankine cycle, depending upon temperature difference.

Many researchers have extensively worked on PV/T modeling and design and have addressed different areas of this field. For example, Sarhaddi, et al. performed exergetic optimization of solar photovoltaic thermal air collector [33]. Different thermal and electrical parameters of PV/T air collector which were considered in their study, including inlet, outlet, back surface temperature, maximum power point tracking. They have performed exergetic optimization under various climatic, operating and design parameters and presented the optimized value of inlet air velocity, duct length. Their results also show that with the increase in cell temperature the electrical efficiency has been reduced. It is necessary to reduce the surface temperature of PV/T using a coolant. Usually a coolant flows from the back surface of PV/T and take that heat out of PV/T. In this way, the cell surface temperature can be kept at a certain level and maximum efficiency can be achieved. Various coolant has been used, according to the system requirement. In early 1970, Wolf [34] presented the concept of PV/T collector. He used water or air as a coolant.

Joshi and Tiwari [35] conducted the energy and exergy analysis of PV/T parallel-plate air collector for the cold climate region of India (in Srinagar). They calculated the energy and exergy efficiencies of the collector which varies between 55-56% and 12-15%, respectively.

Joshi et al. [36] also compared the glass-to-glass and glass-to-tedlar PV/T air collectors. Their result show that the thermal performance of glass-to-glass air collector is better than glass-to-tedlar collector. This is due to better thermal conduction between glass-to-glass when compared to glass-to-tedlar. They also suggested that the exergy efficiency of a PV/T air collector is parametrically depended on its energy analysis.

Dubey et al. [37] calculated both energetic and exergatic performance of PV/T air collector duct. They have tested the PV/T panel in all weather conditions and calculated the effect of design and operating parameters on the PV/T panel performance. The parametric study which they have conducted showed that the thermal and electrical outputs increase with increase in absorber length, air mass flow rate and packing factor, but decrease with increased duct depth. They generated electricity form the PV module to drive the DC circulation pump.

Sarhaddi et al. [38-39] performed first and second law analysis on PV/T array and studied different thermal and electrical parameters. Bergene and Lovvik [40] carried out a detail study on flat-plate PV/T collector system for performance evaluation. The main motivation for their work is that solar cells act as good heat collectors and are fairly good selective absorbers. Additionally, in general solar cells increase their efficiency when heat is drawn from the cells. The model which they devloped is based on an analysis of heat transfer due to conduction, convection, and radiation and predicts the amount of heat that can be drawn from the system as well as the (temperature-dependent) power output.

Agarwal and Garg [41] performed ttheoretical study of a solar hybrid system. They have performed simulations for different water (coolant) masses in the tank and also for different amounts of water withdrawn at different times. The cell efficiency increases slightly with the increase in water mass. It is shown that domestic hybrid solar water heaters (area > 2 m^2) can generate sufficient electrical energy round the year to run tube lights, television etc. for 5–6 h during the night.

Chow et al. [42, 43] performed computer modeling and experimental validation of a building-integrated photovoltaic and water heating system. They developed numerical model based on the finite difference control volume approach. The integrated use of energy balance and fluid flow analysis allows the prediction of the system dynamic behavior under external excitations such as changes in weather, water consumption and make-up conditions. They validated the results of the modeling by comparing its predicted operating temperature changes and system daily efficiencies with the measured data acquired from an experimental rig at the City University of Hong Kong. The predictions from the model show good compliance with the experimental measurements.

Anderson et al. [44] studied the performance of a building integrated photovoltaic/thermal (BIPVT) solar collector. His results showed that key design parameters such as the fin efficiency, the thermal conductivity between the PV cells and their supporting structure, and the lamination method had a significant influence on both the electrical and thermal efficiency of the BIPVT. Furthermore, it was shown that the BIPVT could be made of lower cost materials, such as pre-coated color steel, without significant decreases in efficiency.

Ji et al. [45-46] performed thermal analysis of PV/T evaporator of a solar-assisted heat pump. Their results showed that the PV/T evaporator had an overall efficiency in the range of 0.64–0.87, thermal efficiency 0.53–0.64 and PV efficiency 0.124–0.135. Rosell et al. [47] have discussed design and simulation of a low concentrating photovoltaic/thermal system. They proposed an analytical model to simulate the thermal behavior and validated it with experimental results. The main novelty of their work is actually coupling of a linear Fresnel concentrator with a channel photovoltaic/thermal collector. Measured thermal performance of the solar system gives values above 60%. Their theoretical analysis confirms that thermal conduction between the PV cells and the absorber plate is a critical parameter. A similar type of model was built in Australia [48] where the concentration ratio is 37 times more on silicon cells bonded to an aluminum receiver. Electrical efficiency of the model was recorded 20%, respectively.

Sandnes and Rekstad [49] studied PV/T collector with polymer thermal absorber pasted on silicon cells collector. They compared thermal efficiencies of different collectors. Zakherchenko et al. [50] discussed hybrid PV–thermal system, with the photovoltaic panel (PVP) area much smaller than that of the solar collector. Their conclusion is that the PVP for application in a hybrid system needs a special design providing efficient heat extraction from it. Its study has shown that this design provides the high electrical and thermal efficiency of the hybrid system. They also point out that collector area should be larger than absorber. Efficiency can also be improved by increasing the long wave length absorption. Solar absorptance of the solar cells is significantly lower than of a black absorptance (with absorptance =0.95). Santbergen et al. [51] considered that by following methods one can increase the wavelength absorptance i) to use semi-transparent solar cells followed by a second absorber ii) To increase the amount of long wavelength irradiance that is absorbed in the back contact of the solar cell. Their simulation results indicates that overall absorption of first and second method is 0.87 and 0.85, respectively.

2.2 Absorption Chiller

Absorption chiller (AC) is used to provide cooling effect. It consist of four basic components namely pressuring unit (compressor or pump), condenser to remove heat gained during the pressuring step, expansion valve and evaporator. The working fluid is expanded by reducing its pressure in expansion valve which reduces its temperature and pressure both. This low temperature fluid is then used to cool the air/water (depending up on where it is used) in the evaporator. So net

heat transfer in evaporator basically defines the capacity of the cooling device. Traditionally, compressor along with refrigerants' are being used to provide cooling. One common example of this setup is air condition units installed in homes. However, this process is very energy extensive and the refrigerants' used in that process is not very environmentally benign. It is relatively less energy extensive to pressurize a liquid than gas. Considering this fact and environmental aspects different solutions have been proposed in literature to be used in chiller instead of refrigerants'. One of the most commonly used solution is ammonia water solution. Ammonia is the main working fluid while water act as a carrier fluid. The liquid solution is pumped, using a pump, to the generator where a heat source heats up the solution. Due to this ammonia is heated up and converted into its gases form. While water is returned to the absorber. The vaporized high temperature ammonia then passes through a condenser where its temperature is reduced and expanded eventually in an expansion valve. Due to expansion, the temperature and pressure of the ammonia reduces significantly. This low temperature ammonia gas then passes through evaporator where it exchange heat with the other fluid that needs to be cooled. After evaporator ammonia enters into the absorber where it mixes with that water is returned from generator and form again a solution of ammonia water.

The researchers have extensively addressed different aspects of absorption chillers. Chua et al. [52] performed thermodynamic modeling of an ammonia–water absorption chiller. Kim et al. [53] performed dynamic simulation of a single-effect ammonia–water absorption chiller. Their modeling is based on the continuity of species constituting the ammonia–water mixture and the conservation of energy for each component of the absorption chiller. Ordinary differential equations governing the response of each component and the algebraic equations describing the constitutive relation are solved in parallel by numerical integration. Their model has been applied to a commercially available 10.5 kW absorption chiller to study the transients of temperature, pressure, concentration, and void fraction of each component during the start-up operation. They have also investigated time constant of the absorption chiller. They have considered the effect of different parameters namely the bulk concentration of the ammonia–water solution, the mass of the solution filled, and the volumes of key components of the absorption chiller on chiller capacity. Lostec et al. [54] have performed simulation of ammonia water absorption chiller. They modeled heat and mass transfers in the absorber, the condensation of binary vapor of ammonia–water in the condenser and a thermosyphon desorber placed under the purification column. The results of their

model was compared and validated with experimental data obtained with a solar absorption chiller. The calculated results agree well with experimental data. Simulations based on experimental data were used to predict the temperature and concentration profiles in each heat exchanger. They concluded that COP decreases by 25% with a decrease of 10 °C in evaporator temperature and the COP increases by 4% with an increase of 10 °C in desorber temperature.

Ezzine et al. [55] conducted 1st and 2nd law analysis on solar absorption double effect chiller. Their results indicated that the absorber, solution heat exchangers, and condenser have the most potential to improve chiller energy efficiency. Lostec et al. [56] experimentally investigated ammonia-water chiller. Their results show that the performance of the absorption chiller decreases significantly with the evaporator temperature. This is due to a problem of partial evaporation in the evaporator when the absorption machine is operated outside its design specifications. Cooling capacity oscillations, caused by refrigerant expansion control, were also observed. Absorption chiller performance is also influenced by heat source temperature, cooling temperatures and flow of the rich solution. Wu et. al. [57] presented overview of absorption-chillers and heat pumps. Their findings state that in subfreezing refrigeration, the evaporation temperatures for single-stage absorption is mainly between −30 °C and −5 °C, and they can reach as low as −70 °C in advanced absorption systems. Air-source and ground-source absorption heat pumps are suggested for heating/domestic hot water applications in cold regions. For renewable energy uses, ammonia-based solar absorption applications with various working fluids are quite popular, whereas geothermal and biomass energy systems are less studied. In thermal energy storage, ammonia-based working fluids are not advantageous for storage capacity or cycle efficiency, but they prevail for subfreezing energy storage. Additionally, ammonia-based fluids are also attractive options for the miniaturization of absorption systems due to the absence of crystallization.

2.3 PEM Electrolyzer

PEM stands for polymer exchange membrane. PEM electrolyzer consist of two electrodes seprated by a polymer membrane which is mostly made up of Nafion. At anode, water is being oxidized to oxygen gas and proton travel through the membrane. This protons at cathode gets electrons and reduced into hydrogen gas. The electrolyzer requires electrical work (electricity) as an input. Typically, PEM electrolyzers have high production efficiency (above 80%). It is commonly used in industry for hydrogen production [58]. Ni et al. [59] have performed energy and exergy analysis

of PEM water electrolysis system. They have investigated heat production in the PEM cell due to irreversible losses and they compared with the thermal energy demand of PEM cell. Their results shows that the PEM electrolyzer normally operates in an exothermic mode as the heat production due to overpotentials exceeds the thermal energy demand. As the electrical energy input dominates the overall energy input, the exergy efficiency is about the same as the energy efficiency. Their study has quantified how much the energy efficiency can be decreased by increasing the operating temperature, lowering the current density, reducing the electrolyte thickness, and increasing the electrode catalytic activity.

Ahmadi et al. [60] presented energy and exergy analyses of hydrogen production via solar-boosted ocean thermal energy conversion and PEM electrolysis. Their results showed that the exergy efficiency of the PEM electrolyzer is about 56.5% for a hydrogen production rate of 1.2 kg/h. Ratlamwala et al. [61] performed energy and exergy analyses and optimization study of an integrated solar heliostat field system for hydrogen production. They have used PEM electrolyzer for hydrogen production. Their results show that the power and rate of generated hydrogen increase with increase in the heliostat field area and the solar flux. The rate of generated hydrogen increases from 0.006 kg/s to 0.063 kg/s with increase in the heliostat field area from 8000 m^2 to 50,000 m^2. Moreover, when the solar flux is increased from 400 W/m^2 to 1200 W/m^2, the rate of generated hydrogen increases from 0.005 kg/s to 0.018 kg/s. The optimization study yields maximum energy and exergy efficiencies and the rate of generated hydrogen of 18.74%, 39.55% and 1571 L/s, respectively. Multi-objective optimization have a set of solution not a single solution.

2.4 Optimization

In this section different optimization will be briefly defined and discussed. In the end Non-dominated sorted genetic algorithm (NSGA-II) will be discussed in detail.

2.4.1 Classical optimization

The classical optimization techniques are used to find the optimal solution of continuous and differentiable functions. They are single solution based methods. Some of the specifications of the classical optimization methods are as follow:

- Classical optimization mainly uses gradient information while locating the optimum solution.

- As these methods are mostly applicable to continuous and/or differentiable objective functions, so they are not mostly adopted for practical applications.
- One of the major assumption in these methods are that the derivatives of the objective functions are continuous and the objective functions are differentiable twice.

For multi-objective optimization, they can find a single Pareto-front (PF)solution in each run, and all other runs would be independent. Generally speaking, they have difficulty to find PF set, especially for concave Pareto-fronts.

2.4.2 Numerical method optimization

The numerical optimization can be characterized according to the method. These methods includes:

- Linear programming: Linear programming optimization deals with the linear objective functions. In linear programming, the constraints are defined only in form of linear equalities and inequalities.
- Integer programming: Integer programming deals with such linear objective functions which all the variables or part of them are constrained to take integer values as an input.
- Quadratic programming: Quadratic programming can optimize those objective functions which have quadratic terms. However, the constraints must be linear.
- Nonlinear programming: Nonlinear programming is used to optimize non-linear objective functions. It can also solve non-linear constraints.
- Stochastic programming: This kind of optimization deals with those objective functions whose constraints are dependent on random variable generation.
- Dynamic programming: In dynamic programming, the objective functions are divided in to set of small tasks which are inter related. This is mostly used to solve complex problems.
- Evolutionary algorithm: Evolutionary algorithms are based on biological operations, namely, selection, crossover/recombination, and mutation.

In this thesis, all the Pareto-front (PF) solutions (a set of optimal non-dominated solutions) are required. This is to conduct a sensitivity analysis on PF solutions and also to make a decision to select a robust solution from the set of solutions. Classical optimization methods are based on a single- solution and are not good candidates for the problem under consideration.

2.4.4 Multi-objective optimization and Non-dominated sorted genetic algorithm (NSGA-II)

Objective function for an optimization problem is a mathematical expression which needs to be optimized (maximized or minimized) in terms of input design variables. There may be more than one objective that needs to be optimized called multi-objective. Often multi-objectives are conflicting in nature (i.e. improving one degrades other one).For example in a power plant it is desirable to find such operating conditions which maximize plant efficiency but minimize its operating cost and environmental impact. Those problems which require more than one objective to be optimized are called as "Multi-objective optimization". Among different methods presented in literature, the NSGA-II is one of the most widely used method to optimize two different objectives.

A solution is called non-dominated, Pareto optimal, Pareto efficient or non-inferior, if none of the objective functions can be improved in value without degrading some of the other objective values.In NSGA-II, an initial random population is generated, P_0 is created. The population is sorted based on the non-domination. Each candidate solution is assigned a fitness value (or rank) equal to its non-domination level (1 is the best level, 2 is the next-best level and so on). Minimization of objectives is assumed. At first, the usual binary tournament selection, recombination, and mutation operators are used to create an offspring Q_0 of size N. Since elitism is introduced by comparing current best with previously found best non-dominated solutions.

NSGA-II is simple and straightforward algorithm. First a combined population $R_t = P_t \cup Q_t$ is formed. The population size R_t is 2N. Then, the population R_t is sorted according to non-domination property. Since all previous and current population members are included in R_t, elitism is insured. Now, candidate solutions belonging to the best non-dominated set F_1 are the best solutions in the combined population. If the size is smaller than N, I definitely choose all the members of the set F1 for the new population P_{t+1}.The remaining member of the population P_{t+1} are chosen from the subsequent non-domination fronts in the order of their ranking. Thus, solutions from the set F_2 are chosen next, followed by the solution s from the set F_3, and so on. This procedure is continued until no more sets can be accommodated. Say that the set F_1, is the last non-dominated set beyond which no other set can be accommodated. In general, the count of the candidate solutions in all the sets from F_1. To choose exactly N population members, I sort the solutions of the last front F_1, using the crowded comparison operator $<_n$ in descending order and

choose the best solutions needed to fill all population slots [61-67]. The **crowded distance** is measured as the perimeter of the maximum box containing the two neighboring solutions in the objective space.

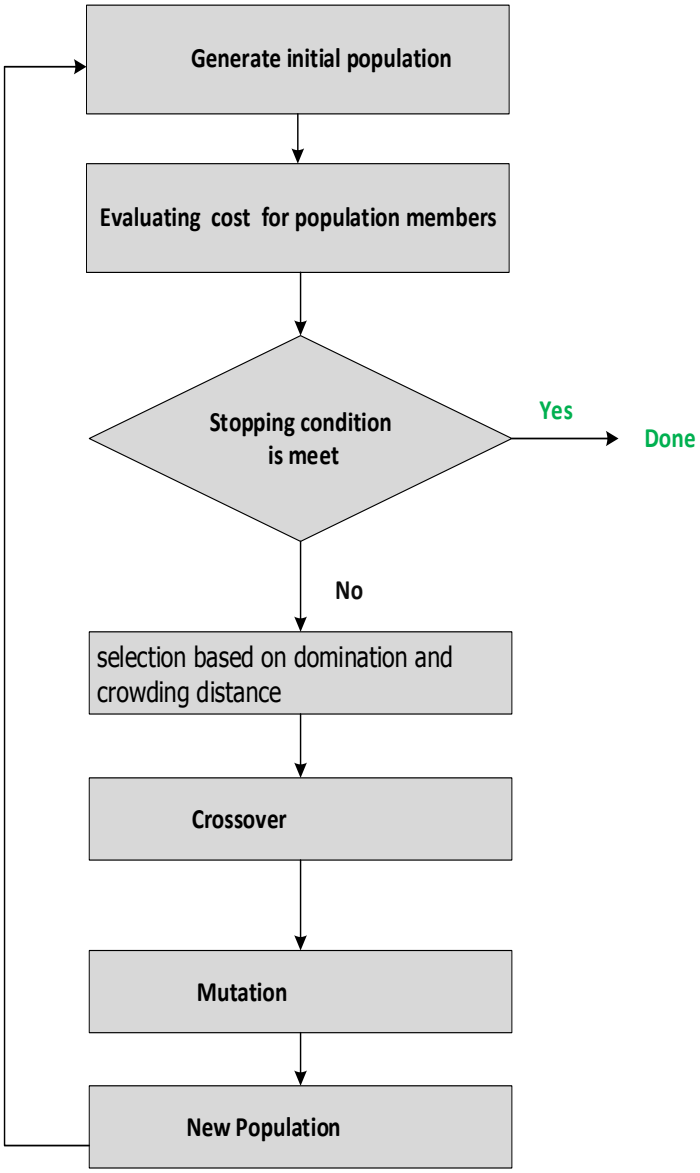

Figure 2.2: Flow chart representing different steps involved in NSGA-II optimization

The new population Pt+1 of size N is now used for selection, crossover, and mutation to create a new population Qt+1 of size N. it is important to note that I use a binary tournament selection operator, but the selection criterion is now based on the crowded comparison operator

$<_n$. Since this operator require both rank and crowded distance of each candidate solution in the population, I calculated these quantities while forming the population $P_{t+1.}$The basic operations and their worst-case complexities are as follows.

1) Non-dominated sorting is $O(MN)^2$);
2) Crowding distance assignment is O(MN log N);
3) Sorting on $<_n$ is O (N Log N).

The overall complexity of the algorithm is O (MN^2), which is governed by the non-dominated sorting component of the algorithm. If performed carefully, the whole population of size 2N need not be sorted according to non-domination. As soon as the sorting procedure has found enough number of front to have N members in $P_{t+1,}$ there is no reason to continue with the sorting procedure.

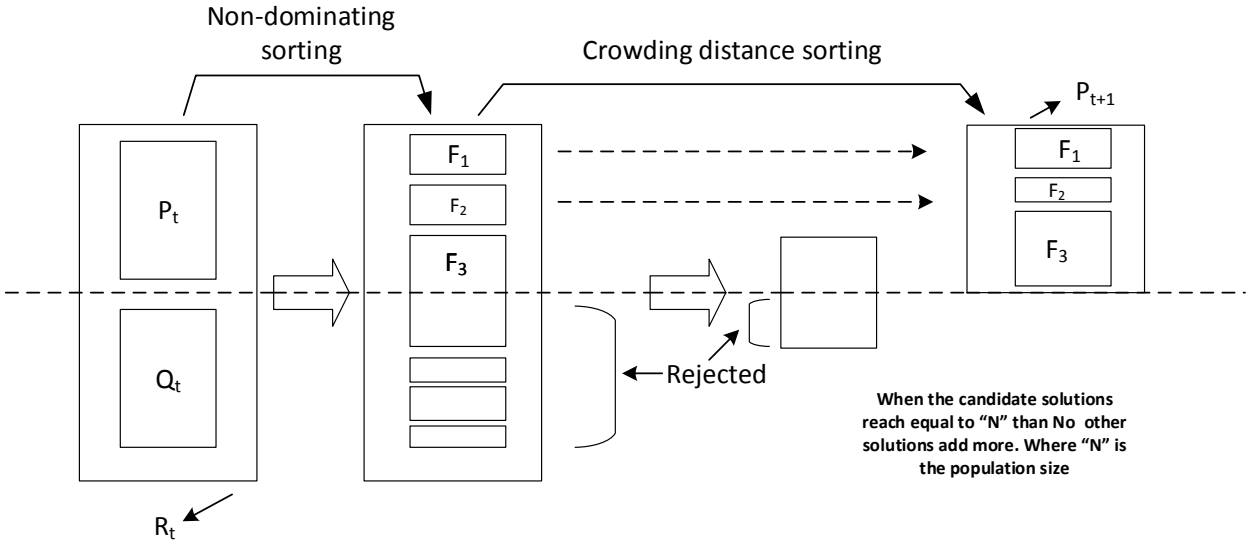

Figure 2.3: NSGA-II Algorithm

In order to identify the solution of the first non-dominated front in a population size N, each candidate solution can be compared with every other candidate solution in the population in term of domination. This requires O (MN) comparisons for each solution, where M is the number

of objectives. When this process is continued to find all members of the first non-dominated level in the population, the total complexity O(MN^2). At this stage all the individual in the first non-dominated front are found. Figure 2.3 shows the NSGA-II procedure and the main NSGA-II algorithm is given in Table 2.1 [61, 66-68].

Table 2.1: NSGA-II Algorithm

$R_t = P_t \cup Q_t$	combine parent and offspring population
$F = fast - non - dominated - sort(R_t)$ of R_t	$F = (F_1, F_2, \ldots\ldots)$ all non-dominated front
$P_{t+1} = \emptyset \; and \; i = 1$	
$until \; \lvert P_{t+1}\rvert + \lvert F_i\rvert \leq N$	until the parent population is filled
$crowding - distance - assignment \; (F_i)$	calculated crowding-distance is F_i
$P_{t+1} = P_{t+1} \cup F_i$	include ith non-dominated front in the parent
$i = i + 1$	check the next front for inclusion
$sort(F_i, \prec_n)$	sort in descending order using $\prec_n$
$P_{t+1} = P_{t+1} \cup F_i[1:(N - \lvert P_{t+1}\rvert)]$	choose the first $(N - \lvert P_{t+1}\rvert)$ element of F_i
$Q_{t+1} = make - new - pop(P_{t+1})$	use selection, crossover and mutation to create New population Q_{t+1}
$t = t + 1$	Increment the generation counter

Fast non-dominated sort (P)

For each $p \in P$

$S_P = \emptyset$

$n_P = 0$

$q \in P$

if $(p < q)$ then — if p dominate q

$S_P = S_P \cup \{q\}$ Add q to the set of solution dominated by p

else if $(q < p)$

$n_P = n_P + 1$ increment the domination counter p

If $n_P = 0$ then q belong to the next front

$p_{rank} = 1$

$F_1 = F_1 \cup \{p\}$

$i = 1$ initialize the front counter

While $F_i \neq \emptyset$

$Q = \emptyset$ Used to store the member of the next front

For each $p \in F_i$

For each $q \in S_p$

$n_P = n_P - 1$

If $n_q = 0$ then q belong to the next front

$q_{rank} = i + 1$

$Q = Q \cup \{q\}$

$i = i + 1$

$$F_i = Q$$

After the sorting based on **crowding distance** is assigned to each individual. For selection (mating) individuals are selected on the bases of fitness (rank) and crowding distance. Crowding distance are assigned in each front so comparing individuals among the different fronts is meaningless [61, 70,71].

<u>crowding-distance –assignment (I)</u>

$l = |I|$ number of solutions in I

$I[i]_{distance} = 0$ initialize distance

For each objective m

$I = sort(I, m)$ sort using each objective value

$I[1]_{distance} = I[l]_{distance} = \infty$ so that boundary points are always selected

For $i = 2\ to\ (l-1)$ for all other points

$I[i]_{distance} = I[i]_{distance} + (I[i+1], m) - I[i-1].m)/(f_m^{max} - f_m^{min})$

Source: [61, 69]

Selection is done by using crowded-comparison operator $\prec_n$. Crowded-comparison is based on

(1) Non-Domination Fitness (rank) of the individual in front Fi as $p_{rank=i}$

(2) $p \prec_n q$ if

- $p_{rank} < q_{rank}$
- or if p and q belong to same front but $F_i(d_p) > F_i(d_q)$ i.e. the crowding distance of p is more than q. I prefer the one which have small crowding distance.

Chapter 3: System Description

Energy is directly related with welfare of human race. Currently it is generated through numerous different sources each with its own advantages and disadvantages. The recent disaster in Foukoshima, Japan have raised serious questions about the safety of nuclear energy. Changing climate around the globe and speedy erosion of fossil fuel resources have not only raised ecological concerns but have also raised questions about energy security. Keeping this in mind, different countries around the globe are heavily investing in green energy technologies which include but not limited to harnessing the solar energy and converting it into electricity heat and other useful commodities, using the energy in fast flowing wind (specially on coastal areas) and converting it into electricity using wind turbine, bio-mass heat, and electricity generation etc. All of these technologies are playing their role in addressing ecological, safety, and energy security concerns.

Among all the available renewable sources of energy, solar energy is being considered extensively as an alternative to fossil fuels. Solar energy can directly be converted to electricity using photovoltaic cells. It can also be used for heating purposes. Recently solar chillers are introduced for commercial applications. As the PV cells produce direct DC voltage and current, so they can also be directly coupled with electrolyzer for hydrogen production.

In this chapter, a novel an energy system with multi commodities will be introduced and discussed.

3.1 System Details

Figure 3.1 shows the system discussed in the present study. It is a multi-commodity system. The system is composed of four sub-systems, namely:

a) Primary power and heat transfer loop
b) Secondary power and heat production loop
c) Cooling loop
d) Hydrogen production

There are numerous advantageous of the proposed energy system compared to standalone electricity producing PV systems. Firstly it provides multi commodities using a single input by extracting the rejected heat using heat exchangers, hence the proposed system have higher energy and exergy efficiency. Secondly, because of the production of multi commodities using a single

energy input, the cost of net electrical workout is significantly lower than standalone power production using photovoltaic array. Thirdly, because of maximum energy usage, the system has minimum energy lost to the environment hence the proposed system is comparatively environmentally benign. The proposed system can be used for a residential compound which need heating, cooling and electricity. It can also be used to power an industrial facility where hydrogen can be used in fuel cells to generate electricity for night operation in addition to heating, cooling and electricity.

3.1.1 Primary Loop

In primary power and heat transfer loop, therminol – 66 is used as a fluid. The choice of therminol – 66 is because of its lower heat capacity and high boiling temperature. Therminol-66 is pumped from state-1 to state-2 using a pump which uses electrical work as an input and it increases the pressure of the fluid at stage-2. As the pressure drop in the system is not very high and to avoid exergy losses across the pump entrance, the therminol-66 is not pressurized to a very high pressure. Pumps are used to provide the necessary force required by the fluid to flow in the loop by overcoming the pressure drop in the loop. If the pressure drop is small in the system, then it is not recommended to pump the fluid at very pressure specially in order to avoid exergy losses in the system. At state-2 it enters into a heat exchanger-4 and ensure that the stream coming out of the inter loop heat exchanger-1 is removed and the fluid entering the pump at stage-1 is at ambient conditions. The main reason for using heat exchanger-4 is that pumps are usually designed to work at low and medium temperatures (for water and related fluids applications typically less than 100^{o}C). There are pumps which can work at high temperatures but they are highly expensive. The pressurized fluid then enter the series of PV/T modules. PV/T modules receives concentrated solar irradiance from reflecting mirrors or dish (depending on how the PV/T is mounted).

A PV/T system produces electrical power and concentrated heat energy travels through different layers of the modules and heat the fluid passing through the PVT module. Figure 2.1 shows different layers of PV/T module. Each layer has its own thermal resistance and depending on its thermal conductivity, it transfers heat to the next layer. Therminol-66 exits PV/T modules at state-3. The temperature at the exit depends on the time of the day.

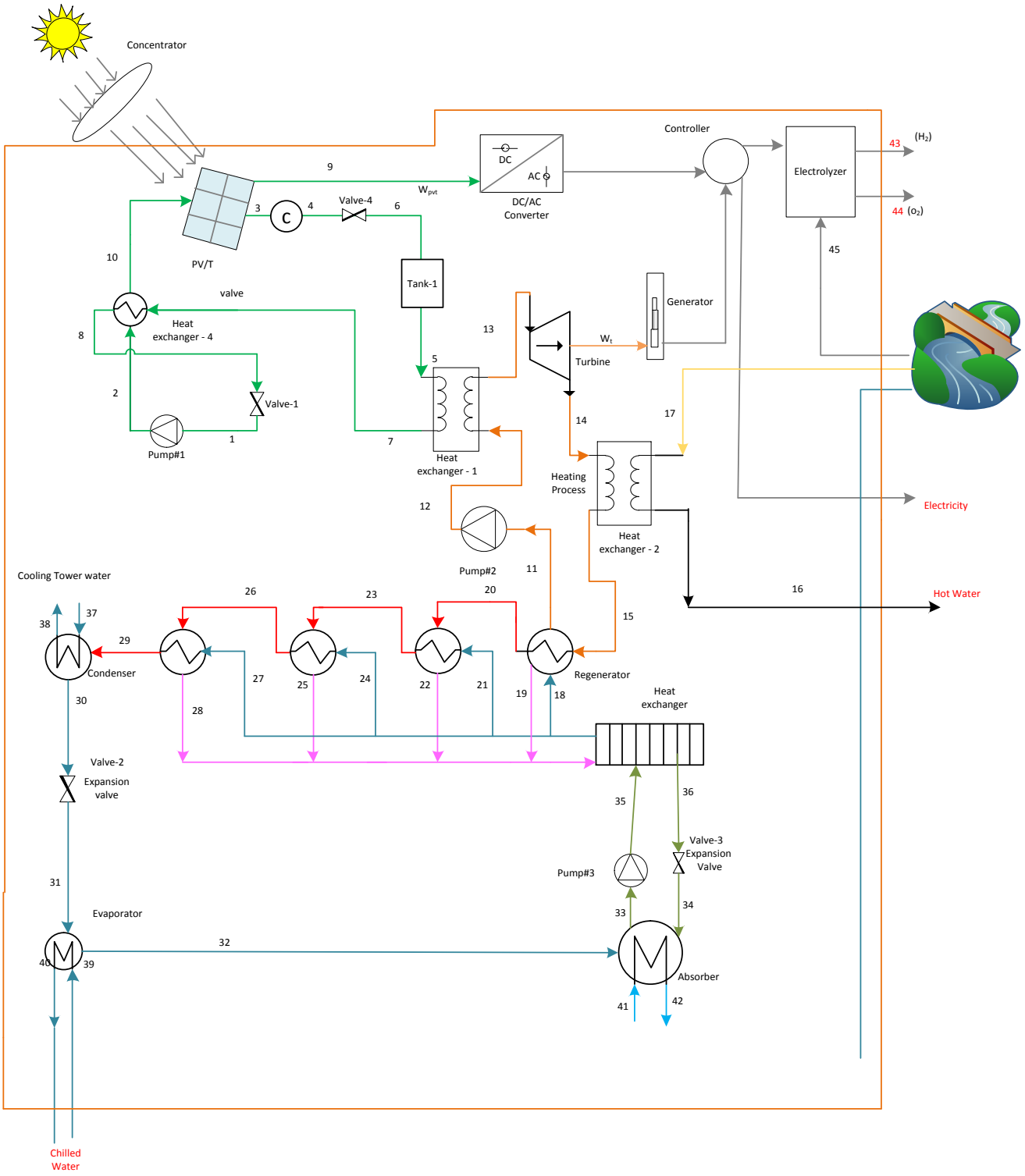

Figure 3.1: Multi Commodities Energy System

The variation in radiation intensity results variation in temperature at stage-3. After PV/T arrays therminol-66 will enter in the pressure regulating valve (V-4) and storage tank. The storage tank acts as a thermal battery. During the sunny period when the temperature at stage-3 is higher than the required designed temperature at stage-5, a part of the energy will be stored in the tank-1 (charging period). On the other hand, when the temperature at stage-3 is lower than the required designed temperature at stage-5, energy stored in the tank during the charring period is used to heat the fluid to its set point temperature. This cycle is called discharging. After that, the high temperature and pressure therminol-66 enters the inter loop HX-1 where it transfers heat to n-octane (working fluid of the secondary loop). The therminol-66 leaves the HX-1 at stage-7 and enters in HX-4 where it dissipates rest of its energy and pre-heat the pumped fluid. The cooled therminol-66 enters the valve (V-1) at stage 8 where its pressure will be reduced before entering into the pump.

3.1.2 Secondary Loop

When heat is being transferred to secondary loop in the heat exchanger (HX-1), it heats the secondary loop fluid. In present study, n-Octane is used as the working fluid for the secondary loop. Secondary loop is an organic Rankine cycle (ORC). The working principle of the organic Rankine cycles is same as steam Rankine cycles however they usually operate using low grade heat as an input. The boiling point of the organic fluids are relatively much lower than steam Rankine cycle at a given pressure so even low grade heat is enough to vaporize the working fluid in the ORC. n-Octane is being pumped from state-11 to state-12 using a pump (Pump # 2). In secondary loop, pressure is important, as the boiling point of the fluid increases with increase in pressure. However, increase in pressure also means increase in net electrical work input to the pump and system. It then passes through a inter loop heat exchanger of the circuit where it gets heated and vaporized due to the heat transfer between primary and secondary fluid. High pressure and temperature n-octane then enters the organic Rankine cycle turbine at state-13 and expands. As a result it rotates the shaft of the turbine and produces mechanical work as an output. The mechanical shaft work of the turbine is converted into electrical work or electricity by the generator. n-octane leaves the turbine at state-14. The pressure at stage-14 is significantly lower than stage-13. The temperature of the n-octane at stage-14 is still high enough and it exchanges heat with water (state-17) in heat exchanger (HX-2) and provide hot water (state-17) for domestic

consumption. At state-15 n-octane enters in a quadruple very high temperature generator (D-1) and gives all of its heat and reach the ambient temperature at low pressure.

3.1.3 Cooling Loop

Heat absorbed by the very high temperature generator is used to heat the ammonia water mixture coming out of heat exchanger at state-18. It increases the temperature of the mixture and vaporize the ammonia while hot water exits the D-1. The high temperature ammonia enters at state-20, the high temperature generator, where a stream of ammonia water mixture also enters at state-21. The temperature of the ammonia is high enough that it vaporizes all the ammonia in the pre-heated mixture of ammonia water entering at state-20. Pure ammonia then leaves the high temperature generator at 23 and enters into medium temperature generator while water leaves the high temperature generator at state-22. Medium temperature generator (D-3) also performs the same function and ammonia leaves the generator at D-3 at state-26 and enters in low temperature generator while water leaves the D-3 at state-25. Finally pure heated ammonia enters into a condenser at state-29 where it is being condensed at state-30 using cooling water (mostly coming from cooling tower) entering condenser at state-37 and leaving at state-38. The condensed ammonia is then throttled and expanded using an expansion valve V-2 at state-32. This significantly reduces the pressure and temperature of the ammonia. It then passes through an evaporator and provides exchange heat with hot water or air and leave the evaporator at state-32 where it enters absorber.

On the other hand, water coming out of generators gained heat and it exchanges heat (HX-3) to pre-heat the feeding stream at state-35. Water leaves the HX-3 after transferring its heat to the ammonia water solution and expanded to the same pressure as state-32 using an expansion valve at state-34. Pure ammonia coming at state-32 and water at state-34 are mixed in absorber and form an ammonia water mixture. The ammonia water mixing is an exothermic reaction and it requires cooling. Water enter at state-41 to cools the mixture before it is pumped from state-33 to state-35.

3.1.4 Hydrogen production

A part of the electricity is used to generate hydrogen, namely, PEM electrolyser. PEM electrolyser consists of anode and cathode, separated by a polymer membrane. Water enters the PEM electrolyser at state-45 and produces hydrogen (state-43) and oxygen (state-44) which can be

stored and used later on. PEM electrolyser is connected with electricity controller which provide electricity to the electrolyser. Electrical controller only provides excess electricity to the PEM electrolyser. In present study, it is assumed that 10% of the produced total power will be used for electrolysis.

Chapter 4: System Modeling

In this chapter, a novel energy system with multi commodities will be modeled. As stated earlier, the main input of the system is solar radiation. The system produces electric power, hydrogen, hot and cold water using a quadruple ammonia water.

This chapter also includes modeling of above mentioned system. The following sub-models are developed for the system:

- Radiation Model: As this is a solar based system, therefore it is necessary to predict solar irradiance at any given time. In present study, the Iqbal model has been used to accurately predict solar irradiance anywhere in the world at any given time. For sake of analysis, the system is developed for Toronto, ON, Canada.
- I-V Model: This model is used to find I-V characteristic of the utilized solar panel used. The input of the models are solar irradiance and other manufacturing characters and this model can predict how much output power is produced from the PV panel.
- PVT Thermal Model : As the light is been concentrated on the PV module which eventually is used to heat the working fluid, a PVT model is developed which predicts the outlet temperature of the fluid coming out from series of PV modules.
- Thermodynamic Model: Based on 1^{st} and 2^{nd} law thermodynamic principles, this model presents the mass balance, energy balance, entropy balance, and exergy balance across different system components. This model also helps us to find the effect of different processing conditions on system performance.
- Exergoeconomic Model: Based on 2^{nd} law analysis, exergoeconomic model presents cost of different streams by taking in account capital cost, interest rate, inflation rate, and other different parameters.
- Efficiency Analysis: based on thermodynamic modeling and system boundary, energy and exergy efficiencies of the system is defined.
- Exergoenvironmental Analysis: Based on 2^{nd} law analysis different exergoenvironmental parameters are defined. These parameters actually represent the effect of system performance on environment.
- Enviro Economics Analysis: This model represents cost of environmental impact of the PVT system when compared to an equivalent coal based system.

- Optimization: The formulation for optimization and sensitivity analysis on the nominal optimized solution is presented.

4.1 System Modeling

As discussed above, a number of various analysis have been carried out on the system. This section provides details and mathematical models mentioned above.

4.1.1 Radiation Model

Iqbal's model [73], which is also one of the most detailed and accurate model, is adopted to predict the radiation intensity for any location around the globe at any given time. The total radiation hitting on the surface is the sum of the reflected, diffuse and normal component (Figure 4.1). It can be written as

$$\dot{I}_t = \dot{I}_b + \dot{I}_d + \dot{I}_r \tag{4.1}$$

If the surface is tilted at an angle $\emptyset$, then the total solar radiation falling on a titled surface can be expressed as

$$\dot{I}_t = r_r \dot{I}_b + \frac{1+\cos\emptyset}{2}\dot{I}_d + \frac{1-\cos\emptyset}{2}(\dot{I}_b + \dot{I}_d)\chi \tag{4.2}$$

or it can be rewritten as

$$\dot{I}_t = r_r \dot{I}_b + \frac{1+\cos\emptyset}{2}\dot{I}_d + \frac{1-\cos\emptyset}{2}\dot{I}_t\chi \tag{4.3}$$

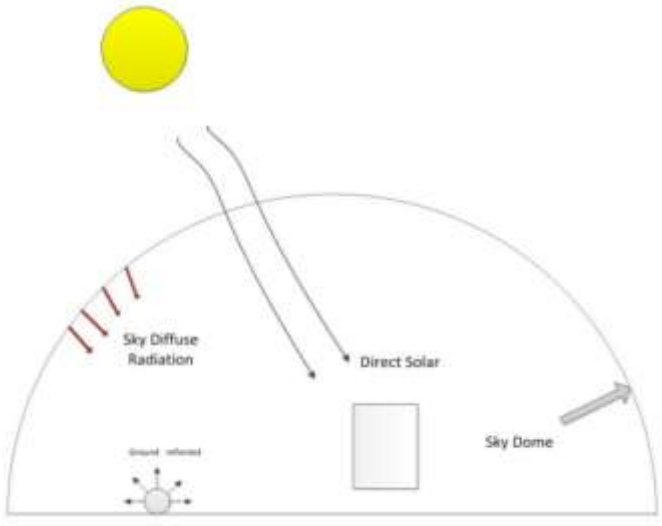

Figure 4.1: Total solar radiations on an object.

Where χ shows the reflectivity of the ground surface,$\dot{I}_r$,$\dot{I}_d$, $\dot{I}_b$ shows the reflected, diffuse and reflected components of the solar radiation on a surface. Table 4.1 shows the reflectance values of different surfaces. The factor r_r in Eq. 4.3 is a function of geographical parameters and can be determined as

$$r_r = \frac{\cos(\psi-\emptyset)\cos\delta\cos\omega+\sin(\psi-\emptyset)\sin\delta}{\cos(\psi)\cos\delta\cos\omega+\sin(\psi)\sin\delta} \quad (4.4)$$

where ω shows the solar angle and measured in radians $\emptyset$ shows the tilt angle, ψ shows the latitude in degrees and δ represents the declination angle.

Table 4.1: Reflectance values for different surfaces [75-84].

Material/Category	**Reflectance "χ"**
Concrete	0.23
Cement board	0.25
Brick (clay brick)	0.3
Limestone	0.28
Steel	0.18
Shingles, asphalt	0.14
Granite	0.33
Sandstone	0.35
Wood, unpainted	0.4
Wood, painted	0.38
Iron	0.13
Site exposure	**Reflectance of snow-covered ground**
Typical city center	0.2
Typical urban site	0.4
Typical rural site	0.5
Isolated rural site	0.7
Soil and Vegetation	
Soil (Dark & Wet)	0.05~0.4
Soil (Light & dry)	0.15~0.45
Grass (Long to short)	0.16~0.26
Agricultural crops	0.18~0.25
Tundra	0.18~0.25
Forest (Delicious)	0.15~0.20
Forest (Coniferous)	0.05~0.15
Snow (old to fresh)	0.40~0.95

The normal direct radiation hitting an object can be calculated as

$$\dot{I}_n = 0.9751 E_o \dot{I_{sc}} \tau_r \tau_o \tau_g \tau_w \tau_a \quad (4.5)$$

where $E_o$represents the eccentricity correction factor (E_o) for the earth orbit and can be calculated as

$$E_o = 1.00011 + 0.034221\cos\Gamma + 0.00128\sin\Gamma + 0.000719\cos 2\Gamma + 0.000077\sin 2\Gamma \quad (4.6)$$

where Γ is the day angle, it can be estimated in radians as

$$\Gamma = 2\pi\left(\frac{N-1}{365}\right) \quad (4.7)$$

where N represents the day number in the year (For example, 1st January N=1 and for December 31, N=365). The dimensionless Rayleigh constant in Eq. 4.5 can be found as

$$\tau_r = e^{-0.0903 m_a^{0.84}\left(1+m_a-m_a^{1.01}\right)} \quad (4.8)$$

Where m_r represents the mass at standard pressure (i.e. 101 kPa), m_a shows the air mass at actual pressure m_a. The m_a and m_r can be correlated as

$$m_a = m_r\left(\frac{p}{1014.15}\right) \quad (4.9)$$

where p shows the local pressure of air in mill bars. The air mass at standard pressure can be computed as

$$m_r = [\cos\theta_z + 0.15(94.885 - \theta_z)^{-1.253}]^{-1} \quad (4.10)$$

The dimensionless ozone constant can be calculated as

$$\tau_o = 1 - [0.1611 U_3(1 + 139.48 U_3)^{-0.3035} - 0.002715 U_3(1 + 0.044 U_3 + 0.0003 U_3^2)^{-1}] \quad (4.11)$$

where U_3 is the ozone relative optical length, it can be calculated as

$$U_3 = l_{0z} m_r \quad (4.12)$$

Here, l_{0z} shows the vertical ozone layer thickness and measured in centimeters. For present analysis, it is taken as 0.35cm [73]. The dimensionless gas constant can be evaluated as

$$\tau_g = e^{-0.0127 m_a^{0.26}} \quad (4.13)$$

The dimensionless water constant can be calculated as

$$\tau_w = 1 - 2.4959 U_1[(1 + 79.034 U_1)^{0.6828} + 6.385 U_1]^{-1} \quad (4.14)$$

where U_1 is the pressure corrected relative optical path length in centimeters.

$$U_1 = wm_r \tag{4.15}$$

where in Eq. 4.15, w shows the water vapour thickness at standard ambient conditions (i.e. P = 101325 Pa and T = 298.15 K) in centimeters, the actual thicknesses w' can be evaluated at other temperatures and pressures as

$$w = w' \left(\frac{p}{1014.15}\right)^{\frac{3}{4}} \left(\frac{273}{T}\right)^{\frac{1}{2}} \tag{4.16}$$

$$w' = 0.1e^{2.2572+0.05454T_{dew}} \tag{4.17}$$

where T_{dew} shows the dew point temperature

The dimensionless aerosols constant can be computed as

$$\tau_a = e^{-l_{ao}^{0.873}(1+l_{0a}-l_{ao}^{0.7808})m_a^{0.9108}} \tag{4.18}$$

l_{0a} is the aerosol optical thickness and can be calculated as

$$l_{ao} = 0.2758l_{ao;\lambda|\lambda=0.38\mu m} + 0.35l_{ao;\lambda|\lambda=0.5\mu m} \tag{4.19}$$

Another correlation to calculate dimensionless aerosol constants (as a function of visibility), can be written as

$$\tau_a = (0.97 - 1.265V_{is}^{-0.66})^{m_a^{0.9}} \tag{4.20}$$

where V_{is} is the visibility in kilometers, which can be calculated as

$$V_{is} = 147.994 - 1740.523[\beta_1\varphi - (\beta_1^2\varphi^2 - 0.17\beta_1\varphi + 0.011758)^{0.5}] \tag{4.21}$$

Here, φ can be calculated as

$$\varphi = 0.55^{-\beta_2} \tag{4.22}$$

where β_1 and β_2 are the Angstrom turbidity-parameters. The typical value for $\beta_2$is 1.3 [74]. The value for β_1 is dependent upon weather conditions and are given in Table 4.2

Table 4.2: Typical values of β_1 [74].

Weather Condition	β_1
Clean	0
Clear	0.1
Turbid	0.2
Very turbid	0.4

The beam component in Eq. 4.3 of the total radiations can be evaluated as

$$\dot{I}_b = \cos\theta_z \dot{I}_n \quad (4.23)$$

Table 4.3: Typical values of ρ_g [74-76]

Material	ρ_g
Concrete	0.09
Uncolored concrete	0.35
White glazed surface	0.74
Grass	0.17.0.28
Wheat	0.16.0.26
Maize	0.18-0.22
Beets	0.18
Potato	0.19
Rain forest	0.12
Deciduous forest	0.10-0.20
Coniferous forest	0.05.0.15
Sub-artic	0.09-0.20
Savannah	0.16.0.21
Steppe	0.20
Fresh snow	0.75.0.95
Old snow	0.40-0.70
Wet dark soil	0.08
Dry dark soil	0.13
Dry sand	0.35
Boreal forest with snow	0.12.0.30
Dune sand	0.24
Sandy loam	0.10-0.19
Clay loam	0.10-0.14

where θ_z represents the zenith angle and it can be calculated as

$$\cos\theta_z = \cos\delta\cos\psi\cos\omega + \sin\delta\sin\psi \quad (4.24)$$

where ω shows the solar hour angle, ψ shows the geographical latitude, δ is the solar declination angle and can be estimated as

$$\delta = 24.45 \sin\left(\frac{360(N+284)}{365}\right) \quad (4.25)$$

The solar hour angle ω is an angular measure of time. It is dependent upon local solar time (ST) and can be calculated as

$$\omega = 15(12 - ST) \tag{4.26}$$

The local solar time is a function of local standard time and is ultimately an equation of time. It can be determined as

$$ST = LT + \frac{ET}{60} - \frac{4}{60}(L_s - L_L) \tag{4.27}$$

where LT represents the local standard time, L_S is the standard meridian for the local time zone; L_L is the longitude of the location in degrees, whereas ET is the equation of time and can be calculated as

$$ET = 9.87\sin 2B - 7.53\cos B - 1.5\sin B \tag{4.28}$$

Here, B can be calculated as

$$B = \frac{360(N-81)}{365} \tag{4.29}$$

The diffuse component can be calculated as

$$\dot{I}_d = \dot{D}_r + \dot{D}_a + \dot{D}_m \tag{4.30}$$

where $\dot{D}_r$ shows the Rayleigh scattering after the first pass through the atmosphere, $\dot{D}_a$ represents the aerosols scattering after the first pass through the atmosphere. $\dot{D}_m$ shows the reflection processes between the ground and sky. All of which are measured in W/m^2. The aerosols scattering after the first pass through the atmosphere of the total diffuse radiations can be computed as

$$\dot{D}_a = \frac{0.79\dot{I}_{sc}\sin\alpha\tau_0\tau_g\tau_w\tau_{aa}F_c(1-\tau_{as})}{1-m_a+m_a^{1.02}} \tag{4.31}$$

τ_{as} is dimensionless factor and can be related to τ_a and τ_{aa} as

$$\tau_{as} = \frac{\tau_a}{\tau_{aa}} \tag{4.32}$$

F_c represents the ratio of forward scattering to total scattering. For present study, its value is taken as 0.84. The reflection processes between the ground and sky ($\dot{D}_m$) can be estimated as

$$\dot{D}_m = \frac{(\dot{I}_n\sin\alpha+\dot{D}_r+\dot{D}_a)\rho_g\rho_a}{1-\rho_g\rho_a} \tag{4.33}$$

where ρ_g is the dimensionless parameter and it represents the albedo of the ground. It is dependent upon weather conditions typical values are given in Table 4.4, ρ_a shows the albedo of the cloudless sky

$$\rho_a = 0.0685 + (1 - F_c)(1 - \tau_{as}) \quad (4.34)$$

The Rayleigh scattering factor of the diffuse radiation is evaluated as

$$\dot{D}_r = \frac{0.79\dot{I}_{sc}\sin\alpha\tau_0\tau_g\tau_w\tau_{aa}0.5(1-\tau_r)}{1-m_a+m_a^{1.02}} \quad (4.35)$$

where $\dot{I}_{sc}$ represents the solar constant and its value is 1367 W/m^2, α represents the solar angle and can be related with zenith angle as

$$\cos\theta_z = \sin\alpha \quad (4.36)$$

Here, τ_{aa} is the dimensionless constant and can be determined as

$$\tau_{aa} = 1 - (1 - \omega_0)(1 - m_a + m_a^{1.06})(1 - \tau_0) \quad (4.37)$$

where ω_0 is the single-scattering albedo fraction of the incident energy scattered to total attenuation by aerosols. Typical value of ω_0 is 0.9.

This completes the radiation modeling.

4.1.2 I-V Model

Then the current voltage (I_{pv}, V_{pv}) characteristic of the PV module under the reference conditions [T = 25^{0}C, P = 101325 Pa] can be given as follows [36-50]

$$I_{pv} = I_{sc.ref}\left[1 - C_1\left(\exp\left(\frac{V_{pv}}{C_2 V_{oc,ref}}\right) - 1\right)\right] \quad (4.38)$$

where V_{Pv} represents photovoltaic module output voltage, V, $V_{oc,ref}$ represent open circuit voltage under normal conditions of solar irradiance and temperature, respectively, $I_{sc.ref}$ represents short circuit current under normal conditions of solar irradiance and temperature; C_1 , C_2 are constants and can be evaluated as

$$C_1 = \left(1 - \frac{I_{max,ref}}{I_{sc,ref}}\right)\exp\left(\frac{V_{max,ref}}{C_2 V_{oc,ref}}\right) \quad (4.39)$$

$$C_2 = \left(\frac{\left(\frac{V_{max,ref}}{V_{oc,ref}}\right)-1}{\ln\left(1-\left(\frac{I_{max,ref}}{I_{sc,ref}}\right)\right)}\right) \quad (4.40)$$

where $V_{max,ref}$ represents voltage at maximum power point under normal conditions of solar irradiance and temperature. The $V_{oc,ref}$ and $I_{sc,ref}$ of a string with number of cells in series (N_s) and parallel (N_m) can be calculated as;

$$V_{oc,ref} = V_{oc,ref,1} N_s N_{cells} \quad (4.41)$$

$$I_{sc,ref} = I_{sc,ref,1} N_m \quad (4.42)$$

where $V_{oc,ref,1}$ represents the open circuit voltage for one cell and $I_{sc,ref,1}$ represents the short circuit for one cell. Under the variable conditions of temperature and solar irradiance, the new value of the current (I_{pvn}) and the voltage (V_{pvn}) of the PV module/ generator are obtained by;

$$I_{pvn} = I_{pv} + \Delta I \quad (4.43)$$

$$V_{pvn} = V_{pv} + \Delta V \quad (4.44)$$

where I_{pv} represents photovoltaic module output current (A); ΔI and ΔV represent respectively the variation of the PV module current and voltage with solar radiation and temperature and they are given by the following equations [41-47]

$$\Delta I = \mu_{Isc}\left(\frac{G_\beta}{G_{ref}}\right)\Delta T + \left(\frac{G_\beta}{G_{ref}} - 1\right) I_{sc,ref} \quad (4.45)$$

$$\Delta V = -0.0539 V_{max,ref} \ln\left(\frac{G_\beta}{G_{ref}}\right) - \mu_{voc}(T_{cell} - T_{c,ref}) \quad (4.46)$$

where G_β represents total solar radiation on a tilted surface (W/m^2), G_{ref} is the reference solar radiation,i.e., 1000 $\frac{W}{m^2}$; $V_{max,ref}$ is the voltage at maximum power point under normal conditions of solar irradiance and temperature, T_{cell} represents the cell temperature and $T_{c,ref}$ reference cell temperature taken as 25 ^{0}C (298.15K); μ_{voc} represents coefficient of variation of the open circuit voltage as a function of temperature; μ_{Isc} represents coefficient of variation of the open circuit voltage as a function of temperature

$$\Delta T = T_c - T_{c,ref} \quad (4.47)$$

The total radiation on titled surface is the product of radiation intensity and concentration factor $G_\beta = \dot{I}_t Co_f$. where $\dot{I}_t$ represents the total radiation falling on one reflective mirror and Co_f represents the concentration factor. The cell temperature will be defined and calculated using thermal model in the Section 4.1.4. The I_{pv} and V_{max} can be evaluated as follows

$$I_{pv} = I_{sc.ref}\left[1 - C_1\left(\exp\left(\frac{V_{pv}}{C_2 V_{oc,ref}}\right) - 1\right)\right] + \Delta I \quad (4.48)$$

$$V_{max} = V_{max,ref}\left\{1 + 0.0539\text{Log}\left(\frac{G_\beta}{G_{ref}}\right)\right\} + \mu_{voc}\Delta T \quad (4.49)$$

where μ_{voc} represents coefficient of variation of the open circuit voltage as a function of temperature. $V_{max,ref}$ for a chained cells can be calculated as

$$V_{max,ref} = V_{max,ref,1} N_s N_{cells} \quad (4.50)$$

Table 4.4: GaAs Module Parameters

	Cell Dimensions	mm	50 x 19
N_s	Number of cells in series in a string		5
N_m	Number of cells in Parallel in a string		2
η_{Pv}	Efficiency at STC	%	28.8
$V_{max,ref,1}$	Maximum voltage at STC	V	0.96
$I_{max,ref,1}$	Maximum current at STC	A	0.22
FF	Fill Factor		84.2
$V_{oc,ref,1}$	Open circuit at STC	V	1.09
$I_{sc,ref,1}$	Short circuit current	A	0.23
μ_{Isc}	Temperature coff. for current	A/K	0.00019
μ_{voc}	Temperature coff. for voltage	V/K	-0.00204
N_{Cell}	Number of cells in one module		36

Using Eq.s 4.48 and 4.49 in Eq.s 4.43 and 4.44 present us actual I-V of the PV module. A number of parameters are provided by the manufacturer. In present study, GaAs solar cell modules from Alta devices are considered. Alta devices have provided the parameters for their module given in (Table 4.4)

4.1.3 PVT Thermal Model

As shown in Figure 2.1, PV/T modules have different layers in it. Rate at which energy is being transferred from one layer to another layer depends on thermal conductivity of the layer determined by number of other parameters. The energy balance across glass to tedlar in a PV module can be written as

The rate of solar energy on PV module=An overall heat loss from the top surface of PV cell to ambient + An overall heat transfer from PV cell to the back surface of tedlar + The rate of electrical energy produced, formulated as

$$\tau_g[\alpha_c\beta_c G + \alpha_T(1-\beta_c)G]Wdx = [U_t(T_{cell} - T_{amb}) + U_T(T_{cell} - T_{bs})]Wdx + \tau_g\beta_c\eta_{el}G_\beta Wdx \quad (4.51)$$

where τ_g represents the transmitivity of glass and its value is taken as 0.95 in present study, α_c represents the absorptivity of solar cell and its value is taken as 0.85, β_c represents packing factor and its value is taken as 0.83, G_β represents solar radiation intensity (W/m^2), α_T represents absorptivity of Tedlar and its value is taken as 0.5, W represents the width of PV/T air collector, dx represents the elemental length of flow duct. T_{cell} represents the cell temperature and measured in kelvin, T_{amb} represents ambient temperature (kelvin), T_{bs} represents the back surface temperature (kelvin), η_{el} represents the electrical efficiency, U_T indicates the conductive heat transfer coefficient from solar cell through tedlar to flowing therminol-66 and can be calculated as;

$$U_T = \left[\frac{L_{si}}{K_{si}} + \frac{L_T}{K_T}\right]^{-1} \quad (4.52)$$

where L_{si} represents the thickness of solar cell (m), k_{si} represents the conductivity of silicon solar cell (W/m K), L_T represents the thickness of tedlar (m), K_T represents the conductivity of tedlar (W/m K). The overall heat transfer coefficient from cell to ambient through glass cover can be calculated as

$$U_t = \left[\frac{L_g}{K_g} + \frac{1}{h_{conv,t}} + \frac{1}{h_{rad}}\right]^{-1} \quad (4.53)$$

where L_g represents the thickness of glass cover (m), K_g indicates the conductivity of glass cover (W/m k). The connective heat transfer coefficient can be estimated as

$$h_{conv,t} = 2.8 + 3V_w \quad (4.54)$$

where $h_{conv,t}$ represents the heat transfer coefficient, V_w represents the wind speed (m/s). The radiative heat transfer coefficient between PV/T collector and surrounding can be found as;

$$h_{rad} = \varepsilon_g\sigma(T_{sky} + T_{cell})(T_{sky}^2 + T_{cell}^2) \quad (4.55)$$

where ε_g and σ are the PV/T air collector emissivity and the Stefan-Boltzmann's constant, respectively, where

$$T_{sky} = T_{amb} - 6 \tag{4.56}$$

The energy balance across the back surface of the toddler can be written as;

An overall heat transfer from the back surface to tedlar = the rate of heat transfer from the back surface of tedlar to flowing air, can be formulated as follow:

$$U_T(T_{cell} - T_{bs})Wdx = h_f(T_{bs} - T_f)Wdx \tag{4.57}$$

where T_f represents the flowing air temperature and measured in Kelvin, h_f represents convective heat transfer coefficient inside the duct, h_f is calculated according to flow regime and its Nusselt number. Energy balance across the therminol – 66 flowing though the duct is written as;

$$\dot{m}C_p\left(\frac{dT_f}{dx}\right)dx + U_b(T_f - T_{amb})Wdx = h_f(T_{bs} - T_f)Wdx \tag{4.58}$$

where $\dot{m}$ represents the mass flow rate and measured in kg/s, C_p represents the specific heat capacity of air (J/kg K), T_{sky} represents the effective temperature of the sky (K). Overall back loss coefficient from flowing therminol-66 to ambient is calculated as;

$$U_b = \left[\frac{L_i}{K_i} + \frac{1}{h_{conv,b}}\right]^{-1} \tag{4.59}$$

where L_i, K_i and $h_{conv,b}$ are the thickness of the back insulation (m), the conductivity of back insulation (W/m K)and conductive heat transfer co efficient on the back surface of PV/T air collector (W/m k), respectively

The equation for cell temperature is deduced from Eq.s 4.51 and 4.57 and it is written as

$$T_{cell} = \frac{(\sigma\tau)_{eff}G_\beta + \cup_t T_{amb} + \cup_T T_{bs}}{\cup_t + \cup_T} \tag{4.60}$$

where $\cup_t$ represents overall heat transfer coefficient from solar cell to ambient through glass cover (W/m^2k), $\cup_T$ represents the conductive heat transfer coefficient from solar cell to flowing air through tedlar (W/m^2k). Back surface temperature can be calculated as

$$T_{bs} = \frac{h_{p1}(\sigma\tau)_{eff}G_\beta + \cup_{tT} T_{amb} + h_f T_f}{\cup_{tT} + h_f} \tag{4.61}$$

where $(\sigma\tau)_{eff}$ represents the product of effective absorptivity and transmissivity and can be estimated as

$$(\sigma\tau)_{eff} = \tau_g[\alpha_c\beta_c + \alpha_T(1-\beta_c) - \beta_c\eta_{el} \quad (4.62)$$

Penalty factor due to the presence of interface of solar cell material is calculated as

$$h_{p1} = \frac{U_T}{U_T+U_t} \quad (4.63)$$

where h_{p1} Penalty factor due to the presence of interface of solar cell material, glass and EVA. The penalty factor due to the presence of interface between tedlar and working fluid can be estimated as

$$h_{p2} = \frac{h_f}{U_{tT}+h_f} \quad (4.64)$$

Where h_{p2} represents the penalty factor due to the presence of interface between tedlar and working fluid, $\cup_{tT}$ represents an overall heat transfer coefficient from glass to tedlar through solar cell (W/m^2 K) and can be evaluated as;

$$\cup_{tT} = \left[\frac{1}{U_t} + \frac{1}{\cup_T}\right]^{-1} = \frac{\cup_T U_t}{\cup_T+U_t} \quad (4.65)$$

Overall heat loss coefficient from the PV/T collector to the environment can be evaluated as;

$$\cup_{tf} = \left[\frac{1}{h_f} + \frac{1}{\cup_{tT}}\right]^{-1} = \frac{\cup_{tT} h_f}{\cup_{tT}+h_f} \quad (4.66)$$

where $\cup_{tf}$ an overall heat transfer coefficient from glass to air through solar cell and tedlar (W/m^{2}k). An ODE is obtained by inputting Eq. 4.61 into Eq. 4.58

$$\frac{dT_f}{dx} + \left(\frac{WU_L}{\dot{m}C_p}\right)(T_f - T_{amb}) = \frac{Wh_{p1}h_{p2}(\sigma\tau)_{eff}G_\beta}{\dot{m}C_p} \quad (4.67)$$

where U_L represents the overall heat loss coefficient from the PV/T air collector to the environment (W/m^{2}k).

$$U_L = U_b + U_{tf} \quad (4.68)$$

where U_b an overall back coefficient from flowing fluid to ambient (W/m^{2}k) evaluated in Eq. 4.59. Integrating 4.67 gives us the fluid temperature across the length of the PV/T module and can be written as

$$T_f(x) = \left(T_{amb} + \frac{h_{p1}h_{p2}(\sigma\tau)_{eff}G_\beta}{U_L}\right)\left(1 - \exp\left(\frac{-WU_Lx}{\dot{m}C_p}\right)\right) + T_{f,in}\exp\left(\frac{-WU_Lx}{\dot{m}C_p}\right) \quad (4.69)$$

where T_f the flowing air temperature (Kelvin) is, C_p represents specific heat capacity of air (J/kg K), U_L represents heat loss coefficient from flowing air to ambient (W/m^2 K), W represents the

width of PV/T air collector (m). When the fluid exit the PV/T module ($x = L$) , the temperature of the fluid can be obtained by

$$T_{f,out} = \left(T_{amb} + \frac{h_{p1}h_{p2}(\sigma\tau)_{eff}G_{\beta}}{U_L}\right)\left(1 - \exp\left(\frac{-WU_LL}{\dot{m}C_p}\right)\right) + T_{f,in}\exp\left(\frac{-WU_LL}{\dot{m}C_p}\right) \quad (4.70)$$

The average temperature of the fluid can be obtained by integrating Eq. 4.67 over the length

$$\overline{T}_f = \frac{1}{L}\int_{x=0}^{L} T_f(x)dx$$

$$= \left[T_{amb} + \frac{h_{p1}h_{p2}(\sigma\tau)_{eff}G_{\beta}}{U_L}\right]\left[1 - \frac{(1-\exp(-WU_LL/\dot{m}C_p))}{WU_LL/\dot{m}C_p}\right] + \frac{T_{f,in}(1-\exp(-WU_LL/\dot{m}C_p))}{WU_LL/\dot{m}C_p} \quad (4.71)$$

where $T_{f,out}$represents the outlet air temperature (Kelvin), L represents the length of air duct (m), $T_{f,in}$ is the inlet air temperature (Kelvin). The overall heat transfer to the following fluid (therminol-66) can be written as

$$\dot{Q}_u = \dot{m}C_p\left(T_{f.out} - T_{f,in}\right) = \frac{\dot{m}C_p}{U_L}\left[h_{p1}h_{p2}(\sigma\tau)_{eff}G_{\beta} - U_L\left(T_{f,in} - T_{amb}\right)\right][1 - \exp(-WU_LL/\dot{m}C_p)] \quad (4.72a)$$

where Q_u represents the heat transfer rate. This completes the thermal modeling of the PVT module

4.1.4 Thermodynamic Modeling

Thermodynamic modeling of the overall system is been performed. Mass, energy, entropy and exergy balance equations are written for each of the component in the system.

4.1.4.1 Thermodynamic Analysis

Thermodynamic analysis is usually used to study the performance of energy systems. It is based on 1st and 2nd law of thermodynamics. First law analysis, commonly known as energy analysis, is based on energy balance across the system boundary. It is the quantities measurement of different energy streams across the system. This law simple states that energy in is equal to energy out for steady state control volume. Mathematically it can be expressed as

$$\sum \dot{E}_{in} = \sum \dot{E}_{out} \quad (4.72b)$$

First law analysis does not take in account the losses taking places within the system boundary. 2nd law analysis is actually qualitative analysis of the energy with the system boundary. It takes in

account different losses taking place within system boundary. For a steady state control volume system it can be expressed as

$$\sum \dot{E}x_{in} = \sum \dot{E}x_{out} + \dot{E}xd_{system} \quad (4.72c)$$

The last term in Eq. (2.2), $\dot{E}xd_{system}$, is actually measure of irreversibilities in the system. During these analyses, the following assumptions are taken:

- Steady state operation for all components.
- All units are based on the Standard International unit system, e.g., kilopascal (kPa) for pressure, Kelvin (K) for temperature and kilo-joules per kilogram (kJ/kg) for enthalpy.
- The heat exchanger, pumps, compressor and turbine are adiabatic and, hence, no heat transfer occurs between them and the surroundings.
- All kinetic and potential exergetic terms are negligible.
- The chemical exergetic term is not changed in the turbine, pumps, compressor or the heat exchanger.
- The ambient temperature and pressure are held constant (T0 and P0) and any change in their value would obviously imply a change in system exergetic efficiency.
- Oxygen and hydrogen are treated as ideal gas.
- Isentropic operation is assumed for the compressor and the turbine with isentropic efficiency of 0.8.

Pump-1 (1-2):

The mass, energy, entropy and exergy balance equations for Pump-1 are given as follows:

$$\dot{m}_1 = \dot{m}_2 \quad (4.73a)$$

$$\dot{W}_{P-1} + \dot{m}_1 h_1 = \dot{m}_2 h_2 \quad (4.73b)$$

$$\dot{m}_1 s_1 + \dot{S}_{g,P-1} = \dot{m}_2 s_2 \quad (4.73c)$$

$$\dot{m}_1 ex_1 - \dot{E}xd_{P-1} + \dot{W}_{P-1} = \dot{m}_2 ex_2 \quad (4.73d)$$

PV/T Module (2-3):

The mass, energy, entropy and exergy balance equations for PV/T module are given as follows:

$$\dot{m}_2 = \dot{m}_3 \quad (4.74a)$$

$$\dot{m}_1 h_1 + \dot{Q}_{in,solar} = \dot{m}_6 h_6 + \dot{W}_{PVT} \quad (4.74b)$$

$$\dot{m}_1 s_1 + \frac{\dot{Q}_{in,solar}}{T_{sun}} + \dot{S}_{g,PVT} = \dot{m}_6 s_6 \quad (4.74c)$$

$$\dot{m}_1 ex_1 + \dot{Q}_{in,solar}\left(1 - \frac{T_0}{T_{sun}}\right) = \dot{m}_6 ex_6 + \dot{W}_{PVT} \quad (4.74d)$$

Valve # 4 (4-6):

The mass, energy, entropy and exergy balance equations for Valve-4 are given as follows:

$$\dot{m}_4 = \dot{m}_6 \quad (4.75a)$$

$$\dot{m}_4 h_4 = \dot{m}_6 h_6 \quad (4.75b)$$

$$\dot{m}_4 s_4 + \dot{S}_{g,V-4} = \dot{m}_6 s_6 \quad (4.75c)$$

$$\dot{m}_4 ex_4 - \dot{Exd}_{V-4} = \dot{m}_6 ex_6 \quad (4.75d)$$

Heat Exchanger-4 (2-10,7-8):

The mass, energy, entropy and exergy balance equations for Heat Exchanger-4 are given as follows:

$$\dot{m}_2 = \dot{m}_{10} \quad (4.76a)$$

$$\dot{m}_7 = \dot{m}_8 \quad (4.76b)$$

$$\dot{m}_2 h_2 + \dot{m}_7 h_7 = \dot{m}_{10} h_{10} + \dot{m}_8 h_8 \quad (4.76c)$$

$$\dot{m}_2 s_2 + \dot{m}_7 s_7 + \dot{S}_{g,HX-1} = \dot{m}_{10} s_{10} + \dot{m}_8 s_8 \quad (4.76d)$$

$$\dot{m}_2 ex_2 + \dot{m}_7 ex_7 - \dot{Exd}_{HX-4} = \dot{m}_{10} ex_{10} + \dot{m}_8 ex_8 \quad (4.76e)$$

Valve-1 (8-1):

The mass, energy, entropy and exergy balance equations for Valve-1 are given as follows:

$$\dot{m}_1 = \dot{m}_6 \quad (4.77a)$$

$$\dot{m}_1 h_1 = \dot{m}_6 h_6 \quad (4.77b)$$

$$\dot{m}_1 s_1 + \dot{S}_{g,V-1} = \dot{m}_6 s_6 \quad (4.77c)$$

$$\dot{m}_1 ex_1 - \dot{Exd}_{V-1} = m_6 ex_6 \quad (4.77d)$$

Tank (5-6):

The mass, energy, entropy and exergy balance equations for Tank are given as follows:

$$\dot{m}_6 = \dot{m}_5 \quad (4.78a)$$

$$\dot{m}_6 h_6 = \dot{m}_5 h_5 \quad (4.78b)$$

$$\dot{m}_6 s_6 + \dot{S}_{g,Tk} = \dot{m}_5 s_5 \quad (4.78c)$$

$$\dot{m}_6 ex_6 - \dot{Exd}_{Tk} = \dot{m}_5 ex_5 \quad (4.78d)$$

Turbine (13-14):

The mass, energy, entropy and exergy balance equations for Turbine are given as follows:

$$\dot{m}_{13} = \dot{m}_{14} \quad (4.79a)$$

$$\dot{m}_{13} h_{13} = \dot{m}_{14} h_{14} + \dot{W}_T \quad (4.79b)$$

$$\dot{m}_{13} s_{13} + \dot{S}_{g,T} = \dot{m}_{14} s_{14} \quad (4.79c)$$

$$\dot{m}_{13} ex_{13} - \dot{Exd}_T = \dot{m}_{14} ex_{14} + \dot{W}_T \quad (4.79d)$$

Pump-2 (11-12):

The mass, energy, entropy and exergy balance equations for Pump-2 are given as follows:

$$\dot{m}_{11} = \dot{m}_{12} \quad (4.80a)$$

$$\dot{W}_{P\#2} + \dot{m}_{11} h_{11} = \dot{m}_{12} h_{12} \quad (4.80b)$$

$$\dot{m}_{11} s_{11} + \dot{S}_{g,P-2} = \dot{m}_{12} s_{12} \quad (4.80c)$$

$$\dot{m}_{11} ex_{11} - \dot{Exd}_{P-2} + \dot{W}_{P-2} = \dot{m}_{12} ex_{12} \quad (4.80d)$$

Heat Exchanger-1 (5-6, 12-13):

The mass, energy, entropy and exergy balance equations for Heat Exchanger-1 are given as follows:

$$\dot{m}_5 = \dot{m}_6 \quad (4.81a)$$

$$\dot{m}_{12} = \dot{m}_{13} \quad (4.81b)$$

$$\dot{m}_5 h_5 + \dot{m}_{12} h_{12} = \dot{m}_6 h_6 + \dot{m}_{13} h_{13} \quad (4.81c)$$

$$\dot{m}_5 s_5 + \dot{m}_{12} s_{12} + \dot{S}_{g,HX-1} = \dot{m}_6 s_6 + \dot{m}_{13} s_{13} \quad (4.81d)$$

$$\dot{m}_5 ex_5 + \dot{m}_{12} ex_{12} - \dot{Exd}_{HX-1} = \dot{m}_6 ex_6 + \dot{m}_{13} ex_{13} \quad (4.81e)$$

Heat Exchanger-2 (16-17,14-15):

The mass, energy, entropy and exergy balance equations for Heat Exchanger-2 are given as follows:

$$\dot{m}_{17} = \dot{m}_{16} \quad (4.82a)$$

$$\dot{m}_{14} = \dot{m}_{15} \quad (4.82b)$$

$$\dot{m}_{17}h_{17} + \dot{m}_{14}h_{14} = \dot{m}_{16}h_{16} + \dot{m}_{15}h_{15} \quad (4.82c)$$

$$\dot{m}_{17}s_{17} + \dot{m}_{14}s_{14} + \dot{S}_{g,HX-2.} = \dot{m}_{16}s_{16} + \dot{m}_{15}s_{15} \quad (4.82d)$$

$$\dot{m}_{17}ex_{17} + \dot{m}_{14}ex_{14} - \dot{Exd}_{HX-2} = \dot{m}_{16}ex_{16} + \dot{m}_{15}ex_{15} \quad (4.82e)$$

Very high Temperature Generator-1 (11-15,18-19-20):

The mass, energy, entropy and exergy balance equations for Very high Temperature Generator D-1 are given as follows:

$$\dot{m}_{11} = \dot{m}_{15} \quad (4.83a)$$

$$\dot{m}_{18} = \dot{m}_{19} + \dot{m}_{20} \quad (4.83b)$$

$$\dot{m}_{18}h_{18} + \dot{m}_{15}h_{15} = \dot{m}_{19}h_{19} + \dot{m}_{20}h_{20} + \dot{m}_{11}h_{11} \quad (4.83c)$$

$$\dot{m}_{18}s_{18} + \dot{m}_{15}s_{15} + \dot{S}_{g,D-1} = \dot{m}_{19}s_{19} + \dot{m}_{20}s_{20} + \dot{m}_{11}s_{11} \quad (4.83d)$$

$$\dot{m}_{18}ex_{18} + \dot{m}_{15}ex_{15} - \dot{Exd}_{D-1} = \dot{m}_{19}ex_{19} + \dot{m}_{20}ex_{20} + \dot{m}_{11}ex_{11} \quad (4.83e)$$

High Temperature Generator-2 (20-21-22-23):

The mass, energy, entropy and exergy balance equations for high Temperature Generator D-2 are given as follows:

$$\dot{m}_{21} + \dot{m}_{20} = \dot{m}_{22} + \dot{m}_{23} \quad (4.84a)$$

$$\dot{m}_{21}h_{21} + \dot{m}_{20}h_{20} = \dot{m}_{22}h_{22} + \dot{m}_{23}h_{23} \quad (4.84b)$$

$$\dot{m}_{21}s_{21} + \dot{m}_{20}s_{20} + \dot{S}_{g,D-2} = \dot{m}_{22}s_{22} + \dot{m}_{23}s_{23} \quad (4.84c)$$

$$\dot{m}_{21}ex_{21} + \dot{m}_{20}ex_{20} - \dot{Exd}_{D-2} = \dot{m}_{22}ex_{22} + \dot{m}_{23}ex_{23} \quad (4.84d)$$

Medium Temperature Generator-3 (23-24-25-26):

The mass, energy, entropy and exergy balance equations for Medium Temperature Generator D-3 are given as follows:

$$\dot{m}_{24} + \dot{m}_{23} = \dot{m}_{25} + \dot{m}_{26} \quad (4.85a)$$

$$\dot{m}_{24}h_{24} + \dot{m}_{23}h_{23} = \dot{m}_{25}h_{25} + \dot{m}_{26}h_{26} \quad (4.85b)$$

$$\dot{m}_{24}s_{24} + \dot{m}_{23}s_{23} + \dot{S}_{g,D-3} = \dot{m}_{25}s_{25} + \dot{m}_{26}s_{26} \quad (4.85c)$$

$$\dot{m}_{24}ex_{24} + \dot{m}_{23}ex_{23} - \dot{Exd}_{D-3} = \dot{m}_{25}ex_{25} + \dot{m}_{26}ex_{26} \quad (4.85d)$$

Low temperature Generator-4 (26-27-28-29):

The mass, energy, entropy and exergy balance equations for Low Temperature Generator D-4 are given as follows:

$$\dot{m}_{27} + \dot{m}_{26} = \dot{m}_{28} + \dot{m}_{29} \quad (4.86a)$$

$$m_{27}h_{27} + \dot{m}_{26}h_{26} = \dot{m}_{28}h_{28} + \dot{m}_{29}h_{29} \quad (4.86b)$$

$$m_{27}s_{27} + \dot{m}_{26}s_{26} + \dot{S}_{g,D-4} = \dot{m}_{28}s_{28} + \dot{m}_{29}s_{29} \quad (4.86c)$$

$$m_{27}ex_{27} + \dot{m}_{26}ex_{26} - \dot{Exd}_{D-4} = \dot{m}_{28}ex_{28} + \dot{m}_{29}ex_{29} \quad (4.86d)$$

Condenser (29-30, 37-38):

The mass, energy, entropy and exergy balance equations for Condenser are given as follows:

$$\dot{m}_{29} = \dot{m}_{30} \quad (4.87a)$$

$$\dot{m}_{37} = \dot{m}_{38} \quad (4.87b)$$

$$\dot{m}_{29}h_{29} + \dot{m}_{37}h_{37} = \dot{m}_{30}h_{30} + \dot{m}_{38}h_{38} \quad (4.87c)$$

$$\dot{m}_{29}s_{29} + \dot{m}_{37}s_{37} + \dot{S}_{g,Cond} = \dot{m}_{30}s_{30} + \dot{m}_{38}s_{38} \quad (4.87d)$$

$$\dot{m}_{29}ex_{29} + \dot{m}_{37}ex_{37} - \dot{Exd}_{Cond} = \dot{m}_{30}ex_{30} + \dot{m}_{38}ex_{38} \quad (4.87e)$$

Valve-2 (30-31):

The mass, energy, entropy and exergy balance equations for Valve-2 are given as follows:

$$\dot{m}_{30} = \dot{m}_{31} \quad (4.88a)$$

$$\dot{m}_{30}h_{30} = \dot{m}_{31}h_{31} \quad (4.88b)$$

$$\dot{m}_{30}s_{30} + \dot{S}_{g,V-2} = \dot{m}_{31}s_{31} \quad (4.88c)$$

$$\dot{m}_{30}ex_{30} - \dot{Exd}_{V-2} = \dot{m}_{31}ex_{31} \quad (4.88d)$$

Valve-3 (34-36):

The mass, energy, entropy and exergy balance equations for Valve-3 are given as follows:

$$\dot{m}_{36} = \dot{m}_{34} \quad (4.89a)$$

$$\dot{m}_{36}h_{36} = \dot{m}_{34}h_{34} \quad (4.89b)$$

$$\dot{m}_{36}s_{36} + \dot{S}_{g,V-3} = \dot{m}_{34}s_{34} \quad (4.89c)$$

$$\dot{m}_{36}ex_{36} - \dot{Exd}_{V-3} = \dot{m}_{34}ex_{34} \quad (4.89d)$$

Pump-3 (33-35):

The mass, energy, entropy and exergy balance equations for Pump-3 are given as follows:

$$\dot{m}_{33} = \dot{m}_{35} \quad (4.90a)$$

$$\dot{W}_{P-3} + \dot{m}_{33} h_{33} = \dot{m}_{35} h_{35} \quad (4.90b)$$

$$\dot{m}_{33} s_{33} + \dot{S}_{g,P-3} = \dot{m}_{35} s_{35} \quad (4.90c)$$

$$\dot{m}_{33} ex_{33} - \dot{Exd}_{P-3} + \dot{W}_{P-3} = \dot{m}_{35} ex_{35} \quad (4.90d)$$

Evaporator (31-32, 39-40):

The mass, energy, entropy and exergy balance equations for Evaporator are given as follows:

$$\dot{m}_{31} = \dot{m}_{32} \quad (4.91a)$$

$$\dot{m}_{39} = \dot{m}_{40} \quad (4.91b)$$

$$\dot{m}_{31} h_{31} + \dot{m}_{39} h_{39} = \dot{m}_{32} h_{32} + \dot{m}_{40} h_{40} \quad (4.91c)$$

$$\dot{m}_{31} s_{31} + \dot{m}_{39} s_{39} + \dot{S}_{g,Evp} = \dot{m}_{32} s_{32} + \dot{m}_{40} s_{40} \quad (4.91d)$$

$$\dot{m}_{31} ex_{31} + \dot{m}_{39} ex_{39} - \dot{Exd}_{Evp} = \dot{m}_{32} ex_{32} + \dot{m}_{40} ex_{40} \quad (4.91e)$$

Absorber (32-33-34, 41-42):

The mass, energy, entropy and exergy balance equations for Absorber are given as follows:

$$\dot{m}_{32} + \dot{m}_{34} = \dot{m}_{33} \quad (4.92a)$$

$$\dot{m}_{41} = \dot{m}_{42} \quad (4.92b)$$

$$\dot{m}_{32} h_{32} + \dot{m}_{34} h_{34} + \dot{m}_{41} h_{41} = \dot{m}_{33} h_{33} + \dot{m}_{42} h_{42} \quad (4.92c)$$

$$\dot{m}_{32} s_{32} + \dot{m}_{34} s_{34} + \dot{m}_{41} s_{41} + \dot{S}_{g,Abs} = \dot{m}_{33} s_{33} + \dot{m}_{42} s_{42} \quad (4.92d)$$

$$\dot{m}_{32} ex_{32} + \dot{m}_{34} ex_{34} + \dot{m}_{41} ex_{41} - \dot{Exd}_{Abs} = \dot{m}_{33} ex_{33} + \dot{m}_{42} ex_{42} \quad (4.92e)$$

Expansion Valve -3 (34-36):

The mass, energy, entropy and exergy balance equations for Expansion Valve-3 are given as follows:

$$\dot{m}_{36} = \dot{m}_{34} \quad (4.93a)$$

$$\dot{m}_{36} h_{36} = \dot{m}_{34} h_{34} \quad (4.93b)$$

$$\dot{m}_{36} s_{36} + \dot{S}_{g,V-3} = \dot{m}_{34} s_{34} \quad (4.93c)$$

$$\dot{m}_{36} ex_{36} - \dot{Exd}_{V-3} = \dot{m}_{34} ex_{34} \quad (4.93d)$$

Electrolyzer (43-44-45):

The mass, energy, entropy and exergy balance equations for electrolyzer are given as follows:

$$\dot{m}_{45} = \dot{m}_{43} + \dot{m}_{44} \quad (4.94a)$$

$$\dot{m}_{45}h_{45} + \dot{W}_{Electrolyzer} = \dot{m}_{43}h_{43} + \dot{m}_{44}h_{44} \quad (4.94b)$$

$$\dot{m}_{45}s_{45} + \dot{S}_{g,Electrolyzer} = \dot{m}_{43}s_{43} + \dot{m}_{44}s_{44} \quad (4.94c)$$

$$\dot{m}_{45}ex_{45} + \dot{W}_{Electrolyzer} - \dot{Exd}_{Electrolyzer} = \dot{m}_{43}ex_{43} + \dot{m}_{44}ex_{44} \quad (4.94d)$$

Heat Exchanger-3 (35-36-18-19-21-22-24-25-27-28):

The mass, energy, entropy and exergy balance equations for heat exchanger Hx-3 are given as follows:

$$\dot{m}_{35} + \dot{m}_{19} + \dot{m}_{22} + \dot{m}_{25} + \dot{m}_{28} = \dot{m}_{36} + \dot{m}_{18} + \dot{m}_{21} + \dot{m}_{24} + \dot{m}_{27} \quad (4.95a)$$

$$\dot{m}_{35}h_{35} + \dot{m}_{19}h_{19} + \dot{m}_{22}h_{22} + \dot{m}_{25}h_{25} + \dot{m}_{28}h_{28} = \dot{m}_{36}h_{36} + \dot{m}_{18}h_{18} + \dot{m}_{21}h_{21} + \dot{m}_{24}h_{24} + \dot{m}_{27}h_{27} \quad (4.95b)$$

$$\dot{m}_{35}s_{35} + \dot{m}_{19}s_{19} + \dot{m}_{22}s_{22} + \dot{m}_{25}s_{25} + \dot{m}_{28}s_{28} + \dot{S}_{g,HX-4.} = \dot{m}_{36}s_{36} + \dot{m}_{18}s_{18} + \dot{m}_{21}s_{21} + \dot{m}_{24}s_{24} + \dot{m}_{27}s_{27} \quad (4.95c)$$

$$\dot{m}_{35}ex_{35} + \dot{m}_{19}ex_{19} + \dot{m}_{22}ex_{22} + \dot{m}_{25}ex_{25} + \dot{m}_{28}ex_{28} - \dot{Exd}_{HX-3} = \dot{m}_{36}ex_{36} + \dot{m}_{18}ex_{18} + \dot{m}_{21}ex_{21} + \dot{m}_{24}ex_{24} + \dot{m}_{27}ex_{27} \quad (4.95d)$$

The minimum required voltage by the electrolyzer is dependent on enthalpy difference between the products (hydrogen and oxygen) and reactant. The theoretical required voltage can be calculated as

$$V_{Electrolyzer} = \frac{\Delta H}{nF} \quad (4.96)$$

where “n” represents number of electrons taking part in the reaction (in water electrolysis n=2) and F is the faraday constant and its value is 96 485.3365 s A / mol. This completes the thermodynamic modeling of the system.

4.1.5 Exergoeconomic Modeling

Exergoeconomic analysis relate exergy analysis with cost. It is a very useful tool to evaluate the performance of the system in terms of cost. In present study, exergoeconomic analysis of the system has been performed. Cost balance equations are written for each of the components.

Generally cost balance equation consist of three sets of variable namely cost of input stream, capital and operating cost and cost of output stream. Different authors have defined different co-relations to relate capital and operating cost with the processing parameters.

Cost balance equations for each of the components are as follow

Pump -1 (1-2):

The cost balance equation for Pump-1 is given as follows:

$$c_1 \dot{m}_1 ex_1 + c_w \dot{W}_{P-1} + \dot{Z}_{P-1} = c_2 \dot{m}_2 ex_2 \quad (4.97)$$

PVT Module (3-10):

The cost balance equation for PV/T is given as follows:

$$c_{10} \dot{m}_{10} ex_{10} + \dot{Z}_{V-PVT} = c_3 \dot{m}_3 ex_3 \quad (4.98)$$

Valve # 2 (4-6):

The cost balance equation for Valve-2 is given as follows:

$$c_4 \dot{m}_4 ex_4 + \dot{Z}_{V-4} = c_6 \dot{m}_6 ex_6 \quad (4.99)$$

Valve # 1 (8-1):

The cost balance equation for Valve-1 is given as follows:

$$c_8 \dot{m}_8 ex_8 + \dot{Z}_{V-} = c_1 \dot{m}_1 ex_1 \quad (4.100)$$

Heat Exchanger-4 (2-10, 8-1):

The cost balance equation for Heat Exchanger-4 is given as follows:

$$c_2 \dot{m}_2 ex_2 + c_{10} \dot{m}_{10} ex_{10} + \dot{Z}_{HX-4} = c_8 \dot{m}_8 ex_8 + c_1 \dot{m}_1 ex_1 \quad (4.101)$$

Tank (8-9):

The cost balance equation for Tank are given as follows:

$$c_6 \dot{m}_6 ex_6 + \dot{Z}_{Tk} = c_5 \dot{m}_5 ex_5 \quad (4.102)$$

Turbine (13-14):

The cost balance equation for Turbine are given as follows:

$$c_{13} \dot{m}_{13} ex_{13} + \dot{Z}_T = c_{14} \dot{m}_{14} ex_{14} + c_w \dot{W}_T \eta_{mech} \eta_{gen} \quad (4.103)$$

Pump (11-12):

The cost balance equation for Pump-2 are given as follows:

$$c_{11}\dot{m}_{11}ex_{11} + \dot{Z}_{P-2} + c_w\dot{W}_{P-2} = c_{12}\dot{m}_{12}ex_{12} \quad (4.104)$$

Heat Exchanger-1(5-6, 12-13):

The cost balance equation for Heat Exchanger HX-1 are given as follows:

$$c_5\dot{m}_5ex_5 + c_{12}\,\dot{m}_{12}ex_{12} + \dot{Z}_{HX-1} = \dot{m}_6ex_6 + \dot{m}_{13}ex_{13} \quad (4.105)$$

Heat Exchanger-2(16-17, 14-15):

The cost balance equation for Heat Exchanger HX-2 are given as follows:

$$c_{17}\dot{m}_{17}ex_{17} + c_{14}\dot{m}_{14}ex_{14} + \dot{Z}_{HX-2} = c_{16}\dot{m}_{16}ex_{16} + c_{15}\dot{m}_{15}ex_{15} \quad (4.106)$$

Very high Temperature Generator-1 (11-15,18-19-20):

The cost balance equation for Very high Temperature generator D-1 are given as follows:

$$c_{18}\dot{m}_{18}ex_{18} + c_{15}\dot{m}_{15}ex_{15} + \dot{Z}_{D-1} = c_{19}\dot{m}_{19}ex_{19} + c_{20}\dot{m}_{20}ex_{20} + c_{11}\dot{m}_{11}ex_{11} \quad (4.107)$$

High Temperature Generator-2(20-21-22-23):

The cost balance equation for Very high Temperature generator D-2 are given as follows:

$$c_{21}\dot{m}_{21}ex_{21} + c_{20}\dot{m}_{20}ex_{20} + \dot{Z}_{D-2} = c_{22}\dot{m}_{22}ex_{22} + c_{23}\dot{m}_{23}ex_{23} \quad (4.108)$$

Medium Temperature Generator-3(23-24-25-26):

The cost balance equation for Very high Temperature generator D-3 are given as follows:

$$c_{24}\dot{m}_{24}ex_{24} + c_{23}\dot{m}_{23}ex_{23} + \dot{Z}_{D-3} = c_{25}\dot{m}_{25}ex_{25} + c_{26}\dot{m}_{26}ex_{26} \quad (4.109)$$

Low temperature Generator-4 (26-27-28-29):

The cost balance equation for Very high Temperature generator D-4 are given as follows:

$$c_{27}m_{27}ex_{27} + c_{26}\dot{m}_{26}ex_{26} + \dot{Z}_{D-4} = c_{28}\dot{m}_{28}ex_{28} + c_{29}\dot{m}_{29}ex_{29} \quad (4.110)$$

Condenser (29-30, 37-38):

The cost balance equation for condenser are given as follows:

$$c_{29}\dot{m}_{29}ex_{29} + c_{37}\dot{m}_{37}ex_{37} + \dot{Z}_{Cond} = c_{30}\dot{m}_{30}ex_{30} + c_{38}\dot{m}_{38}ex_{38} \quad (4.111)$$

Valve-2 (30-31):

The cost balance for equation Valve V-2 are given as follows:

$$c_{30}\dot{m}_{30}ex_{30} + \dot{Z}_{V-2} = c_{31}\dot{m}_{31}ex_{31} \quad (4.112)$$

Valve-3 (34-36):

The cost balance for equation Valve V-3 are given as follows:

$$c_{36}\dot{m}_{36}ex_{36} + \dot{Z}_{V-3} = c_{34}\dot{m}_{34}ex_{34} \quad (4.113)$$

Pump-3 (33-35):

The cost balance equation for Pump-3are given as follows:

$$c_{33}\dot{m}_{33}ex_{33} + \dot{Z}_{P-3} + c_w\dot{W}_{P-3} = c_{35}\dot{m}_{35}ex_{35} \quad (4.114)$$

Evaporator (31-32, 39-40):

The cost balance equation for evaporator are given as follows:

$$c_{31}\dot{m}_{31}ex_{31} + c_{39}\dot{m}_{39}ex_{39} + \dot{Z}_{Evp} = \dot{m}_{32}ex_{32} + \dot{m}_{40}ex_{40} \quad (4.115)$$

Absorber (32-33-34, 41-42):

The cost balance equation for absorber are given as follows:

$$c_{32}\dot{m}_{32}ex_{32} + c_{34}\dot{m}_{34}ex_{34} + c_{41}\dot{m}_{41}ex_{41} + \dot{Z}_{Abs} = c_{33}\dot{m}_{33}ex_{33} + c_{42}\dot{m}_{42}ex_{42} \quad (4.116)$$

Expansion Valve (34-36):

The cost balance equation for Expansion Valve V-3 are given as follows:

$$\dot{m}_{36}ex_{36} + \dot{Z}_{V-3} = \dot{m}_{34}ex_{34} \quad (4.117)$$

Electrolyzer (43-44-45)

The cost balance equation for Electrolyzer are given as follows:

$$c_{45}\dot{m}_{45}ex_{45} + c_w\dot{W}_{Electrolyzer} + \dot{Z}_{Electrolyzer} = c_{43}\dot{m}_{43}ex_{43} + c_{44}\dot{m}_{44}ex_{44} \quad (4.118)$$

The capital cost rate of each of the above mentioned equipment is taken from literature [60] and they are given as follows:

$$\text{Turbine} = \dot{Z}_T = \left(4750\dot{W}^{0.75} + 60\dot{W}^{0.75}\right)CRF \quad (4.119)$$

$\dot{W}$ represents mechanical work output in Eq. 4.119

$$\text{Heat Exchangers} = \dot{Z}_{HX} = (80Q^{0.85})CRF \quad (4.120)$$

Q represents amount of heat exchanged between fluids in Eq. 4.120

$$\text{Valve} = \dot{Z}_V = \left(37\left(\frac{P_{out}}{P_{in}}\right)^{0.68}\right)CRF \quad (4.121)$$

P_{in} represents inlet pressure of the valve, P_{out} represents outlet pressure in Eq. 4.121

$$\text{PVT} = \dot{Z}_{PVT} = (150N_{mod} + 25Co_f)CRF \quad (4.122)$$

N_{mod} represents total number of modules, Co_f represents concentration factor in Eq. 4.122

Tank= $\dot{Z}_{Tk} = (350\dot{m})CRF$ (4.123)

$\dot{m}$ represents total inlet flow rate in Eq. 4.123

Electrolyzer= $\dot{Z}_{Electrolyzer} = (1000\dot{W})CRF$ (4.124)

$\dot{W}$ represents total electrical work input to the electrolyzer in Eq. 4.124

Generator= $\dot{Z}_D = (1250\dot{m})CRF$ (4.125)

$\dot{m}$ represents mass flow rate of brine entering into the generator in Eq. 4.125

where CRF represents capital recovery factor and can be calculated as

$$CRF = \frac{\left(\frac{q^{k+CP}-1}{(q-1)(q^{k+CP})} - \frac{q^{CP}-1}{(q-1)q^{CP}}\right)^{-1} \phi}{3600N_o} \quad (4.126)$$

where CP represents construction period (in years) and its value is set to 1 in present analysis, k represents amortization period (in years), N_o represents total number of operational hours in one year, ϕ represents maintenance factor and set to 1.06, q is a function of inflation and interest rate and can be calculated as

$$q = \left(1 + \frac{in}{100}\right)(1 + ri) \quad (4.127)$$

where 'in' represents interest rate and ri represents inflation rate. Both of them in %. This complete the exergoeconomic modeling of the system.

4.1.6 Efficiency Analysis

For present system, 1st and 2nd law efficiencies are defined as below

$$\eta_{en} = \frac{\dot{W}_{Net} + \dot{m}_{16}(h_{16} - h_{17}) + \dot{m}_{43}HHV_{H2} + \dot{m}_{39}(h_{39} - h_{40})}{\dot{Q}_{in,Solar}} \quad (4.128)$$

The exergy efficiency can be defined as

$$\eta_{exe} = \frac{\dot{W}_{Net} + \dot{m}_{16}(ex_{16} - ex_{17}) + \dot{m}_{43}ex_{H2}^{ch} + \dot{m}_{39}(ex_{39} - ex_{40})}{\dot{Q}_{in,Solar}\left(1 - \frac{T_0}{T_{Sun}}\right)} \quad (4.129)$$

where HHV_{H2} represents the higher heating value of hydrogen and its value is 141.80 MJ/kg, ex_{H2}^{ch}represents the chemical exergy of hydrogen and its value is 236.1 MJ/kmol, T_{Sun} represents the surface temperature of Sun and its value is taken as 5000K, $\dot{W}_{Net}$ represents the network output and $\dot{Q}_{in,Solar}$ represents the total solar energy concentrated on PV panels. The network output can be calculated as

$$\dot{W}_{Net} = \dot{W}_T + \dot{W}_{PVT} - \dot{W}_{P-1} - \dot{W}_{P-2} - \dot{W}_{P-3} \quad (4.130)$$

Total input solar energy can be calculated as

$$\dot{Q}_{in,Solar} = \eta_{optical} w l N_{mod} G_\beta \quad (4.131)$$

where $\eta_{optical}$ represents the optical efficiency and its value is taken as 0.85 in present study, w is the width of each PV/T module, l represents the length of PV/T module, N_{mod} is the total number of modules and G_β represents the total concentrated solar irradiance.

4.1.7 Exergoenvironmental Modeling

Environmental impact of different exergy systems are usually expressed in number of different parameters which relate useful exergy with exergy destruction and plant efficiency. In present study following parameters are considered.

4.1.7.1 Exergoenvironmental impact factor

The exergoenvironmental impact factor is used to find the positive effect of the studied system on the environment. The main reason of studying this parameter is that it helps in reducing the environmental effect of the system by reducing the irreversibilities in the system. The ideal value of exergoenvironmental impact factor is "zero" which represents that system has zero irreversibilities. Mathematically, the exergoenvironmental impact factor is defined as

$$f_{ei} = \frac{\dot{E}x_{des,tot}}{\dot{E}_{x_{in}}} \quad (4.132)$$

where f_{ei}, $\dot{E}x_{des,tot}$ and $\dot{E}_{x_{in}}$ represent exergoenvironmental impact factor, total exergy destruction in the system, and total input exergy, respectively.

4.1.7.2 Exergoenvironmental impact coefficient

The exergoenvironmental impact coefficient is associated to the exergy efficiency of the system. Its value is one under ideal conditions. This means system is working under such conditions which has exergy efficiency of one (i.e. with zero irreversibility). Mathematically, this coefficient is defined as

$$C_{ei} = \frac{1}{\eta_{exe}} \quad (4.133)$$

where C_{ei} and η_{ex} represent exergoenvironmental impact coefficient and exergy efficiency, respectively.

4.1.7.3 Exergoenvironmental impact index

The exergoenvironmental impact index shows whether or not the system under consideration harms the environment due to its unusable waste exergy output and exergy destruction. Smaller values of exergoenvironmental impact index is desirable. Mathematically, the exergoenvironmental impact index is computed by multiplying exergoenvironmental impact coefficient and exergoenvironmental impact factor and is written as

$$\theta_{ei} = f_{ei} \times C_{ei} \tag{4.134}$$

where θ_{ei} represents exergoenvironmental impact index.

4.1.7.4 Exergoenvironmental impact improvement

The exergoenvironmental impact improvement parameter determines the environmental suitability of the studied system. Exergoenvironmental impact index should be minimized in order to improve the environmental suitability of the system. The smaller value of exergoenvironmental impact improvement means the system under consideration has high exergy destruction. Mathematically, it is defined as

$$\theta_{eii} = \frac{1}{\theta_{ei}} \tag{4.135}$$

where θ_{eii} represents exergoenvironmental impact improvement.

4.1.7.5 Exergetic stability factor

The exergetic stability factor depends on the net useful output exergy, net exergy destruction and net unused exergy from the source. The ideal value for this factor is one. Mathematically, this factor is defined as

$$f_{es} = \frac{\dot{E}x_{tot,out}}{\dot{E}x_{tot,out} + \dot{E}x_{des,tot} + \dot{E}x_{uu}} \tag{4.136}$$

where f_{es} and $\dot{E}x_{uu}$ shows exergetic stability factor and exergy carried by unused fuel.

4.1.7.6 Exergetic sustainability index

The exergetic sustainability index is the product of exergetic stability factor and exergoenvironmental impact improvement of the investigated system. The higher the value of exergetic sustainability index, the better it is form environmental prospective. Mathematically, this index is defined as

$$\theta_{est} = f_{es} \times \theta_{eii} \tag{4.137}$$

where θ_{est} represents exergetic sustainability index.

4.1.8 Evniroeconomic (environmental cost) analysis

When we produce power/electricity from fossil fuel, it produces a lot of hazardous of gases specially CO_2 which is harmful for environment and living beings. The enviroeconomic analysis is based upon price of CO_2 emission into the environment, which is the most powerful mechanism to promote the deployment of renewable energy technologies that does not emit carbon to the atmosphere. If coal is being used to produce electricity then 960g CO_2/kWh is being released but due to losses, 40% in transmission and distribution and 20% in ineffective electrical equipment the actual amount of produced CO_2 is 2.0kg/kWh. Therefore, CO_2 mitigation per annum from the hybrid PVT array can be estimated as

$$\phi_{co_2} = \frac{\psi_{co_2} \times \dot{E}_{overall}}{10^3} \tag{4.138}$$

where ϕ_{co_2} where is CO_2 mitigation per annum (tCO_2/annum), ψ_{co_2} is the average CO_2 equivalent intensity for electricity generation from coal (2.0 $kgCO_2$/kW h) and $\dot{E}_{overall}$ is the annual overall energy/exergy produced (kW h) from the hybrid PVT array per annum. For high and low pledge scenario the international price of CO_2 is between 13 \$/tCO_2 - 16 \$/tCO_2. So the average is 14.5 \$ tCO_2. The environmental cost is given as

$$\dot{Z}_{co_2} = Z_{co_2} \times \phi_{co_2} \tag{4.139}$$

where $\dot{Z}_{co_2}$ is the evniroeconomic (environmental cost) parameters CO_2 (mitigation price per annum) (\$/annum) and Z_{co_2} is the carbon price per tCO_2 (14.5 \$/ tCO_2).

4.1.8 Optimization

The following five parameters, namely, pressure in primary loop, pressure and temperature of organic Rankine cycle, pressure and temperature of ammonia water chiller system have been varied in order to investigate their effect on energy and exergy efficiencies, cost of electricity, enviro economic parameter and on different exergoenvironmental factors. The three main objectives of the optimization is to come up with such a parameters at which system will have maximum efficiency, minimum cost, and minimum environmental impact. Three output variables, namely, exergy efficiency, cost coefficient of electrical work output and exergoenvironmental impact coefficient are chosen for optimization. Based on the parametric study data, three objective

functions are formed by performing curve fitting on the data. Design- expert ® is used for curve fitting (Regression process).

There are the three objective functions that are to be optimized in this study. Multi Objective Genetic algorithm is used to get the optimum value of these function for a given box-constraints. As mentioned earlier, the objective is to find optimal values of decision variables at which exergy efficiency is maximized, cost of electricity is minimized with minimum environmental impact. The objective functions of exergy efficiency, cost coefficient of electricity and environmental impact coefficient are functions of pressure in primary loop, pressure in secondary loop, temperature in secondary loop, pressure in absorption chiller and temperature of absorption chiller. The units of cost coefficient is $/kWh. Mathematically, the objective functions are given as

$$\eta_{\text{exergy}} = +0.30082 - 1.13307\text{e}^{-6} * \text{P2} - 3.24019\text{e}^{-6} * \text{P12} + 2.25705\text{e}^{-4} * \text{T13} - 4.77408\text{e}^{-4} * \text{P18} + 1.45067\text{e}^{-5} * \text{T40} + 4.98103\text{e}^{-9} * \text{P12} * \text{T13} - 7.80025\text{e}^{-10} * \text{P12} * \text{P18} + 6.70516\text{e}^{-7} * \text{T13} * \text{P18} \quad (4.140)$$

$$\text{c}_{\text{W}} = -6.33145\text{e}^{-3} + 7.50667\text{e}^{-9} * \text{P2} + 2.71993\text{e}^{-7} * \text{P12} + 1.64498\text{e}^{-5} * \text{T13} - 3.31707\text{e}^{-9} * \text{P18} - 5.01520\text{e}^{-10} * \text{P12} * \text{T13} \quad (1.141)$$

$$\text{C}_{\text{ei}} = +11.47675 + 5.90000\text{e}^{-6} * \text{P2} + 3.38776\text{e}^{-5} * \text{P12} - 0.033739 * \text{T13} + 4.60871\text{e}^{-3} * \text{P18} - 1.06267\text{e}^{-4} * \text{T40} + 5.77236\text{e}^{-9} * \text{P2} * \text{P18} - 5.58126\text{e}^{-8} * \text{P12} * \text{T13} + 1.04480\text{e}^{-8} * \text{P12} * \text{P18} - 7.62117\text{e}^{-6} * \text{T13} * \text{P18} - 2.53029\text{e}^{-10} * \text{P12}^2 + 3.13267\text{e}^{-5} * \text{T13}^2 + 3.71192\text{e}^{-7} * \text{P18}^2 \quad (1.142)$$

As stated earlier, there are five variable in the objective function equations, i.e., P2, P12, P18, T13, and T40. The optimization box-constraints on the decision variables are given as:

$$150 \leq P2 \leq 350$$

$$2000 \leq P12 \leq 5000$$

$$510 \leq T13 \leq 550$$

$$250 \leq P18 \leq 600$$

$$280 \leq T40 \leq 288$$

The constraints and their ranges are also tabulated in Table 4.5.

Table 4.5: Decision variable ranges (called box-constraints)

Variable	Minimum Value	Maximum Value
Pressure in primary loop "P2" (kPa)	150	350
Pressure in secondary loop "P12" (kPa)	2000	5000
Temperature in secondary loop "T13" (K)	510	550
Pressure in absorption chiller "P18" (kPa)	250	600
Temperature in absorption chiller "T40"(K)	280	288

Increasing exergy mean that system is more efficient and more net output work. Minimizing cost coefficient of work make the system economically more feasible and minimizing coefficient of environmental impact mean that system is less irreversibilities. Ideal value of this objective is "zero" which shows that system has no irreversibilities.

The optimization is performed using well-known NSGA-II algorithm. Depending upon the objective or constraints there are two types of robust optimizations "objective robustness" or "feasibility robustness". The main goal for objective robustness is to seek a design solution whose values almost remain the same regardless of reasonable variability of decision variables. The main purpose of feasibility robustness is to design a feasible solution regardless of the variability. Sometime feasibility also referred as reliability, feasibility robust optimization is also called reliability optimization [85-.104]. For sensitivity analysis, the values of optimal solutions are varied up to 3% by following the algorithm presented in [102-104]:

$\min/\max f_i(x_1, x_2, x_3 \dots \dots x_n) \quad i = 1,2,3..$ Nominal NSGA-II optimal solution

where

$X_{min} \leq x_1, x_2, x_3 \leq X_{max}$ Variable ranges

Subjected to

$$|f_i(x_1, x_2, x_3 \dots \dots x_n) - f_i^*(x_1, x_2, x_3 \dots \dots x_n)| - \Delta f_{a_n} \leq 0$$

$f_i^*(x_1, x_2, x_3 \dots \dots x_n)$ represents the value of objective function when then value of decision variable is varied N% and Δf_{a_n} represents the maximum acceptable variation in output value. In

present, study, six different cases are investigated. Table 4.6 shows the maximum acceptable difference in objective function values. In first five cases values of decision variables are varied up individually to check the sensitivity of the optimized solution with respect to the variable. In case 6, all the variables are sententiously simultaneously varied. If the variable sensitivity is low for Pareto frontier solution, then it means changing that variable do not have significant effect on the performance of the solution and vice versa.

Table 4.6: Maximum acceptable difference for the objective function

Variable	Maximum acceptable difference
$\Delta\eta_{exergy}$	0.05
Δc_W	0.0005
ΔC_{ei}	0.1

Case-1

P_2 is varied upto 3% of its nominal optimal value and see it effect to the to the system. How much it exergy efficiency, cost of work and cost of environmental impact change.

$$|\eta_{exergy}(P_2, P_{12}, T_{13}, P_{18}, T_{40}) - \eta_{exergy}(P_2^*, P_{12}, T_{13}, P_{18}, T_{40})| - \Delta\eta_{exergy} \leq 0 \quad (4.143)$$

$$|c_W(P_2, P_{12}, T_{13}, P_{18}, T_{40}) - c_W(P_2^*, P_{12}, T_{13}, P_{18}, T_{40})| - \Delta c_W \leq 0 \quad (4.144)$$

$$|C_{ei}(P_2, P_{12}, T_{13}, P_{18}, T_{40}) - C_{ei}(P_2^*, P_{12}, T_{13}, P_{18}, T_{40})| - \Delta C_{ei} \leq 0 \quad (4.145)$$

Case-2

P_{12} is varied upto 3% of its nominal optimal value and see it effect to the to the system. How much it exergy efficiency, cost of work and cost of environmental impact change.

$$|\eta_{exergy}(P_2, P_{12}, T_{13}, P_{18}, T_{40}) - \eta_{exergy}(P_2, P_{12}^*, T_{13}, P_{18}, T_{40})| - \Delta\eta_{exergy} \leq 0 \quad (4.146)$$

$$|c_W(P_2, P_{12}, T_{13}, P_{18}, T_{40}) - c_W(P_2, P_{12}^*, T_{13}, P_{18}, T_{40})| - \Delta c_W \leq 0 \quad (4.147)$$

$$|C_{ei}(P_2, P_{12}, T_{13}, P_{18}, T_{40}) - C_{ei}(P_2, P_{12}^*, T_{13}, P_{18}, T_{40})| - \Delta C_{ei} \leq 0 \quad (4.148)$$

Case-3

T_{13} is varied upto 3% of its nominal optimal value and see it effect to the to the system. How much it exergy efficiency, cost of work and cost of environmental impact change.

$$|\eta_{exergy}(P_2, P_{12}, T_{13}, P_{18}, T_{40}) - \eta_{exergy}(P_2, P_{12}, T_{13}^*, P_{18}, T_{40})| - \Delta\eta_{exergy} \leq 0 \quad (4.149)$$

$$|c_W(P_2, P_{12}, T_{13}, P_{18}, T_{40}) - c_W(P_2, P_{12}, T_{13}^*, P_{18}, T_{40})| - \Delta c_W \leq 0 \quad (4.150)$$

$$|C_{ei}(P_2, P_{12}, T_{13}, P_{18}, T_{40}) - C_{ei}(P_2, P_{12}, T_{13}^*, P_{18}, T_{40})| - \Delta C_{ei} \leq 0 \quad (4.151)$$

Case-4

P_{18} is varied upto 3% of its nominal optimal value and see it effect to the to the system. How much it exergy efficiency, cost of work and cost of environmental impact change.

$$|\eta_{exergy}(P_2, P_{12}, T_{13}, P_{18}, T_{40}) - \eta_{exergy}(P_2, P_{12}, T_{13}, P_{18}^*, T_{40})| - \Delta\eta_{exergy} \leq 0 \quad (4.152)$$

$$|c_W(P_2, P_{12}, T_{13}, P_{18}, T_{40}) - c_W(P_2, P_{12}, T_{13}, P_{18}^*, T_{40})| - \Delta c_W \leq 0 \quad (4.153)$$

$$|C_{ei}(P_2, P_{12}, T_{13}, P_{18}, T_{40}) - C_{ei}(P_2, P_{12}, T_{13}, P_{18}^*, T_{40})| - \Delta C_{ei} \leq 0 \quad (4.154)$$

Case-5

T_{40} is varied upto 3% of its nominal optimal value and see it effect to the to the system. How much it exergy efficiency, cost of work and cost of environmental impact change.

$$|\eta_{exergy}(P_2, P_{12}, T_{13}, P_{18}, T_{40}) - \eta_{exergy}(P_2, P_{12}, T_{13}, P_{18}, T_{40}^*)| - \Delta\eta_{exergy} \leq 0 \quad (4.155)$$

$$|c_W(P_2, P_{12}, T_{13}, P_{18}, T_{40}) - c_W(P_2, P_{12}, T_{13}, P_{18}, T_{40}^*)| - \Delta c_W \leq 0 \quad (4.156)$$

$$|C_{ei}(P_2, P_{12}, T_{13}, P_{18}, T_{40}) - C_{ei}(P_2, P_{12}, T_{13}, P_{18}, T_{40}^*)| - \Delta C_{ei} \leq 0 \quad (4.157)$$

Case-6

Values of all 5 variables $(P_2, P_{12}, T_{13}, P_{18}, T_{40})$ are varied upto 3% of their nominal optimal value and see it effect to the system. How much it exergy efficiency, cost of work and cost of environmental impact change.

$$|\eta_{exergy}(P_2, P_{12}, T_{13}, P_{18}, T_{40}) - \eta_{exergy}(P_2^*, P_{12}^*, T_{13}^*, P_{18}^*, T_{40}^*)| - \Delta\eta_{exergy} \leq 0 \quad (4.158)$$

$$|c_W(P_2, P_{12}, T_{13}, P_{18}, T_{40}) - c_W(P_2^*, P_{12}^*, T_{13}^*, P_{18}^*, T_{40}^*)| - \Delta c_W \leq 0 \quad (4.159)$$

$$|C_{ei}(P_2, P_{12}, T_{13}, P_{18}, T_{40}) - C_{ei}(P_2^*, P_{12}^*, T_{13}^*, P_{18}^*, T_{40}^*)| - \Delta C_{ei} \leq 0 \quad (4.160)$$

Chapter 5: Results and Discussion

In this chapter, results of radiation modeling, I-V modeling, I-V thermal modeling, thermodynamic and efficiency analysis, exergoeconomic modeling, exergoenvironmental analysis and enviro economics analysis are explained. Five parameters namely pressure in primary loop, pressure and temperature of organic Rankine cycle, pressure and temperature of ammonia water chiller system are varied in order to examine their effect on energy and exergy efficiencies, cost of electricity, enviro economic parameter and on different exergoenvironmental factors.

5.1 Radiation Modeling Results

In this section, the results of radiation model are presented. The details of radiation modeling is given in section 4.1.1.

5.1.1 Radiation Intensity

The radiation model is presented in section 4.1. For sake of analysis, city of Toronto is chosen. The geographical location of Toronto is 79.404^o longitude and 46.64^o is the latitude. The standard time difference between Greenwich Mean Time and Toronto is +5 hours. Standard meridian is 75^o. During the modeling the ozone layer thickness is taken as 0.35 and average dew point temperature is assumed as 10^o. β_2 is taken as 1.3 and for analysis purpose β_1 is taken as 0. Figure 5.1 shows the radiation intensity in the city of Toronto for a clear sky model. The curve is sinusoidal. It increases in start and then start decreasing at the end of the day. Radiation intensity is maximum between 12:00 P.M and 1:00 P.M and during the middle of the year. It value increases as high as 750 W/m^2 at 30^o inclined angle. For example at 180th day of the year and at 12:00 P.M total radiation falling on the PV/T panel is 684.7 W/m^2. The normal direct radiation is 709.3 W/m2 out of which beam component is 663.9W/m^2 and diffuse component is 67.92W/m^2. For those calculations ground reflectance is assumed as 0.5. In the cloudy or turbid day, the value of β_1 increases up to 0.4 and the amount of radiation falling on the surface of the PV/T decreases. It is therefore utmost important to select that geographical location which has minimum number of turbid days. The model presented in section 4.1 can be used to predict the solar irradiation at any geographical location on the globe. Table 5.1 shows the values of other different parameters calculated using the radiation modeling and are used to calculate the final value of radiation falling on the PV/T panel.

Table 5.1: Calculated and/or assumed values for different parameters used in radiation modeling

Variable	Value	Variable	Value
α_s	69.38	P_0 (kPa)	101.3
B_1	97.64	φ	0.715
β_1	0	P_I	101325
B_2	1.3	ρ_a	0.07701
δ	23.24	ρ_g	0.24
Δt	5	r_r	0.8272
D_a	26.98	ST	12.24
D_m	13.53	T_0 (K)	300
D_r	27.41	τ_a	0.945
ET	-3.087	τ_{aa}	0.9981
E_{io}	1.035	τ_{as}	0.9468
F_c	0.84	τ_g	0.9872
Γ	0.4904	τ_o	0.981
I_b (W/m^2)	663.9	τ_r	0.9091
I_d (W/m^2)	67.92	τ_w	0.618
I_n (W/m^2)	709.3	θ_z	20.62
I_{sc} (W/m^2)	1367	T_{dew} (K)	283
I_t (W/m^2)	787.9	U_1	4.859×10^6
LT	12	U_3	0.3737
L_L	79.4	V_{is}	336.7
L_{oz}	0.35	W_a	4.551×10^6
L_s	75	ϖ	4.771×10^6
m_a	1.068	ξ	46.64
m_r	1.0068	ν	0.5
Nd	180	ω	-3.632

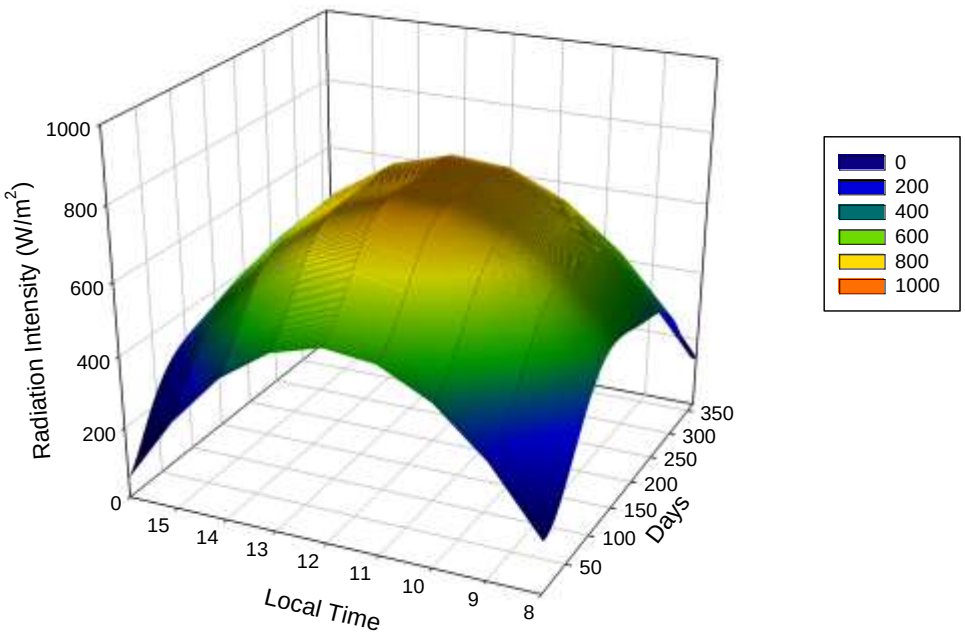

Figure 5.1: Radiation intensity from 8:00 A.M to 4:00 P.M throughout the year in Toronto, ON, Canada, for a clear sky

5.1.2 Effect of Tilt Angle on Radiation Intensity

Changing the tilt angle changes the radiation falling on an object (PV/T panel in present study). Figure 5.2 shows the effect of tilt angle on the radiation intensity at 12:00 P.M throughout the year. Increasing the tilt angle increases the radiation intensity until it reaches 30^{o}. After 30^{o} the radiation intensity starting to decrease. By looking at Eq's 4.2 and 4.3, it can easily be predicted that increasing the tilt angle beyond a certain value, decreases the radiation intensity. Figure 5.3 shows the effect of tilt angle on the PV/T panel surface at 180th day of the year from 8:00 A.M to 5:00 P.M. The tilt angle is varied from 5^{o} to 90^{o}. Radiation intensity is minimum at 90^{o} and maximum at 30^{o}. Eq's 4.5, 4.23 and 4.30 indicate the fact that changing the tilt angle do not affect the value of diffused, normal and beam component. Evo Energy [105] have tested their PV panels at number of different tilt angles and their results also suggest that the optimum angle for the PV panel is 30^{o} which actually confirms the results predicted by the model used in present study.

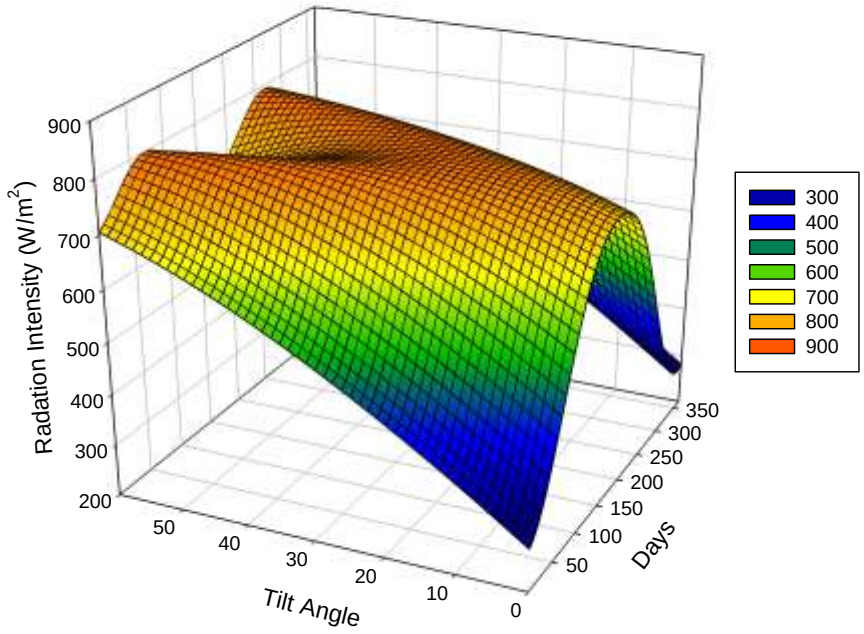

Figure 5.2: Radiation intensity at different tilt angles

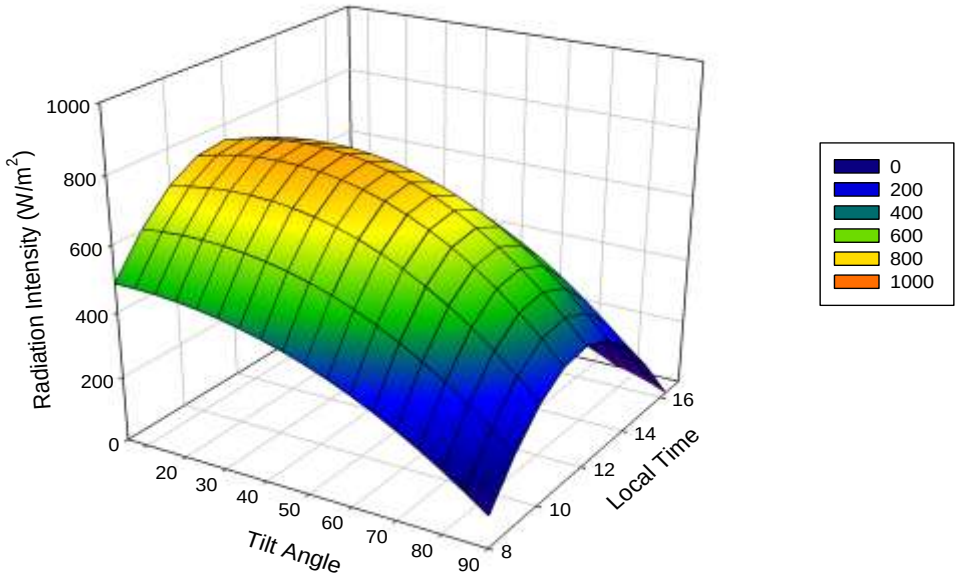

Figure 5.3: Radiation intensity at different tilt angles

5.2 I-V Modeling Results

In this section, the results of I-V electrical model is presented. A static and dynamic model is considered. Effect of different parameters on current and voltage is investigated. The detail I-V modeling is given in section 4.1.2.

5.2.1 I-V Characteristic Curve

The voltage and current output of the PV module is estimated using Eq. 4.38. When the light is concentrated on the PV panel it decreases the voltage of the panel (V_{PVN}) and increases the current of the panel (I_{PVN}). The advantage of GaAs compared to silicon cells is that they can withstand high temperature without any significant change in their efficiency. Figure 5.4 shows the I-V characteristic of the GaAs cells.

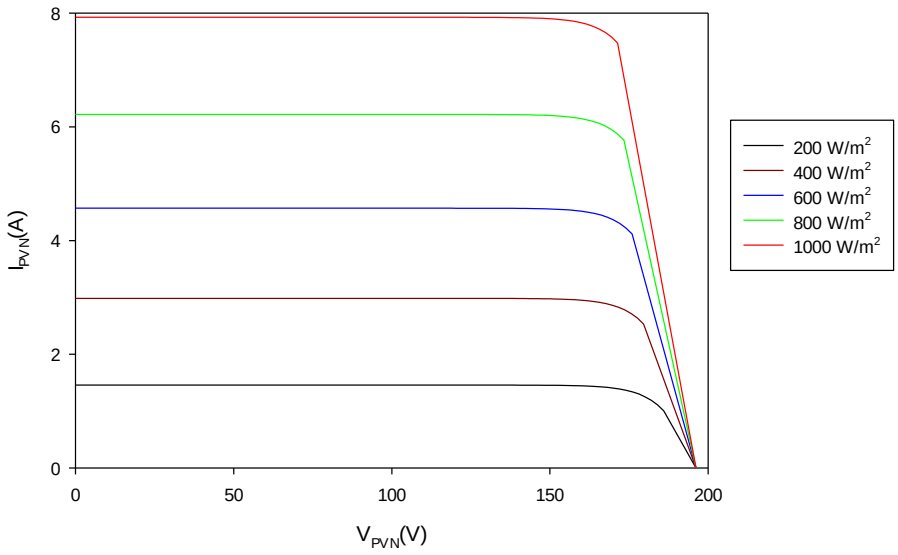

Figure 5.4: Effect of radiation intensity on I-V characteristic of GaAs photovoltaics array.

It is also important to mention here that depending upon different doping layers during the manufacturing of the cell, the temperature dependant voltage coefficient and temperature dependant current coefficient also changes. The temperature dependant coefficient is also a function of temperature of cell however because of lack of availability of data it is used as constant. Table 4.4 shows different characteristics of the cells used in analysis of present energy system. Increasing the radiation intensity increases the current output of the module. At 0V, the PV panel act as a short electrical circuit where current is maximum. At a given intensity, changing the

voltage does not have significant effect on the current of the panel. However, when the voltage is near to its open circuit voltage of the panel than the current drops sharply and reaches zero at the maximum output voltage. This is known as “Open circuit voltage”. The short circuit current for the modules considered in present study is 7.92 (A) and open circuit voltage is 196V at radiation intensity of 1000 W/m^2.

5.2.2 Effect of Solar Concentration and Radiation Intensity

Figure 5.5 shows the effect of radiation intensity and solar concentration on the PV module current. As indicated in Figure 5.4, increasing the radiation intensity actually increases the total energy input into the system which ultimately results in increase in electrical power output from the module.

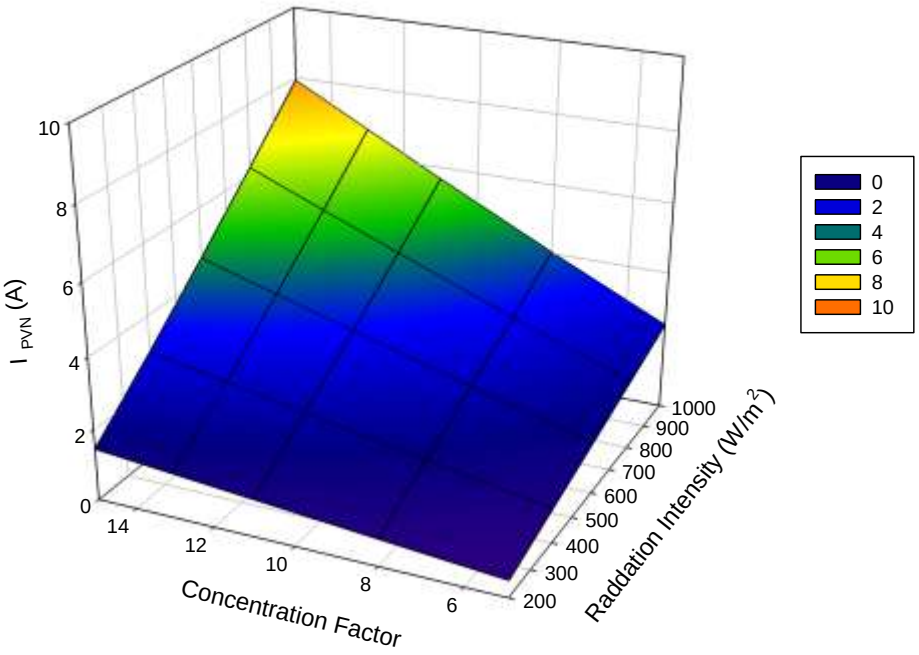

Figure 5.5: Effect of radiation intensity and concentration factor on photovoltaic module output current.

The increase in output power from the module is because of increase in current of the module. By increasing the concentration factor, the amount of energy input per square inch increases which results increasing in PV module current. In present analysis, the concentration ratio is varied from

5 to 15 as increasing the concentration beyond that will increase the cell temperature beyond the acceptable limit described in literature which ultimately have negative effect on the cell efficiency and in some cases higher concentration ratio results in cell melts down as well. The maximum current is at a concentration factor of 15 and at a radiation intensity of 1000W/m^2. The increase in current can be described from Eq.s 4.43 and 4.45. Increasing the radiation intensity or concertation factor also increases cell temperature which results increasing in current by 0.00019 A/K.

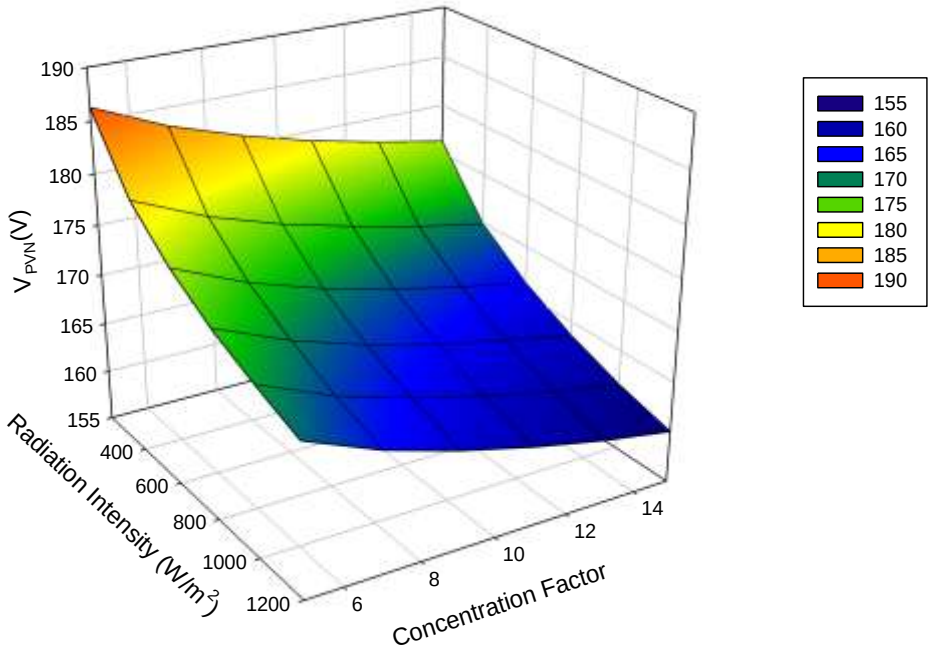

Figure 5.6: Effect of radiation intensity and concentration factor on photovoltaic module output voltage.

The current and voltage of output from the module works quite oppositely. It is also dependent upon the configuration in which cells are placed. In present analysis, the module produces a fix amount of electrical power output. Increasing the current, decreases the voltage. Figure 5.6 shows the effect of radiation intensity and concentration factor on photovoltaic module output voltage. The voltage is varied from 200 W/m^2 to 1200 W/m^2 and concentration factor is varied from 5 to 15. Maximum voltage of 186.2V is at 200 W/m^2 and at a concentration factor of 5. As the radiation intensity increases, voltage drops and it is not linear as shown by Eq. 4.46, it follows a natural log-athematic trend.

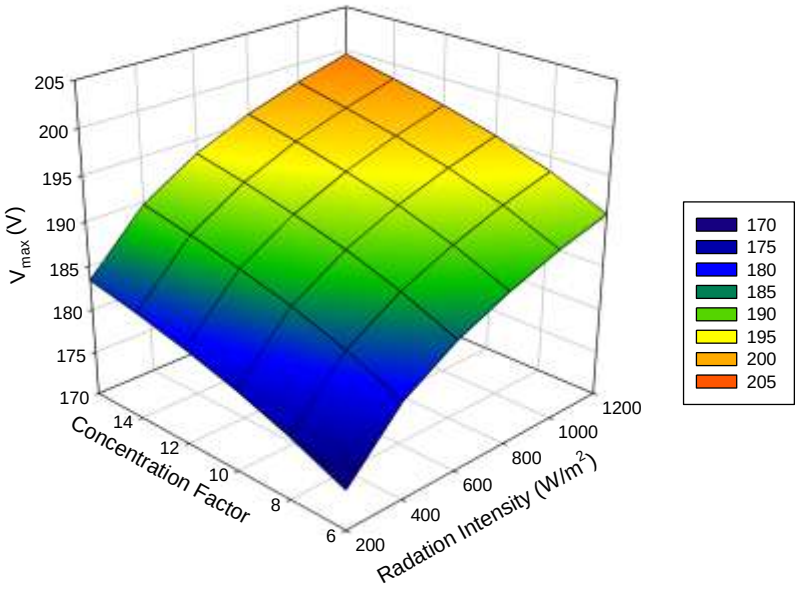

Figure 5.7: Effect of radiation intensity and concentration factor on photovoltaic module maximum voltage.

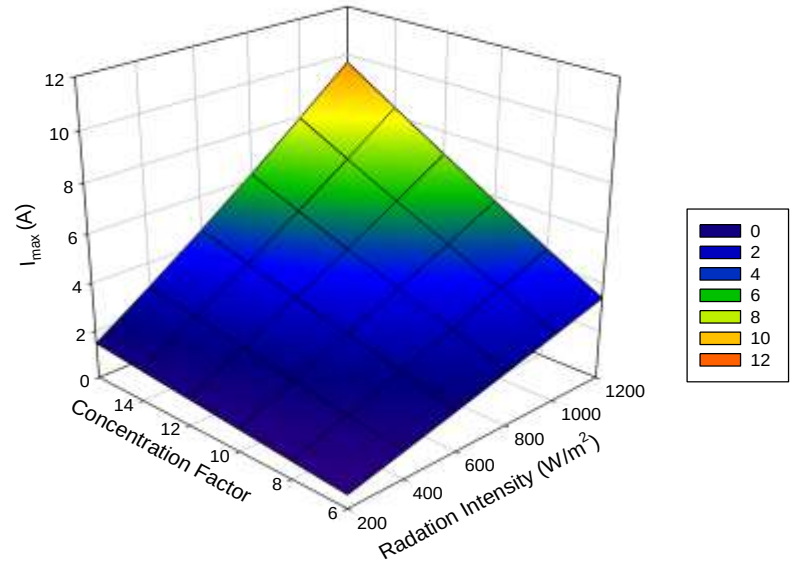

Figure 5.8: Effect of radiation intensity and concentration factor on photovoltaic module maximum current.

Increasing the radiation intensity also increases the cell temperature which results in lower voltage (as indicated by the 2nd term in Eq. 4.46, the decrease in cell voltage with increase in cell temperature is 0.00204V/K). Figure 5.7 is actually the graphical form of Eq. 4.49. It shows the effect of radiation intensity and concentration factor on the maximum module output voltage. The first term in the Eq. 4.49 is responsible for increasing trend (i.e. with increase in radiation intensity and concentration factor the maximum voltage of the module increases). However, as stated earlier, due to the concertation of radiation on the PV panel, temperatures in present study are beyond the normal working temperatures (i.e. generally most PV cells operate between 0^{o}C to 70^{o}C max.). The increase in cell temperature results decreasing maximum voltage because of the negative temperature dependant voltage coefficient (2^{nd} term on R.H.S of Eq. 4.49). The effect of 2^{nd} term is small compared to the 1^{st} term in Eq. 4.49 which results in overall increase in maximum output voltage of the module.

In case of maximum current, it increases with increase in radiation intensity or concentration factor. This is because of the positive value of temperature dependant current coefficient. Figure 5.8 shows the effect of radiation intensity and concentration factor on photovoltaic module maximum current.

5.2.3 Dynamic I-V Model

Figure 5.9 shows the photovoltaic module voltage between 8:00 A:M to 4:00 P.M throughout the year for a clear sky model and for city of Toronto. For sake of analysis, a concentration factor of 15 is used. These graphs are generated by integrating radiation model with the I-V model. As the radiation intensity changes throughout the day which effects the module current and voltage. The voltage is maximum in start and at the end of the day during the winter session. As the days get longer, voltage reduces. The explanation is similar to Figure 5.6. Increasing the light intensity reduces the cell voltage. The voltage is minimum during the summer and especially in afternoon when the radiation intensity is maximum. Figure 5.10 shows the photovoltaic module current between 8:00 A:M to 4:00 P.M throughout the year for a clear sky model and for city of Toronto. A similar concentration factor as of Figure 5.9 is used (i.e. concentration factor of 15). As indicated in Figure 5.5, the current increases with increase in radiation intensity. The current is maximum during the afternoon hours and summer session.

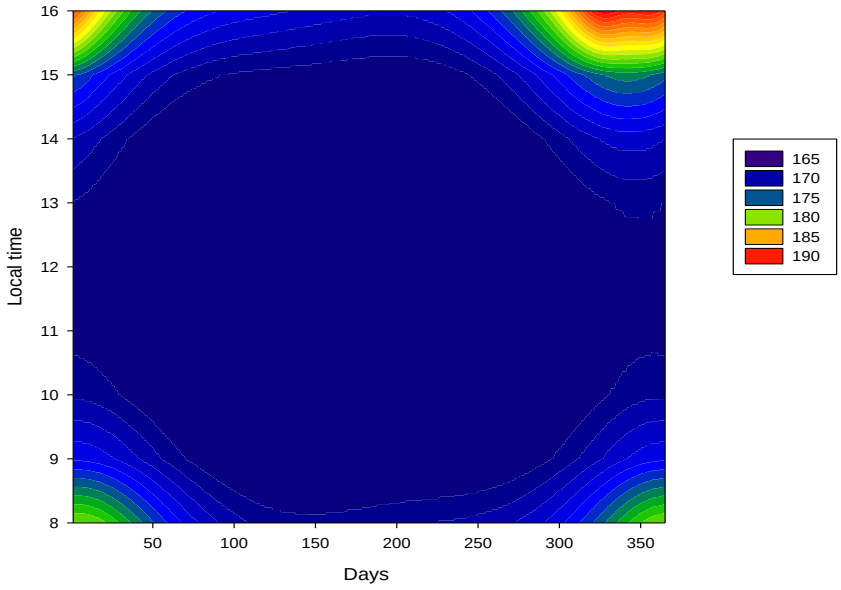

Figure 5.9: Photovoltaic module voltage between 8:00 A.M to 4:00 P.M throughout the year for a clear sky.

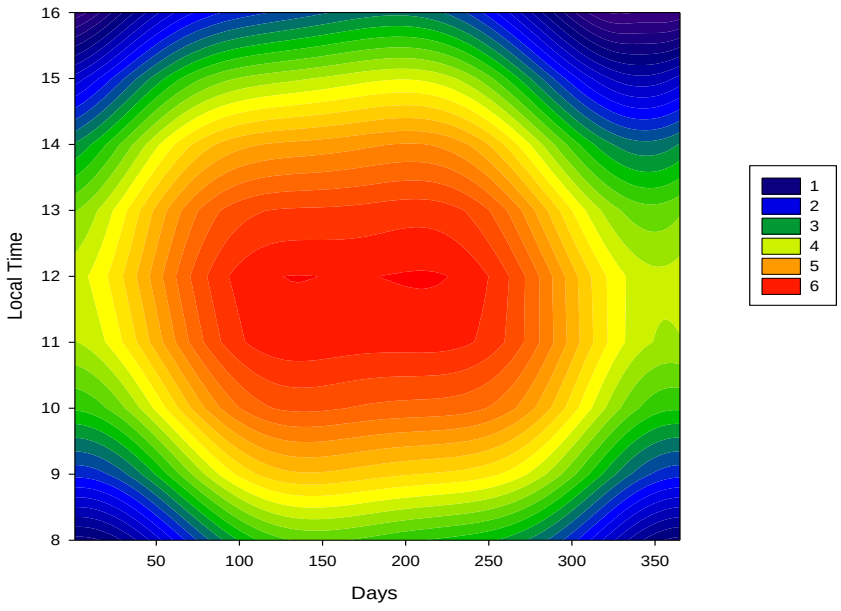

. Figure 5.10: Photovoltaic module current between 8:00 A.M to 4:00 P.M throughout the year for a clear sky.

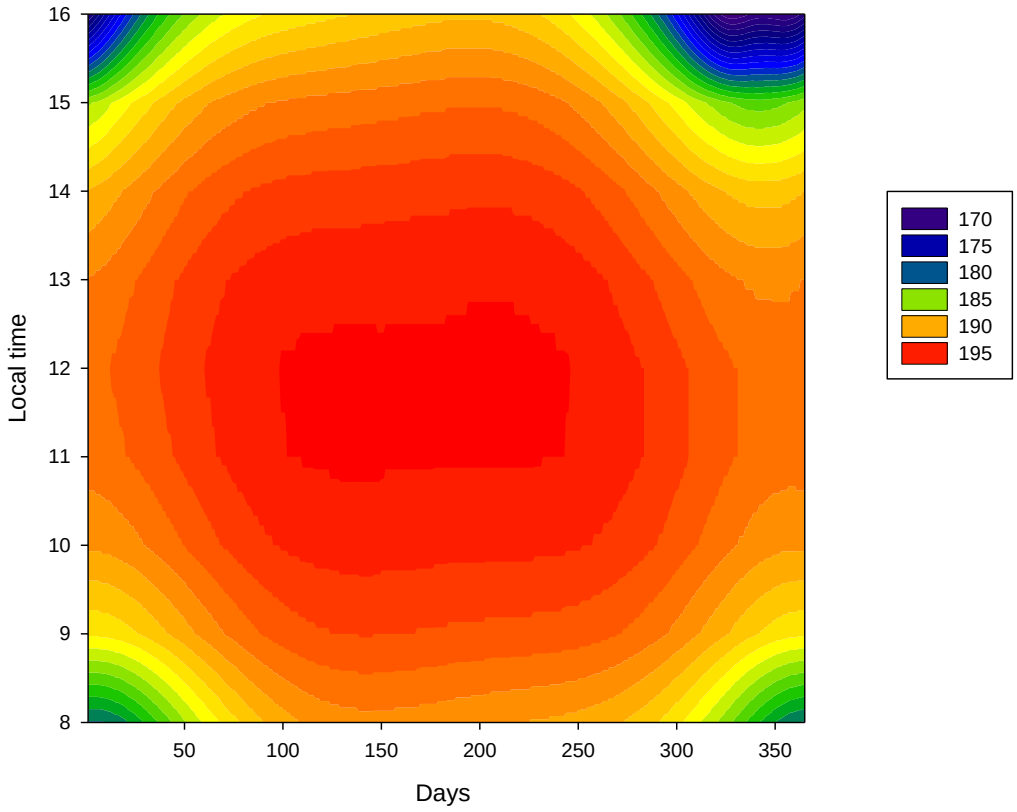

Figure 5.11: Photovoltaic maximum module voltage between 8:00 A.M to 4:00 P.M throughout the year for a clear sky.

The average output decreases during the winter time because of shorter days which results in smaller radiation intensity as depicted by the Figure 5.10. Figure 5.11 shows the Photovoltaic maximum module voltage between 8:00 A.M to 4:00 P.M throughout the year for a clear sky. As stated in explanation of Figure 5.7, increasing the radiation intensity increases the maximum output voltage of the module and vice-versa. The maximum module reaches a value of 186.5V during the summer session. However it drops to 170V at 4:00 P.M during the winter session. Figure 5.13 shows the photovoltaic maximum module current between 8:00 A.M to 4:00 P.M throughout the year for a clear sky. The maximum current output from the module increases from 8:00 A.M till the afternoon and then start to decrease because of decrease in radiation intensity. Its value is maximum during the summer session and minimum during the winter session.

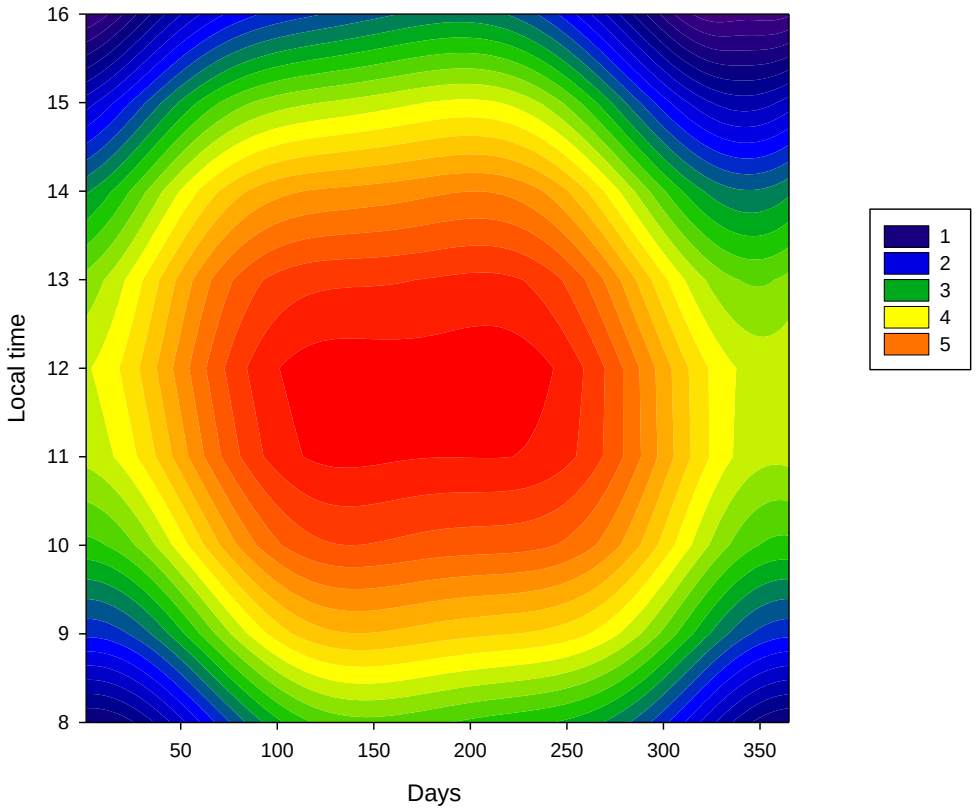

Figure 5.12: Photovoltaic maximum module current between 8:00 A.M to 4:00 P.M throughout the year for a clear sky.

5.3 PVT Thermal Model Results

As the sun light is being concentrated on the PVT module, it increases the energy input on the surface of PVT module. This energy travels through different layers of cell (see Figure 2.1 for details). In order to reduce the temperature of the cell, a fluid flows through between the tedlar and last insulation layer. In present analysis, Therminol-66 is used as a fluid. As Therminol-66 cool down the module, its temperature increases. The increase in temperature is mainly dependent on the radiation intensity and concentration factor. Figure 5.13 shows the effect of radiation intensity and concentration factor on maximum solar cell temperature. Increase in either radiation intensity or the concentration factor increases the cell temperature. Depending up on the flow rate of the cooling fluid (Therminol-66), the temperature of the working reaches up to 700K at a radiation

intensity of 1000 W/m^2 and at concentration factor of 20. Equation 4.60 is used to calculate the cell temperature.

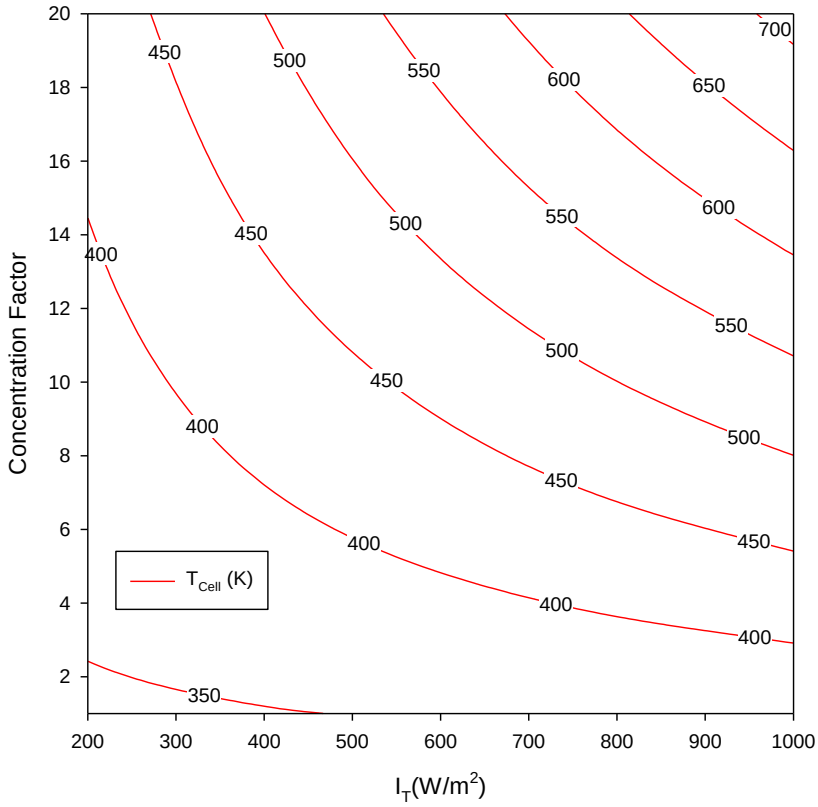

Figure 5.13: Effect of radiation intensity and concentration factor on cell temperature.

Figure 5.14 shows the cooling fluid temperature in dynamic mode (i.e. integrating the PVT thermal model with the radiation intensity model for the city of Toronto between 8:00 A.M to 4:00 P:M for a concentration factor of 15). The temperature of the cell increases from 8:00 A.M till afternoon because of increase in radiation intensity. Increase in the cell temperature ultimately transform into increase in cooling fluid temperature at a given flow rate of the cooling fluid. The temperature of the fluid increases to 550K. However the system will be on optimum value (will be discussed in optimization section). All the energy above the optimum value is stored. The period in which excess energy is stored is referred as charging period. This excess energy is used when the radiation intensity is not enough to heat up the cooling fluid Thermonial-66 to its optimum value. The high temperature Therminol-66 is used to transfer the heat into secondary loop and to

run the organic cycle. After around 1:00 P.M in most of the days in the year, the temperature of the cooling fluid starts to decrease and system run in discharging mode.

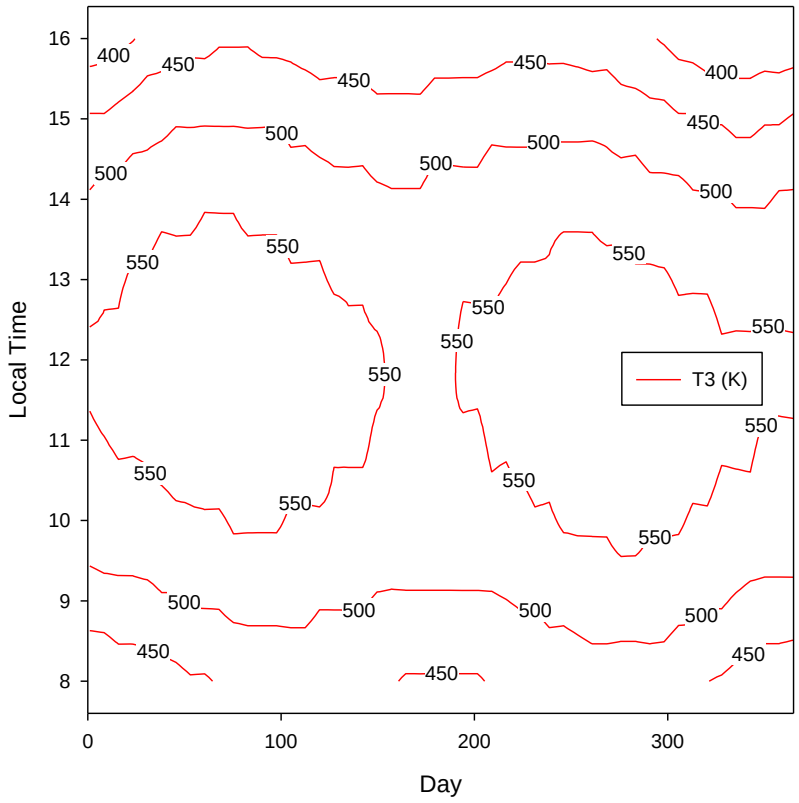

Figure 5.14: Temperature at the exit of PV arrays from 8:00 A.M to 4:00 P.M throughout the year.

5.4 Thermodynamic Efficiency Analysis Results

In this section, the results of thermodynamic modeling are presented. Effect of ambient temperature, pressure and temperature of the secondary loop and pressure of absorption chiller is invest aged on energy, exergy efficiency and network output. The detail thermodynamic model is given in section 4.1.4.

5.4.1 Effect of Ambient Temperature

Ambient temperature effect the performance of the system. Changing ambient temperature changes number of parameters. It changes the radiation intensity because of change in vapour

thickness in the environment, and exergy of the system. Figure 5.15 shows the effect of ambient temperature on the energy efficiency, the exergy efficiency, and the network output of the system. Increase in ambient system reduces the energy and exergy efficiency of the system. The energy efficiency drops from around 48% to 44% and exergy efficiency changes 1% (i.e. from 39% to 38%) when the ambient temperature changes from 260K to 320K. This drop in energy efficiency is because of decrease in required energy for heating purpose and more input energy is required for cooling purposes. The drop in exergy efficiency is because of decrease in available exergy of the system. With increase in ambient temperature, the output work increases from around 166kW to 169.5kW. This increase is because of less energy required for the fluids in primary and secondary to heat-up to their optimum value.

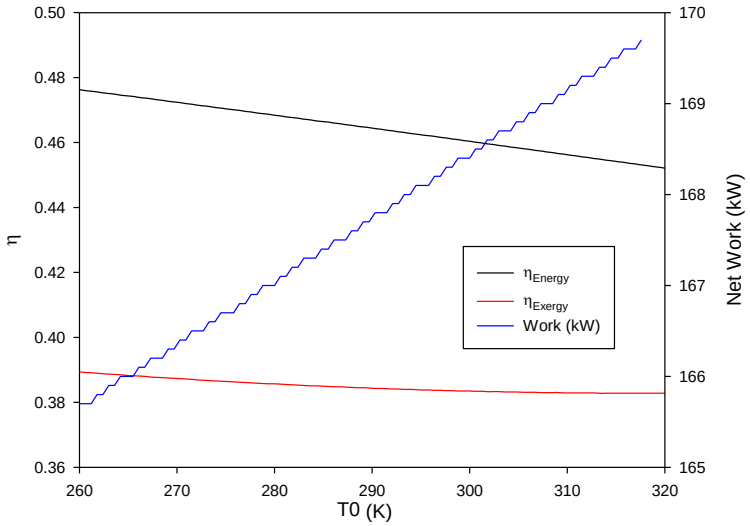

Figure 5.15: Effect of ambient temperature on energy, exergy and network output (kW).

5.4.2 Effect of Pressure and Temperature of Secondary Cycle

The secondary cycle is solely dependent upon heat transfer from the primary cycle. Figures 5.16 and 5.17 show the effect of pressure of organic Rankine cycle on energy and exergy efficiency at different organic Rankine cycle temperatures, respectively. The pressure is varied from 2000 kPa to 5000 kPa and the temperature of the secondary cycle is varied from 510K to 550K. Increasing the temperature decreases the energy efficiency of the system because more input energy is required to heat up the n-octane to 550K. This increases the denominator term in the Eq. 4.128.

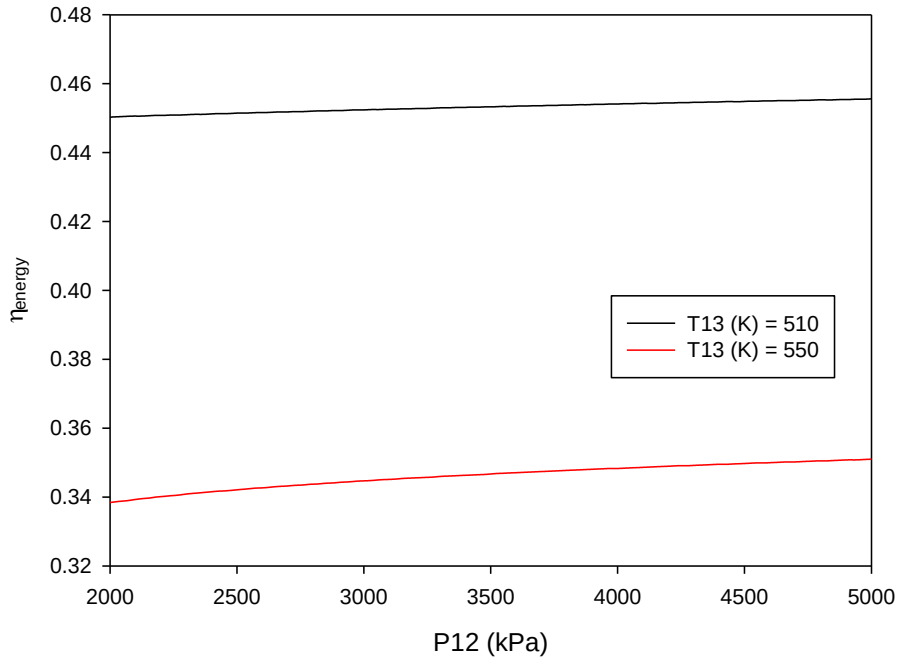

Figure 5.16: Effect of pressure of organic Rankine cycle on energy efficiency at different cycle temperatures

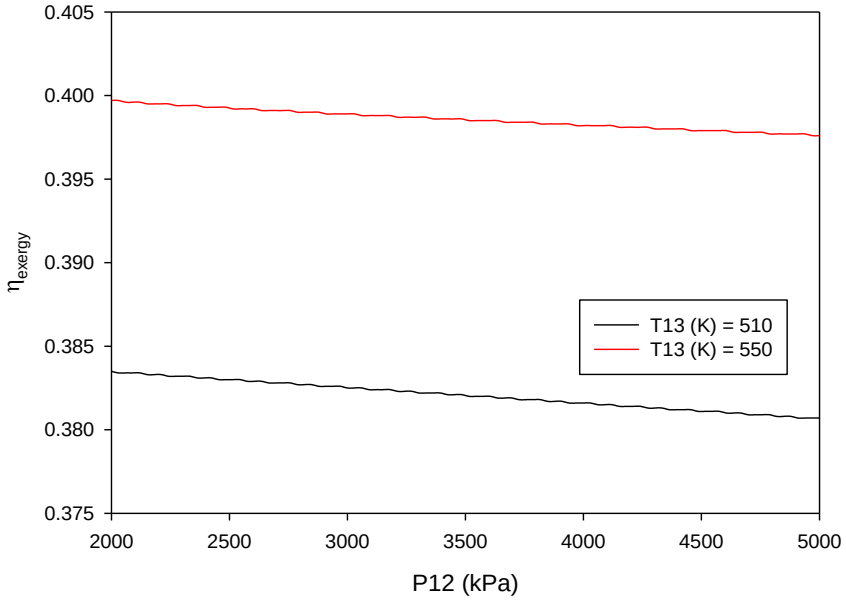

Figure 5.17: Effect of pressure of organic Rankine cycle on exergy efficiency at different organic Rankine cycle temperatures.

With increase in pressure the energy efficiency increases because of slight increase in the enthalpy difference for the heating output. The energy efficiency changes from 45% to 46% at a secondary loop temperature of 510K when the pressure changes from 2000kPa to 5000kPa. Similarly, the energy efficiency changes from 34% to 35% at a secondary loop of temperature of 550K when the pressure changes from 2000kPa to 5000kPa. The exergy efficiency shows quite an opposite trend. Increasing the pressure of the secondary loop decreases the exergy efficiency of the system. This is because of increase in input work to the system as a result of increases in pressure followed by higher exergy losses in the system components which decreases the exergy efficiency of the system. However, the decrease in work output and exergy losses due to increase is very small. Figure 5.18 shows the effect of secondary cycle on network output at different organic Rankine cycle temperatures. The temperature of the secondary loop however has quite significant effect on the output work. The output work decreases from 177kW to 168.5kW at 2000 kPa.

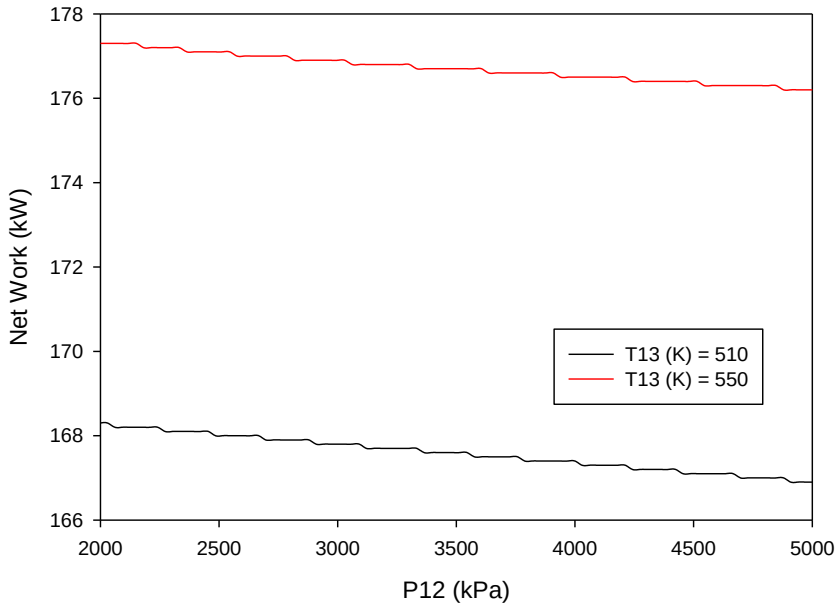

Figure 5.18: Effect of pressure of organic Rankine cycle on network output at different organic Rankine cycle temperatures.

5.4.3 Effect of Pressure of Absorption Chiller

Figure 5.19 shows the effect of pressure of the ammonia water quadruple absorption chiller on energy efficiency, exergy efficiency and network output. Increasing the pressure of pump-3

increases the network input to the system which decreases energy efficiency, exergy efficiency and the network output of the system. The energy efficiency changes from 45% to 41% and the exergy efficiency changes from 38.5% to 33.5%. This is because of change in net work output of the system which decrease linearly with increases in pressure. The work output decreases from 167kW to 147kW.

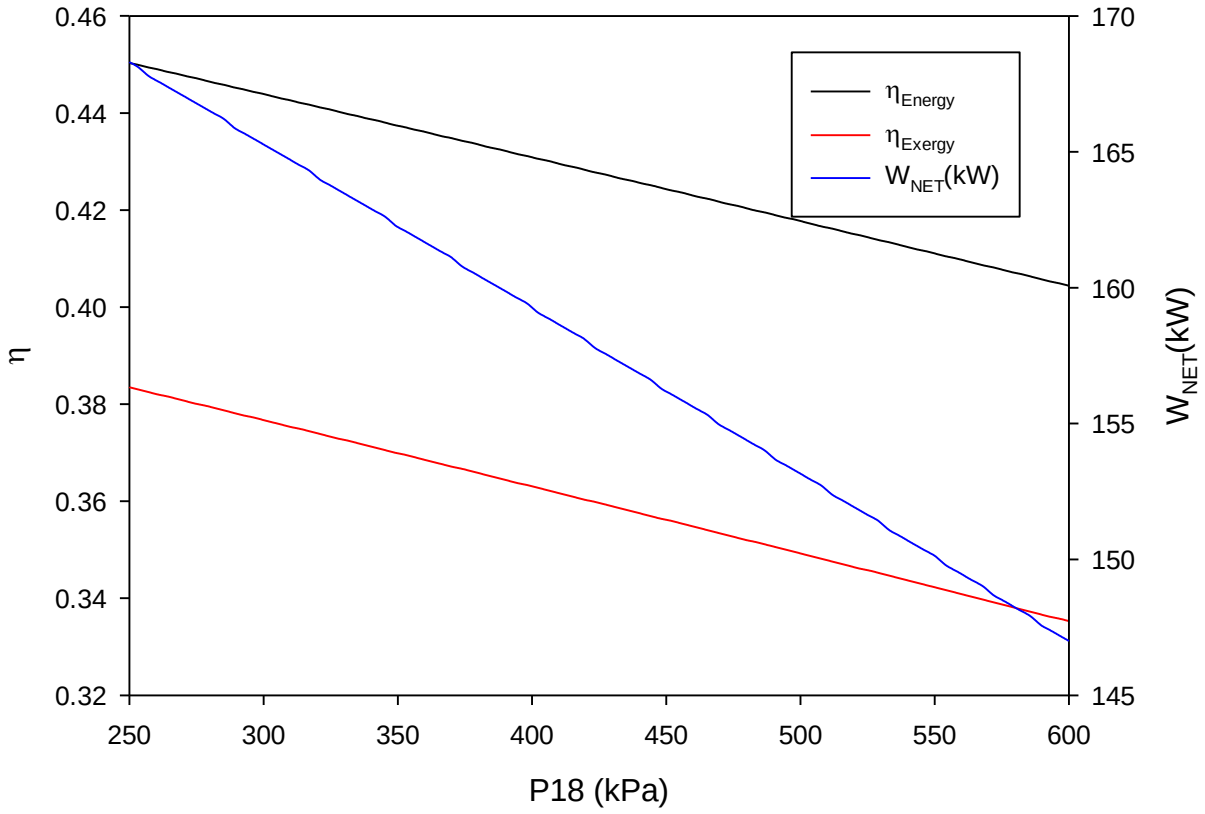

Figure 5.19: Effect of pressure of the ammonia water quadruple absorption chiller on energy efficiency, exergy efficiency and network output.

5.5 Environmental Impact Accessibility Results

In this section, the effect of ambient temperature and secondary loop pressure on different environmental coefficients. The details of these coefficients are given in section 4.1.7.

5.5.1 Effect of Ambient Temperature

As discussed in section 5.4.1, the ambient temperature changes the energy and exergy efficiency of the system because of change in network output and exergy destruction of the system components. This results in change in exergoeconomic factors discussed in Section 4.1.7. Figure 5.20 shows the effect of ambient temperature on exergoenvironmental impact factor, exergo environmental impact improvement and exergetic sustainability index. The exergoenvironmental impact factor increases with increase in ambient temperature. This is because of increase in exergy destruction with increase in ambient temperature. Its value changes from 0.611 to 0.617. The exergoenvironmental impact improvement factor and exergetic sustainability index decreases with increase in ambient temperature. This means that the system is more environmentally benign at lower ambient temperatures.

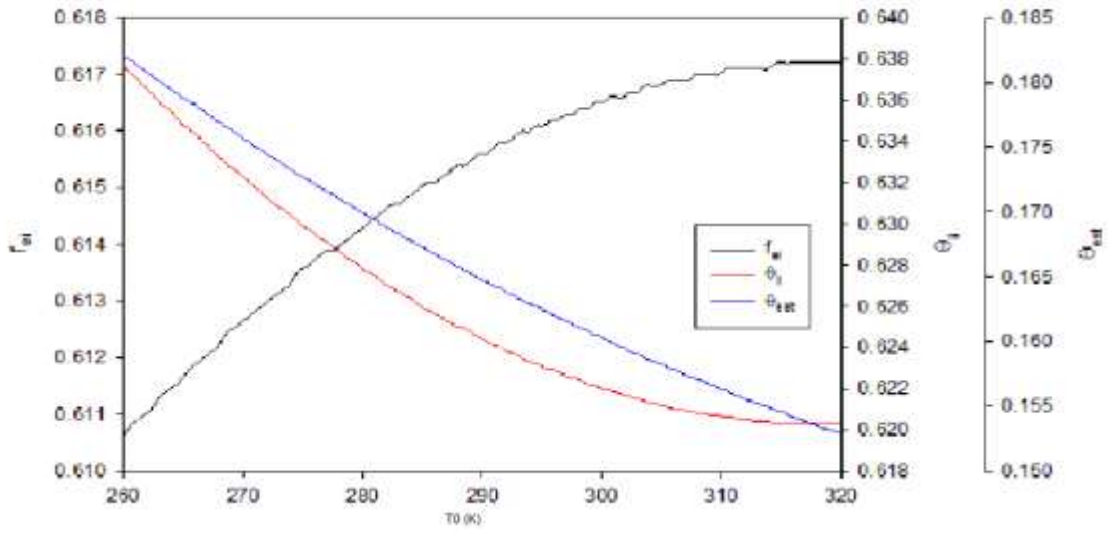

Figure 5.20: Effect of ambient temperature on exergoenvironmental impact factor, exergo environmental impact improvement and exergetic sustainability index.

5.5.2 Effect of Secondary Loop Pressure

Figure 5.21 shows the effect of pressure of the ammonia water quadruple absorption chiller on exergoenvironmental impact factor, exergoenvironmental impact improvement and exergetic sustainability index. Because increasing the pressure reduces the exergy efficiency of the system (see Figure 5.17) hence increases the environmental impact.

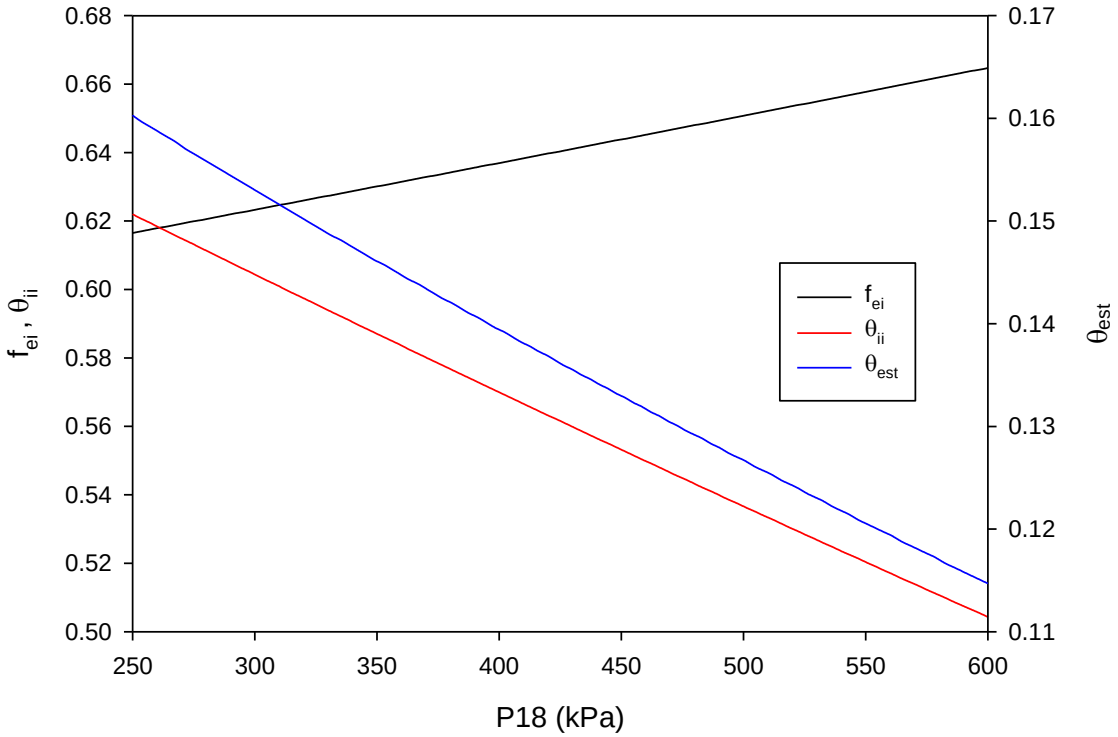

Figure 5.21: Effect of pressure of the ammonia water quadruple absorption chiller on exergo environmental impact factor, exergoenvironmental impact improvement and exergetic sustainability index.

5.6 Exergoeconomic and Enviroeconomics Results

In this section, the results of exergoeconomic and enviroeconomics models are presented. Effect of ambient temperature, pressure and temperature of the secondary loop and pressure of absorption chiller is investigated on cost coefficient of work, chiller and hydrogen production. The detail thermodynamic model is given in section 4.1.8.

5.6.1 Effect of Ambient Temperature

The exergoeconomic and enviroeconomics analysis are carried in order to find the effect of different processing parameters on cost of work, cost of hydrogen and environmental cost. Figure 5.23 shows the effect of ambient temperature on enviroeconomics cost parameter, cost coefficient of hydrogen and cost coefficient of network output. Increase in ambient temperature results in decrease in enviroeconomics cost parameter. This is because of increase in network output of the

system. The ambient temperature is varied from 260K to 320K. The resulting enviro economic cost parameter decreases from $17,850/annum to $16,900/annum. However, because of decrease in exergy efficiency of the system results in increase in the cost coefficients of the hydrogen production and cost coefficient of network output. The cost coefficient of hydrogen increases from 7.5 $/kWh to 11.7 $/kWh when the ambient temperature changes from 260K to 320K. The cost coefficient of work changes increases from 10.5 ₡/kWh to 13.2 ₡ /kWh with the same variation of ambient temperature from 260K to 320K. Economically, the best situation is at lower ambient temperature.

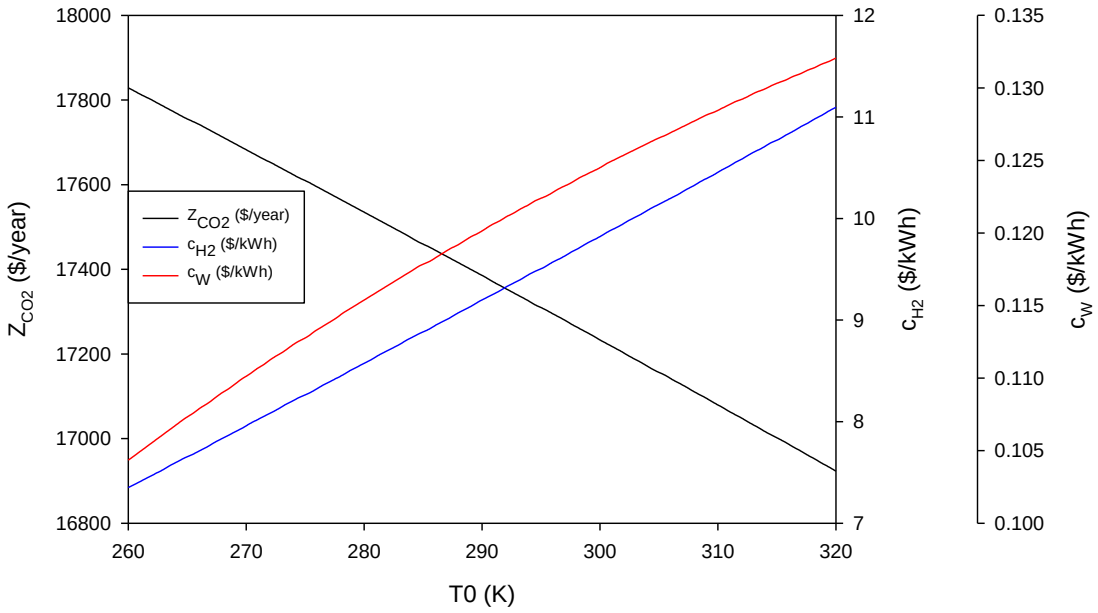

Figure 5.22: Effect of ambient temperature on enviroeconomics parameter, cost coefficient of hydrogen and cost coefficient of network output.

5.6.2 Effect of Pressure and Temperature of Secondary Cycle

Figure 5.24 shows the effect of pressure of organic Rankine cycle on enviro economic parameter at different organic Rankine cycle temperatures. As with increase in temperature, the net useful output work increases which results in decrease in enviro-economic coefficient. The increase in organic Rankine cycle pressure results in slight increase in enviro-cost coefficient. This is because of slight increase in network input with increase in pressure. At 2000 kPa, the cost coefficient is around 12800/annum at 550K and 16900$/annum at 510K. As stated earlier, the increase in

pressure results in slight decrease in network output, so at 5000kPa, the cost coefficient of the enviro-economic parameter also increases slightly.

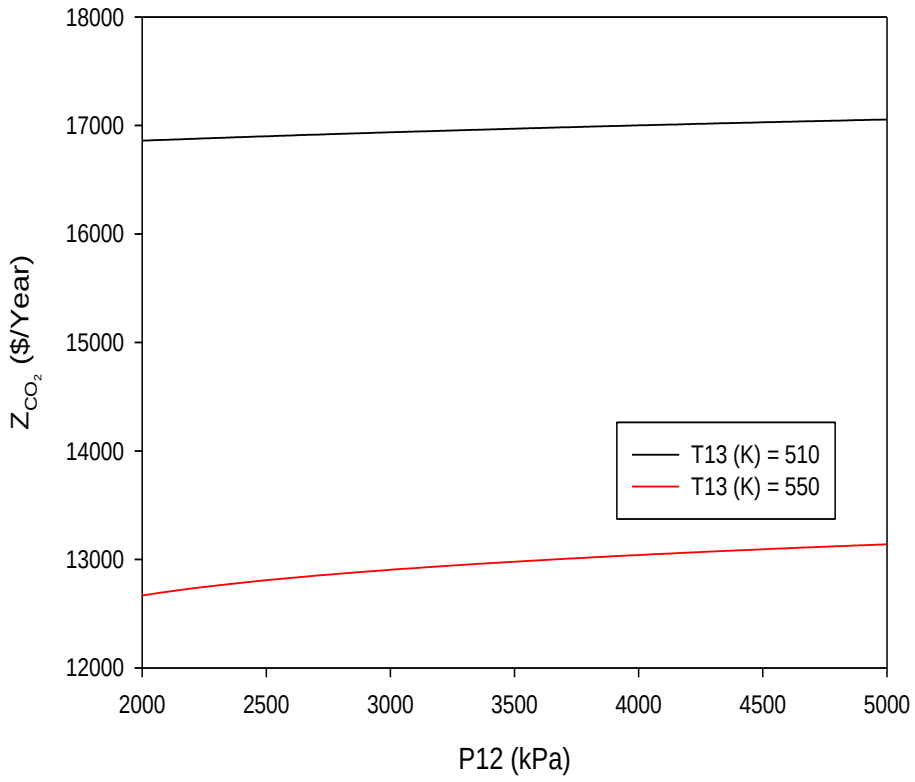

Figure 5.23: Effect of pressure of organic Rankine cycle on enviro economic parameter at different organic Rankine cycle temperatures.

Figure 5.24 shows the effect of pressure of organic Rankine cycle on network cost coefficient at different organic Rankine cycle temperatures. Increase in temperature results in increase in cost of the output work because of increase in exergy input to the system. In order to increase the temperature either radiation intensity increases or the concentration factor increases. Figure 5.24 is drawn at a radiation intensity of 1000W/m2 which means in order to increase the temperature, the concentration factor needs to be increased (Eq. 4.122) which results in increase in cost of the network output.

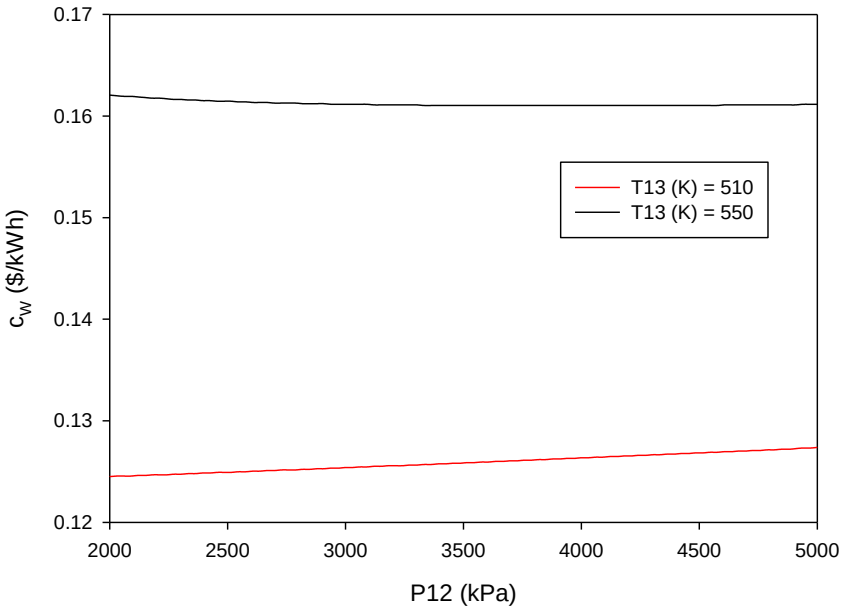

Figure 5.24: Effect of pressure of organic Rankine cycle on network cost coefficient at different organic Rankine cycle temperatures.

The pressure of the organic Rankine cycle does not have significant effect of the cost coefficient of the work. At 2000 kPa, the cost coefficient of work is 0.0027$/kW.min at 550K and 0.0021$/kW.min at 510k. The cost coefficient of hydrogen follows the same trend as of cost coefficient of work because it is assumed in the entire analysis that 10% of the total electrical work is used to produce hydrogen.

5.6.3 Effect of Pressure of Absorption Chiller

Figure 5.25 shows the effect of pressure of the ammonia water quadruple absorption chiller on enviro economic parameter and cost coefficient of cold water. As increase in pressure of the absorption chiller cycle, increases the net input work input and decreases the efficiency and net available energy which results in decrease in enviro economic cost parameter. The absorption chiller pressure is varied from 250 kPa to 600 kPa. The cost parameter decrease from 16,850$/annum to 15,200$/annum. On the other hand, cost coefficient of chiller output increases with increase in pressure of absorption chiller cycle. This increase is because of increase in net work input. At 250 kPa, the cost coefficient of the chiller is 0.0029$/kW.min and it increases to 0.0034$/kW.min when the pressure increases to 600 kPa.

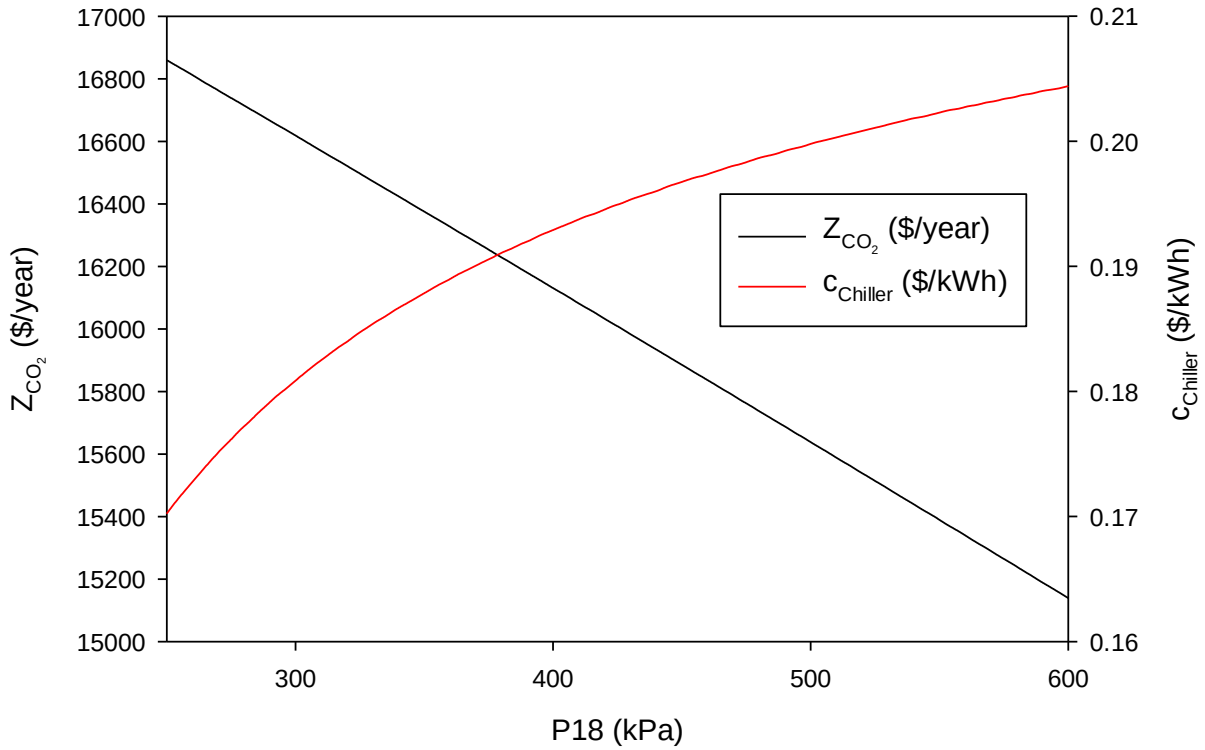

Figure 5.25: Effect of pressure of the ammonia water quadruple absorption chiller on enviro economic parameter and cost coefficient of cold water.

5.7 Optimization Results

As discussed in Section 4.1.8, based on the parametric study, five parameters namely pressure in primary loop, pressure and temperature of organic Rankine cycle, pressure and temperature of ammonia water chiller system are chosen for optimization. There are three output parameters (also called objective functions in optimization study) namely exergy efficiencies, cost of electricity, enviro economic parameter and on different exergoenvironmental factors. A genetic algorithm NSGA-II algorithm is used for optimization. The population size chosen for optimization is 1400 with 1500 iterations. Figure 5.26 shows the results of all evaluations during 1500 generations using genetic algorithm. Exergy efficiency on x-axis, electricity cost coefficient ($/kWh) on y-axis and exergoenvironmental impact coefficient on z-axis. Three different points were marked as point of interest as shown in Table 5.2.

Table 5.2: Optimized points of interest

Point	η_{exe} (%)	c_W (¢/kWh)	C_{ei}
A	38.14	13.4	2.619
B	40.04	16.3	2.505
C	34.64	14.1	2.884

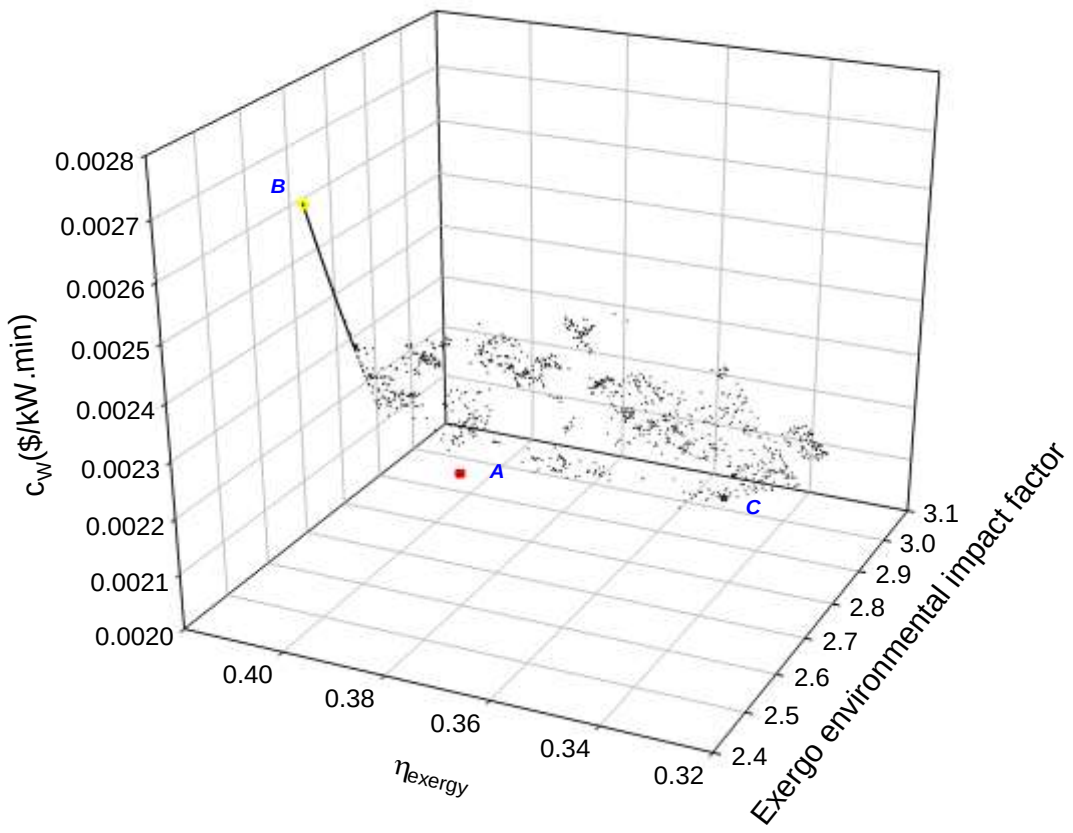

Figure 5.26: Results of all evaluations during 1400 generations using genetic algorithm. Exergy efficiency on x-axis, Electricity cost coefficient ($/kW.min) on y-axis and exergoenvironmental impact coefficient on z-axis.

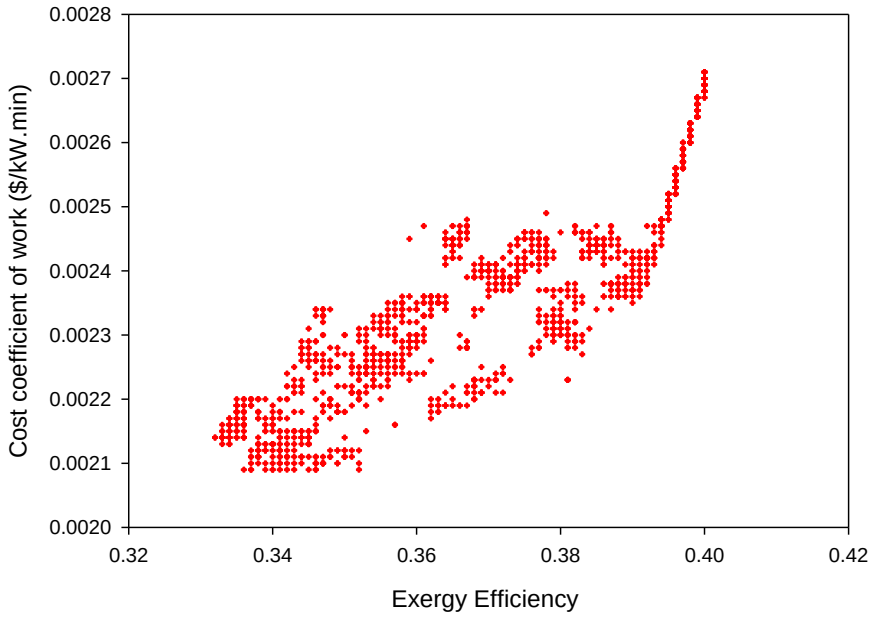

Figure 5.27: Pareto frontier solutions for exergy efficiency and cost coefficient of work

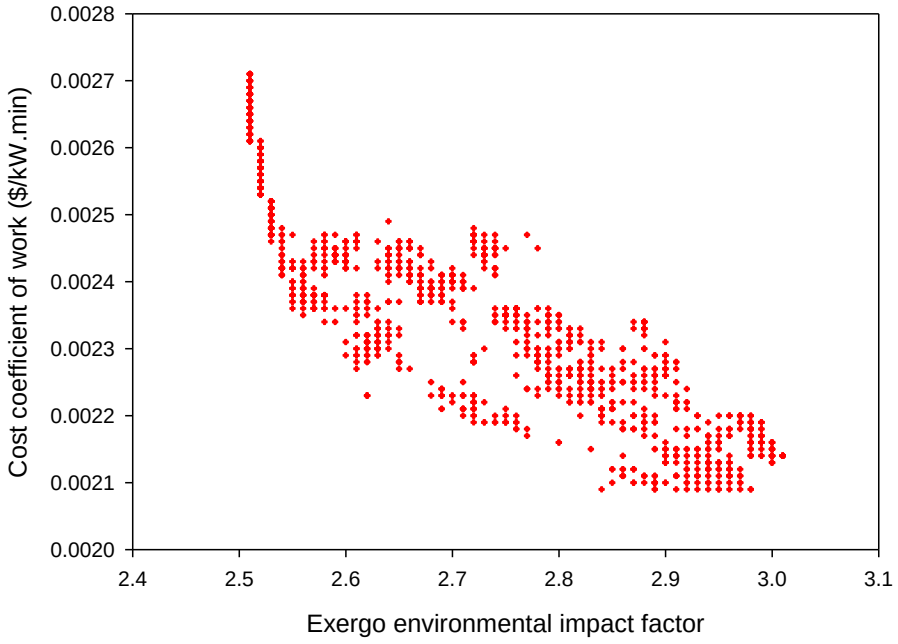

Figure 5.28: Pareto frontier solutions for exergoenvironmental impact factor and cost coefficient of work

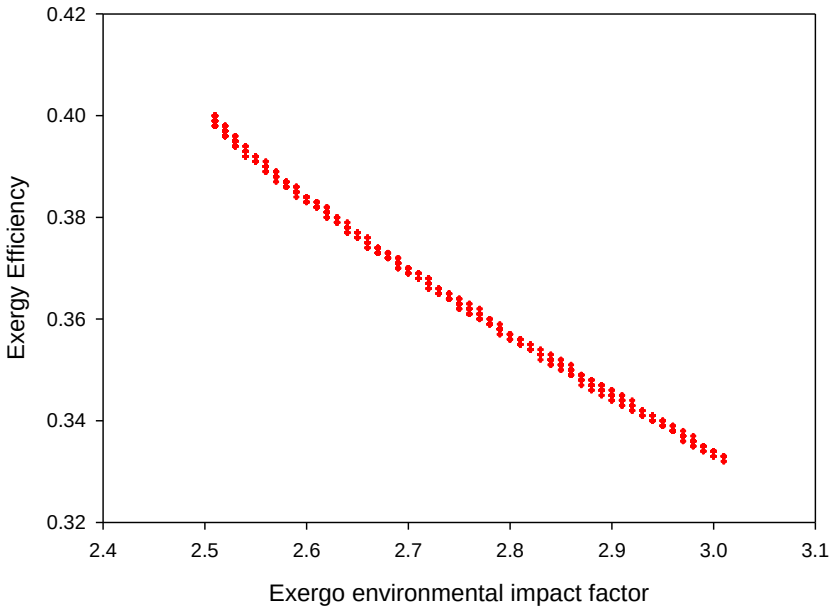

Figure 5.29: Pareto frontier solutions for exergoenvironmental impact factor and exergy efficiency

Figures 5.27-5.29 show the Pareto frontier solutions for exergo environmental impact factor, exergy efficiency and cost coefficient of work. As stated earlier, the objective is to choose a point where cost is minimum, efficiency is maximum and exergo environmental impact coefficient is minimum. At point A, cost is minimum but the exergy efficiency is not at its maximum value. At point B, the exergy efficiency is maximum however, the cost is maximum. At point C, the efficiency is minimum and the cost is also close to its minimum. Table 5.3 shows the thermodynamic characteristics of three different points on the Pareto frontier. In this study, I chose the point A as the optimized point. The efficiency at point A is reasonably high and cost is minimum with small value of environmental impact coefficient.

Table 5.3: Thermodynamic characteristics of three different points on the Pareto frontier

Point	P2 (kPa)	P12 (kPa)	T13 (K)	P18 (kPa)	T40 (K)
A	159.6	2000	518.8	298.3	286.1
B	150	2000	550	250	288
C	180.9	2263.7	510	523.1	282.5

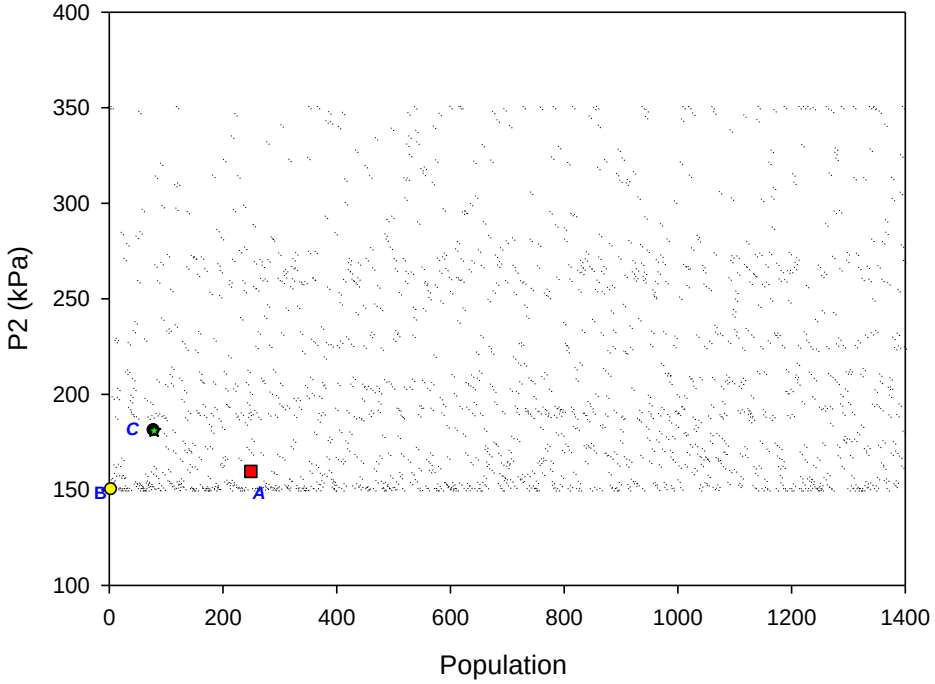

Figure 5.30: Scattered distribution of decision variables with population in Pareto frontier for pressure in primary loop

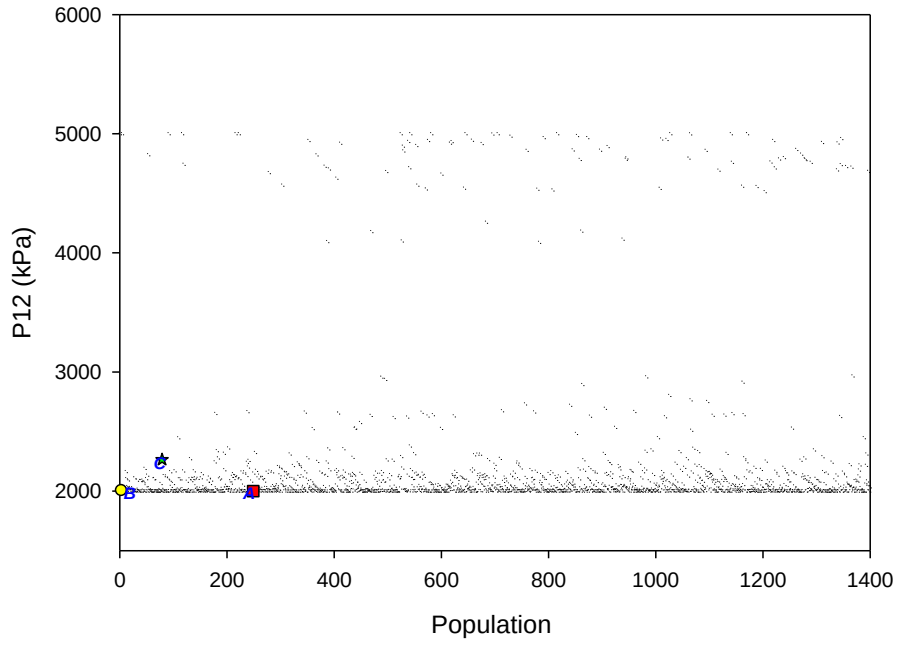

Figure 5.31: Scattered distribution of decision variables with population in Pareto frontier for pressure in secondary loop

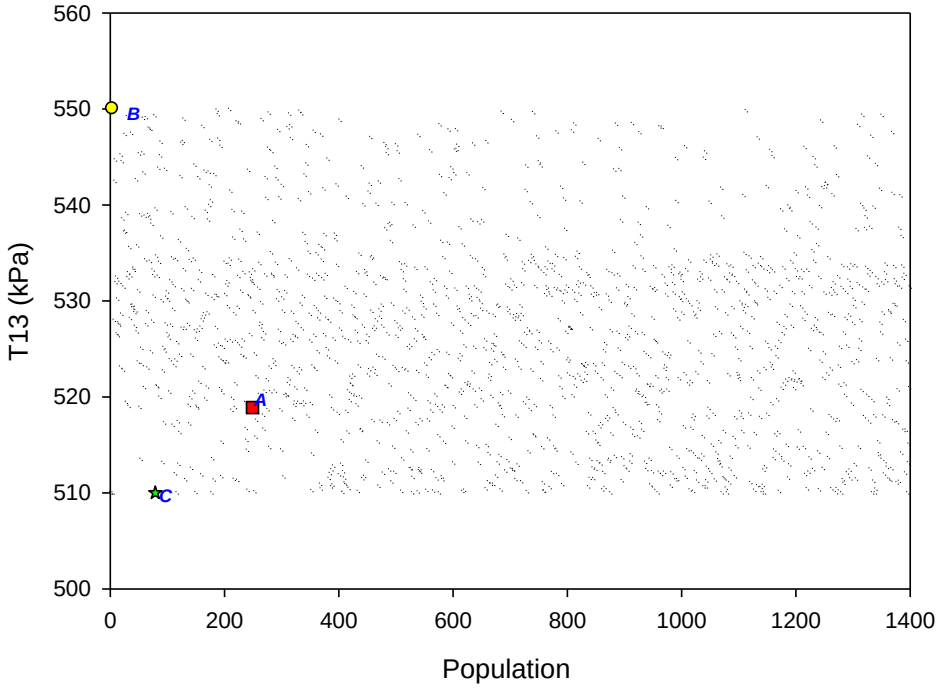

Figure 5.32: Scattered distribution of decision variables with population in Pareto frontier for temperature in secondary loop

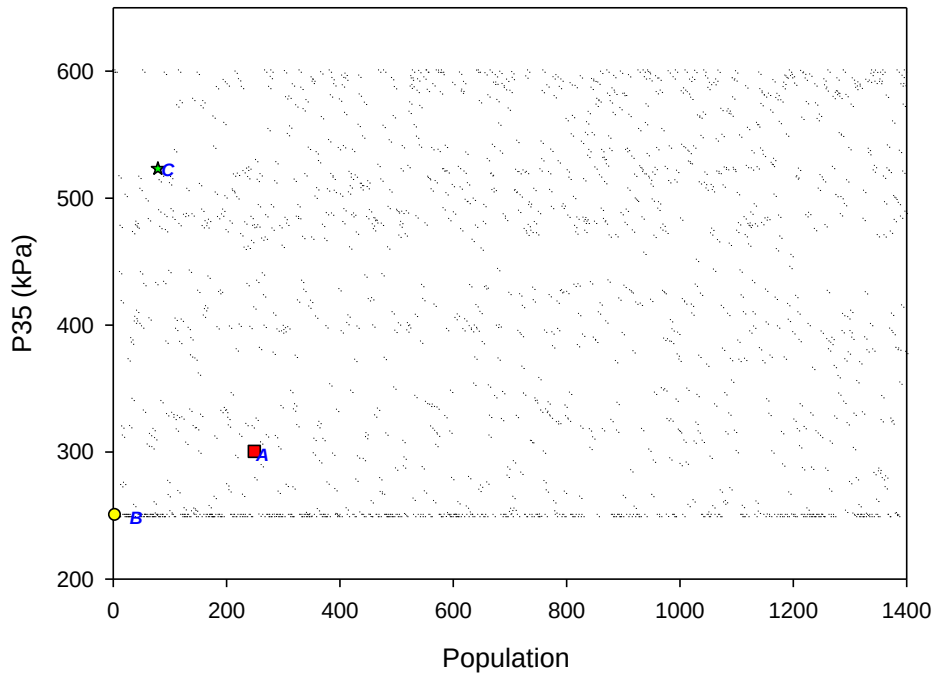

Figure 5.33: Scattered distribution of decision variables with population in Pareto frontier for pressure in absorption chiller

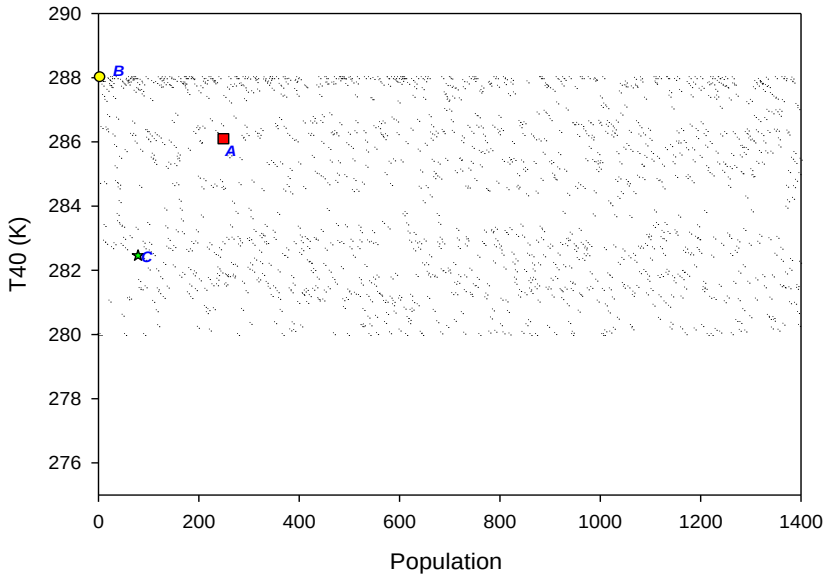

Figure 5.34: Scattered distribution of decision variables with population in Pareto frontier for temperature in absorption chiller.

The optimized pressure in primary loop is 159.6 kPa, the pressure and temperature of organic Rankine cycle is 2000 kPa and 518.8K respectively, the pressure and temperature of ammonia water chiller system is 298.3 kPa and 286.1 K respectively. Figure 5.30 to Figure 5.34 show the scattered distribution of decision variables with population in Pareto frontier for pressure in primary loop, pressure in secondary loop, temperature in secondary loop, pressure in absorption chiller and temperature in absorption chiller.

5.7.1 Sensitivity Analysis Results

In order to have a better understanding of our multi-objective optimization, a comprehensive sensitivity analysis is performed. The five input parameters are varied up to 3% of their optimum value subject to the condition presented in Eq.s 4.143 to 4.160. This is to investigate the effect of variation of input parameters on the objective function. Six different cases are studied in present study.

Case-1 Results

Figure 5.35 shows the effect of variation of primary loop pressure on all three objective function. The nominal value is the optimized value using NSGA-II (same as Figure 5.27).

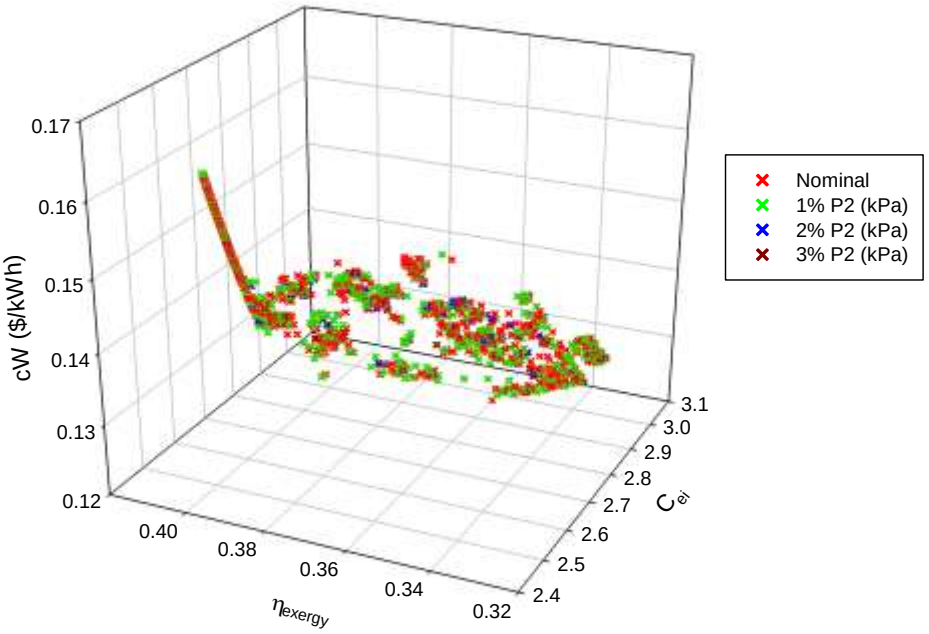

Figure 5.35 Effect of primary loop pressure on all three objective functions

At 1% change in pressure (of point A from Table 5.3), the maximum in change in exergy efficiency is 0.015%, the maximum change in cost coefficient is 0.023% and the maximum change in environmental impact coefficient is 0.02% from their nominal optimized value. When said "maximum change", it means out of all 1400 nominal solutions (can also be termed as Pareto frontier solutions), the solution at which difference between the nominal value of the objective function and the value at varied parameter is maximum. When the pressure of the primary loop is varied to 2% of its nominal optimized value, the maximum exergy efficiency changes 0.017%, the maximum change in cost coefficient is 0.025% and the change in environmental impact coefficient is 0.021% from their nominal optimized value. Increasing the pressure further increase the difference between nominal optimized value and value at a new pressure of the primary loop. As stated earlier, in present analysis, the maximum studied variation is 3%. So at 3% variation in primary loop, the maximum exergy efficiency changes 0.018%, the change in cost coefficient is 0.0254% and the change in environmental impact coefficient is 0.021% from their nominal optimized value. This basically concludes that variation in primary loop pressure do not have significant effect on the objective functions.

Case-2 Results

Figure 5.36 shows the effect of variation of secondary loop pressure on all three objective function.

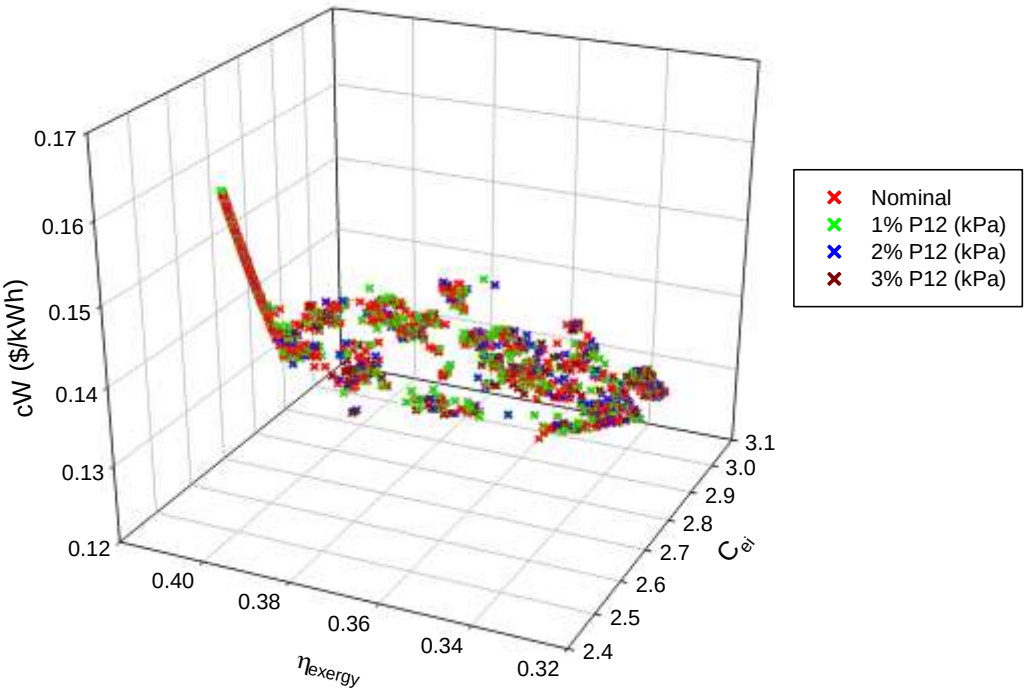

Figure 5.36: Effect of secondary loop pressure on all three objective functions

At 1% change in pressure value (of point A from Table 5.3) results in maximum change in exergy efficiency by 0.038%, the maximum change in cost coefficient is 0.084% and the maximum change in environmental impact coefficient is 0.037% from their nominal optimized value. When the pressure of the secondary loop is varied to 2% of its nominal optimized value, the exergy efficiency changes 0.06%, the maximum change in cost coefficient is 0.12 % and the maximum change in environmental impact coefficient is 0.054% from their nominal optimized value. At 3% variation in primary loop, the maximum exergy efficiency changes 0.074%, the maximum change in cost coefficient is 0.15% and the change in environmental impact coefficient is 0.07% from their nominal optimized value. This suggest that variation in secondary loop pressure do not have significant effect on the objective functions.

Case-3 Results

Figure 5.37 shows the effect of variation of secondary loop temperature on all three objective function. The maximum variation of the value of point A is at 3% of the nominal optimized value.

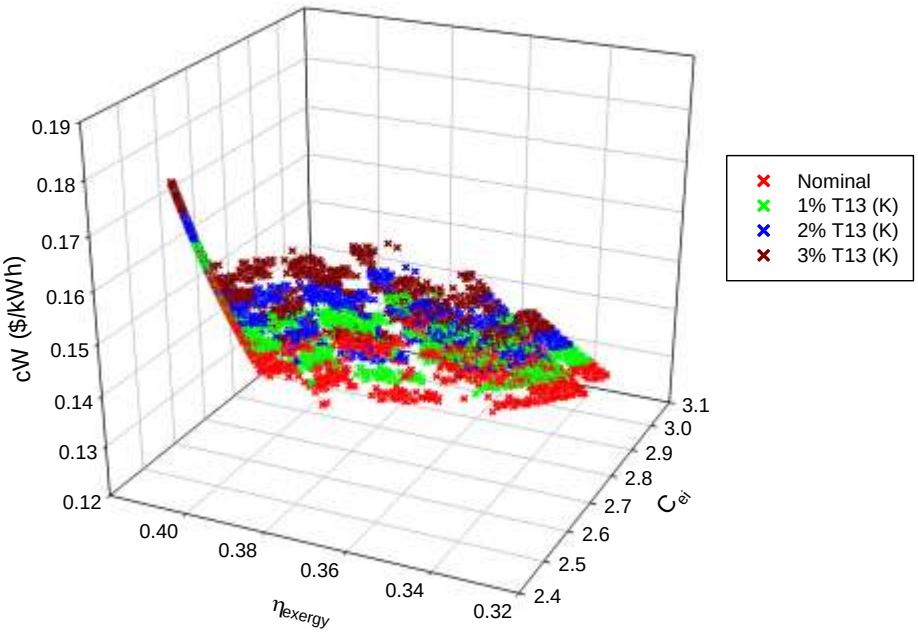

Figure 5.37: Effect of secondary loop temperature on all three objective functions

At 3% variation in secondary loop temperature, the maximum exergy efficiency changes by 3.01 %, the maximum change in cost coefficient is 11.31 % and the maximum change in environmental impact coefficient is 3.14 % from their nominal optimized value. This basically suggests that the objective functions are sensitive to the variation in secondary loop temperature.

Case-4 Results

Figure 5.38 the effect of variation of absorption chiller pressure and temperature on all three objective functions.

Case-5 Results

Figure 5.39 show the effect of variation of absorption chiller pressure and temperature on all three objective functions.

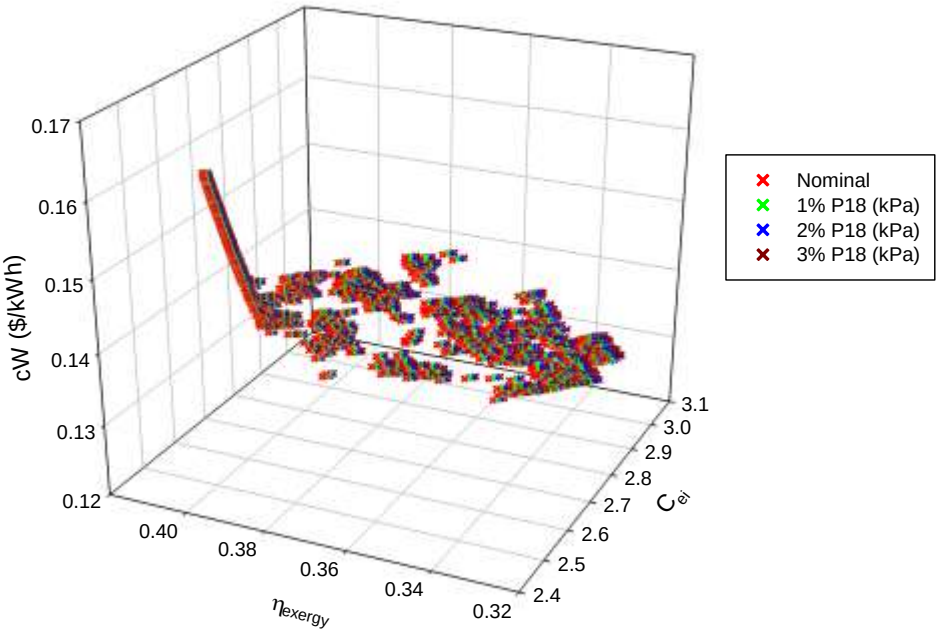

Figure 5.38: Effect of absorption chiller pressure on all three objective functions

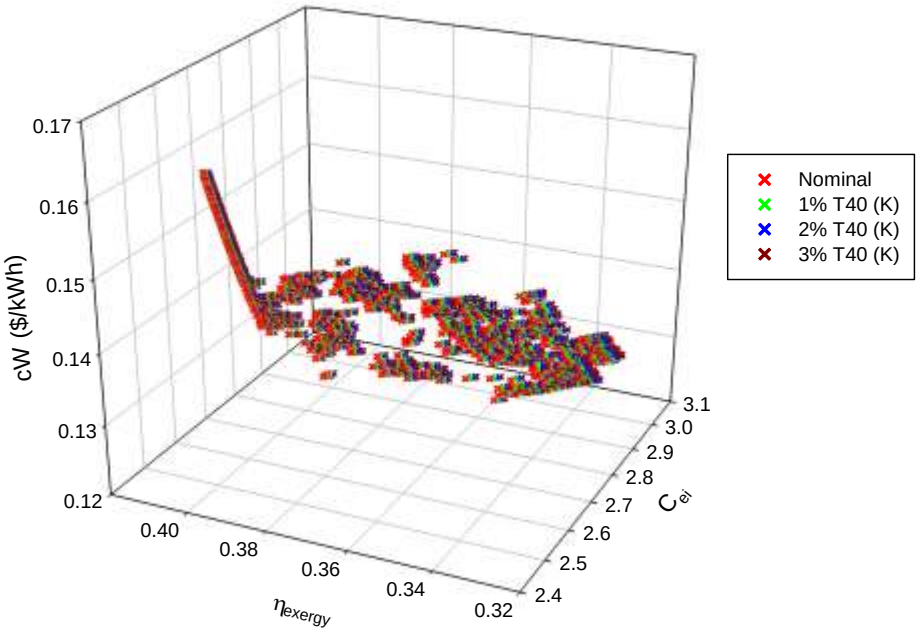

Figure 5.39: Effect of absorption chiller temperature on all three objective functions

At 3% change in value of the pressure and temperature of the absorption chiller, the maximum change in exergy efficiency, work cost coefficient and environmental impact coefficient are less than 0.05%. This mean that the variation in pressure and temperature.

Case-6 Results

Figure 5.40 shows the effect of variation of all five decision variables on all three objective functions. All 5 decision variables (P_2, P_{12}, T_{13}, P_{18}, $T_{40)}$ were varied up to 3% of their value simultaneously. At 3% change in values of all the decision variables, the maximum change in exergy efficiency is 1.5%, work cost coefficient changes by 7.6% and environmental impact coefficient are less than 1.7%. Compared to other decision variables, the secondary loop temperature variation has the most significant impact on all objective functions. This concludes the sensitivity analysis.

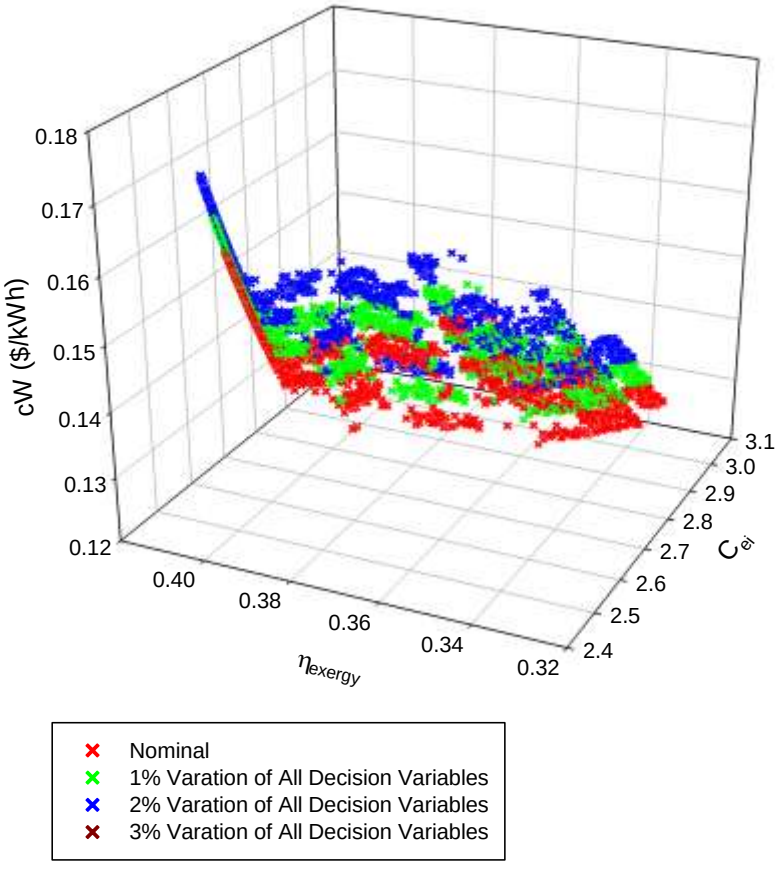

Figure 5.40: Effect of variation of all five decision variables on all three objective functions.

In all the above discussed cases the overall variation is much smaller then minimum acceptable limit for point A. Thus point “A” (in table 5.2 and 5.3) is the most optimum point and variation of 3% in decision variable range of PF solution of A do not have significant effect on the main objective functions as well. Hence “A” is also less sensitive.

Based on the parametric study presented from section 5.1 to section 5.6, the optimized solution is predicted before the sensitivity analysis (i.e. Point A as an optimum point). Sensitivity analysis confirms the predication and confirm Point A as the robust solution with least sensitivity compared to other two selected points. In the cases where the effect of decision variables are very strong on the output, the final decision should be made after sensitivity analysis.

Chapter 6: Conclusions and Recommendations

This chapter consists of two sections, namely conclusions to present the main findings of this study and recommendations to make some recommendations for future studies.

6.1 Conclusions

A multigeneration renewable energy based system is designed with four loops. The primary loop consist of series of GaAs photovoltaics arrays with concentrated solar irradiation and therminol – 66 as a working fluid, the secondary loop which is an organic Rankine cycle with n-octane, the ammonia water absorption chiller for providing cold water as an output and finally PEM electrolyzer for hydrogen production.

- A number of different models are developed to analyze this system which include Radiation Model, I-V Model of the PV array, PVT Thermal Model, Thermodynamic Model, Exergoeconomic Model, Efficiency Analysis, Exergoenvironmental Analysis and Enviro Economics Analysis.
- Five parameters namely pressure in primary loop, pressure and temperature of organic Rankine cycle, pressure and temperature of ammonia water chiller system have been varied in order to investigate their effect on energy and exergy efficiencies, cost of electricity, enviro economic parameter and on different exergoenvironmental factors.
- Concentrated light reduces the electrical efficiency of the PV panels because of increased cell temperature which is compensated by the electricity produced by the organic Rankine cycle with other useful commodities.
- Concentrated light also decreases open circuit cell voltage and increases close loop current of the PV cells.
- The change in ambient conditions do not have significant effect on the performance of the system. The change in energy and exergy efficiency is very small which results in negligible change in cost coefficient for the work and evniroeconomic parameter.
- Change in organic Rankine cycle temperature significantly affect the energy and exergy efficiency and consequently on cost coefficients. Increasing the pressure increases the energy efficiency of the system but decreases the exergy efficiency. Increasing the temperature increases the net workout and exergy efficiency. Net cost of electrical work

- Pressure of the absorption chiller also have significant effect on 1st and 2nd law efficiencies. The efficiency decreases with increase in pressure of the ammonia water in chiller. The network output also decreases and exergoenvironmental impact factor increases. It also increases the cost of electricity production and cost required to produce cold water.
- The system is optimized using NSGA-II method and results shows that an exergy efficiency of 38.14%, cost of electricity of 13.4 cents/kWh and exergoenvironmental impact coefficient of 2.62 can be achieved at primary loop pressure of 160 kPa, at a pressure and temperature of 2000 kPa and 518.8 K for organic Rankine cycle and at pressure and temperature of 298.3 kPa and 286.1 K for quadruple ammonia water absorption chiller.
- For sensitivity analysis five decision variables are varied. Results showed that the objective functions are highly sensitive to the secondary loop temperature. The change in rest of the four variables does not have any significant effect on the objective function.

6.2 Recommendations

Sustainable energy systems for compound/industrial applications are investigated in this thesis study and the analysis results presented here provide engineers and designers across the globe with potential solutions to reduce environmental impact of residential buildings for various locations and climates by utilizing regionally available renewable resources. For future research, it is recommended to

- Reduced-scale experimental units of the investigated systems should be built and monitored in different locations to provide practical results for varying climates and renewable resource availability, as well as to identify areas for system improvement based on real-world conditions.
- Structurally integrated photovoltaic systems i.e. rooftop arrays, windows, Installations should be studied to increase the efficiencies of the developed systems.
- It is recommended to analyze the same system by using parabolic collectors and do performance comparison with heliostat collectors.
- Geothermal, tidal and other renewable energy based hydrogen production methods should also be studied by using life cycle assessment methodology.

Reference

1. International Energy Agency 2013.
2. C. A. Grimes , O. K. Varghese , S. Ranjan , Light, Water, Hydrogen: The Solar Generation of Hydrogen by Water Photoelectrolysis, 2007, ISBN 978-0-387-68238-9.
3. S. Pachauri, D. Spreng, Measuring and monitoring energy poverty, Energy Policy, Volume 39, December 2011, Pages 7497-7504.
4. C. J. Campbell, The Coming Oil Crisis. Multi-Science Publishing Company & Petro-consultants S.A., Essex, United Kingdom, 1997.
5. D. Rahm, US public policy and emerging technologies: The case of solar energy, Energy Policy, Volume 21, 1993, Pages 374-384.
6. S. Arrhenius, On the influence of carbonic acid in the air upon the temperature of the ground. Philosophical Magazine Volume 41, 1986, Pages 237-276.
7. M. I. Hoffert, K. Caldeira, G. Benford, D. R. Criswell, C .Green, H. Herzog, A. K. Jain, H. S. Kheshgi, K. S. Lackner, J. S. Lewis, H. D. Lightfoot, W. Manheimer, J. C. Mankins, M. E. Mauel, L. J. Perkins, M. E. Schlesinger, V. T, T.M. L Wigley , Advanced technology paths to global climate stability: Energy for a greenhouse planet. Science Volume 298, 2002, Pages: 981.987.
8. M. Jefferson, Sustainable energy development: performance and prospects. Renewable energy Volume 31, Issue 5, April 2006, Pages 571–582.
9. M. Bailey, A. Ö. Arnas, R. Potter, J. W. Samples, The 20 year evolution of an energy conversion course at the United States Military Academy, Energy Conversion and Management, Volume 45, 2004, Pages 495-509.
10. F. McGowan, The single energy market and energy policy: conflicting agendas? Energy Policy, Volume 17, 1989, Pages 547-553.
11. M. Lazzarini, P. Reddy Marpu, H. Ghedira, Temperature-land cover interactions: The inversion of urban heat island phenomenon in desert city areas, Remote Sensing of Environment, Volume 130, 2013, Pages 136-152.
12. I. Dincer, M. Rosen, "Exergy: Energy, Environment and sustainable Development" Elsevier, First edition, 2007, ISBN-13: 978-0080445298.
13. W. Hermann, Quantifying global exergy resources, Energy, Vol. 31, 2006, Pages.1685–1702.
14. T. Ganapathy, N. Alagumurthi, R. Gakkharand, K. Murugesan, Exergy Analysis of Operating Lignite Fired Thermal Power Plant, Journal of Engineering Science and Technology Review 2, Vol. 1, 2009, Pages. 123-130.
15. F. Orhan., I. Dincer. M. Rosen, Exergoeconomic analysis of a thermo-dynamical copper-chlorine cycle for hydrogen production production using specific exergy cost (SPECO) method, Thermochimica Acta, Vol. 497, 2010, Pages. 60-66.
16. F. Orhan., I. Dincer. M. Rosen, An exergy–cost-energy-mass analysis of a hybrid copper-chlorine thermochemical cycle for hydrogen production, International Journal of Hydrogen Energy, Vol. 35, 2010, Issue 10, Pages 4831-4838.
17. M. Rosen, I. Dincer, M. Kanoglu, "Role of exergy in increasing efficiency and sustainability and reducing environmental impact", Energy Policy, Vol. 36, 2008, Issue 1, Pages 128-137.
18. I. Dincer. M. Hussain, M. Al-Zaharnah, Energy and exergy use in public and private sector of Saudi Arabia, Energy Policy, Vol. 32, 2004, Issue 14, Pages 1615-1624.
19. L. Ozgener, A. Hepbasli, I. Dincer, Energy and exergy analysis of the Gonen geothermal district heating system, Turkey, Geothermic, Vol. 34, 2005, Issue 5, Pages 632-645.

20. I. Dincer, Exergy as a potential tool for sustainable drying systems, Sustainable Cities and Society, Vol. 1, 2011, Pages 91–96.
21. Y. Haseli, I. Dincer, G. Naterer, Optimum temperatures in a shell and tube condenser with respect to exergy,International Journal of Heat and Mass Transfer,Vol. 51, 2008, Issue 9-10, Pages 2462-2470.
22. F. Orhan, I. Dincer. M. Rosen., "An exergy–cost-energy-mass analysis of a hybrid copper-chlorine thermochemical cycle for hydrogen production", International Journal of Hydrogen Energy,Vol. 35, 2010, Issue 10, Pages 4831-4838.
23. Deng-Chern S., Chia-Chin C.,"Engineering design and exergy analyses for combustion gas turbine based power generation system", Energy, Vol. 29, 2004, Issue 8, Pages 1183-1205.
24. Y. Haseli, I. Dincer. G. Naterer, Thermodynamics analysis of a combined gas turbine power system with a solid oxide fuel cell through exergy, Thermochimica Acta,Vol. 480, 2008, Issues 1 -2, Pages 1-9.
25. Y. Huangfu, J. Wu, R. Wang, Z. Xia, Experimental investigation of adsorption chiller for Micro-scale BCHP system application, Energy and buildings, Vol. 39, 2007, Pages120-127.
26. M. Tatiana, G. Tsatsaronis, Advanced Exergy Analysis for Chemically Reacting Systems – Application to a Simple Open Gas-Turbine System, International Journal of Thermodynamics, Vol. 12, 2009, Pages 105-111.
27. M. Ebrahimi, A. Keshavarz, A. Jamali, Energy and exergy analyses of a micro-steam CCHP cycle for a residential building. Energy and Buildings, Vol. 45, 2012, Pages 202-210.
28. A. Khaliq, Exergy analysis of gas turbine trigeneration system for combined production of power heat and refrigeration, International Journal of Refrigeration, Vol. 32, 2009, Pages 534-545.
29. G. Tsatsaronis, M. Moran, Exergy-aided cost minimization, Energy Conversion and Management, Vol. 38, 1997, Pages 1535-1542.
30. I. Dincer, M. Rosen, Exergy: Energy, Environment and Sustainable Development, Elsevier, First Edition, Pages 1-14, 2007.
31. L. Gao, H. Jin, Z. Liu, D. Zheng, Exergy analysis of coal-based polygeneration system for power and chemical production, Energy, Vol. 29, 2004, Pages 2359-2371.
32. Azouma, Y. Blin, J. Daho, T., "Exergy efficiency applied for the performance optimization of a direct injection compression ignition (CI) engine using biofuels", Renewable Energy, Vol. 34, 2009, Pages 1494–1500.
33. F. Sarhaddi, S. Farahat, H. Ajam, A. Behzadmehr, Perform exergetic optimization of solar photovoltaic thermal (PV/T) air collector, International journal of energy research, Vol. 35, 2011, Pages 813-827
34. M. Wolf, Performance analysis of combined heating and photovoltaic powers systems for residence, Energy conversion and management, Vol. 16, 1976, Pages 79-90.
35. A.S Joshi, A. Tiwari, Energy and exergy efficiencies of a hybrid photovoltaic-thermal (PV/T) air collector, Renewable Energy, Vol. 32, Issue 13, 2007, Pages 2223-2241.
36. A.S Joshi, A. Tiwari, G.N Tiwari, I. Dincer , B.V Reddy, Performance evaluation of a hybrid photovoltaic thermal (PV/T) (glass-to-glass) system. Internal journal of thermal sciences, Vol. 48, 2009, Pages 154-164.
37. S. Dubey, S.C Solanki, A. Tiwari, Energy and exergy analysis of PV/T air collector connected in series, Energy and Building, Vol. 41, Issue 8, 2009, Pages 863-870.

38. F. Sarhaddi, S. Farhat, H. Ajam, A. Behzadmehr, M. Adeli, An improved thermal and electrical model for a solar photovoltaic thermal (PV/T) air collector, Applied Energy, Vol. 87, 2010, Pages 2328-2339.
39. F. Sarhaddi, S. Farhat, H. Ajam, A. Behzadmehr, Exergatic optimization of a solar photovoltaic (PV) array, Journal of thermodynamics Volume 2009 (2009), Article ID 313561, 11 pages.
40. T. Bergene, O.M Lovvik, Model calculations on a flat-plat solar heat collector with integrated solar cells, Sol Energy, Vol. 55, 1995, Pages 453-62.
41. R.K Agerwal, H.P Garg, Study of a photovoltaic-thermal system-thermosyphonic solar water heater combined with solar cells, Energy convers Manage, Vol. 35, Issue 7, 1994, Pages 605-20.
42. T.T Chow, W. He, A.L.S Chan, K.F. Fong, Z. Lin, J. Ji, Computer modeling and experimental validation of a building-integrated photovoltaic and water heating system, Applied thermal Engineering, Vol. 28, Issue 11-12, 2008, Pages 1356-64.
43. T.T Chow, W. He, A.L.S Chan, K.F Fong, Z. Lin, J. Ji, Annual performance of building-integrated photovoltaic/ water –heating system for warm climate application, Applied Energy, Vol. 86, Issue 5, 2009, Pages 1356-64.
44. T. N Anderson, M. Duke, G.L Morrison, J.K Carson, Performance of a building integrated photovoltaic/thermal (BiPVT) solar collector, Sol Energy, Vol. 83, 2009, Pages 445-455.
45. J. Jie, L. Keliang, C. T Tai, P. Gang, H. Hannfeng, Thermal analysis of PV/T evaporator of a solar assisted heat pump, Int. J Energy Res, Vol. 31, Issue 5, 2007, Pages 525-545.
46. J. Jie, L. Keliang, C. T Tai, P. Gang, H. Hannfeng, H. Wei, Distributed dynamic modeling and experiment study of PV evaporator in a PV/T solar assisted heat pump, Int. J Heat Mass Transfer, Vol. 52, 2009, Pages 1365-73.
47. J. Rosell, X. Vallverdu, M.A Lechon, M. Ibanzen, Design and simulation of a low concentrating photovoltaic /thermal system, Energy covers Manage, Vol. 46, 2005, Pages 3034-3046.
48. J.S Conventry, Performance of a concentrating photovoltaic/thermal collector, Sol Energy, Vol. 78, 2005, Pages 211-22.
49. B. Sandnes, J. Rekstad, A photovoltaic/thermal (PV/T) collector with polymer absorber plate: experimental study and analysis model, Sol Energy Vol.72, Issue 1, 2002, Pages 63-73.
50. R. Zakharchenko, L. Licea-Jiménez, S.A. Pérez-García, P. Vorobiev , U. Dehesa-Carrasco, J.F. Pérez-Roblesa, J. González-Hernándeza, Yu. Vorobieva, Photovoltaic solar panel for a hybrid PV/ thermal system, Sol Energy Master Sol cells, Vol.82, Issue 1-2, 2004, Pages 253-261.
51. R. Santbergen, R.J.C Zolingen, Modeling the thermal absorptance factor of thermal/photovoltaic (CPVT) combi-panels, Energy cover Manage, Vol. 48, 2006, Pages: 3572-3581.
52. H.T. Chua, , , H.K. Toh, K.C. Ng, Thermodynamic modeling of an ammonia–water absorption chiller, International Journal of Refrigeration, Volume 25, Issue 7, November 2002, Pages 896–906.
53. B. Kim, J. Park, Dynamic simulation of a single-effect ammonia–water absorption chiller, International Journal of Refrigeration, Volume 30, Issue 3, May 2007, Pages 535–545.
54. B. L. Lostec, N. Galanis, J. Millette, Simulation of an ammonia–water absorption chiller, Renewable Energy, Volume 60, December 2013, Pages 269–283

55. N. B. Ezzine, M. Barhoumi, Kh. Mejbri, S. Chemkhi, A. Bellagi, Solar cooling with the absorption principle: first and Second Law analysis of an ammonia—water double-generator absorption chiller , Desalination, Volume 168, 15 August 2004, Pages 137–144
56. B. L. Lostec , N. Galanis, J. Millette, Experimental study of an ammonia-water absorption chiller, International Journal of Refrigeration, Volume 35, Issue 8, December 2012, Pages 2275–2286.
57. W. Wu, B. Wang, W. Shi, X. Li, An overview of ammonia-based absorption chillers and heat pumps, Renewable and Sustainable Energy Reviews, Volume 31, March 2014, Pages 681–707.
58. F. Barbir, PEM electrolysis for production of hydrogen from renewable energy sources, Solar Energy, Volume 78, Issue 5, May 2005, Pages 661–669.
59. M. Ni, M. K.H. Leung, D. Y.C. Leung, Energy and exergy analysis of hydrogen production by a proton exchange membrane (PEM) electrolyzer plant, Energy Conversion and Management, Volume 49, Issue 10, October 2008, Pages 2748–2756.
60. P. Ahmadi, I. Dincer, M. A. Rosen, Energy and exergy analyses of hydrogen production via solar-boosted ocean thermal energy conversion and PEM electrolysis, International Journal of Hydrogen Energy, Volume 38, Issue 4, 12 February 2013, Pages 1795–1805.
61. T.A.H. Ratlamwala, I. Dincer, M. Aydina, Energy and exergy analyses and optimization study of an integrated solar heliostat field system for hydrogen production, International Journal of Hydrogen Energy, Volume 37, Issue 24, December 2012, Pages 18704–18712.
62. K. Deb, A. Pratap, S. Agarwal, T. Meyarivan, A Fast and Elitist Multiobjective Genetic Algorithm: Nsga-II IEEE, Transactions On Evolutionary Computation, Vol. 6, No. 2, April 2002.
63. K. Deb, Multiobjective Optimization Using Evolutionary Algorithms. Chichester, U.K.: Wiley, 2001.
64. C. M. Fonseca, P. J. Fleming, "Genetic algorithms for multiobjective optimization: Formulation, discussion and generalization," in Proceedings of the Fifth International Conference on Genetic Algorithms, S.Forrest, Ed. San Mateo, CA: Morgan Kauffman, 1993, Pages 416–423.
65. J. Horn, N. Nafploitis, and D. E. Goldberg, "A niched Pareto genetic algorithm for multiobjective optimization," in Proceedings of the First IEEE Conference on Evolutionary Computation, Z. Michalewicz,Ed. Piscataway, NJ: IEEE Press, 1994, Pages 82–87.
66. N. Srinivas, K. Deb, "Multiobjective function optimization using nondominated sorting genetic algorithms," Evol. Comput., Vol. 2, No.3, 1995, Pages 221–248,.
67. E. Zitzler, L. Thiele, Multiobjective optimization using evolutionary algorithms — A comparative case study, Vol. 1498, June 2006, Pages 292-301.
68. G. Rudolph, Evolutionary search under partially ordered sets, Computer Methods in Applied Mechanics and Engineering, 2001.
69. K. Deb, An efficient constraint-handling method for genetic algorithms, Comput. Methods Appl. Mech. Eng., Vol. 186, No. 2–4, 2000, Pages 311–338.
70. K. Deb and R. B. Agrawal, "Simulated binary crossover for continuous search space," in Complex Syst., Vol. 9, Apr. 1995, Pages 115–148.
71. T. Ray, K. Tai, C. Seow, An evolutionary algorithm for multiobjective optimization, Eng. Optim., Vol. 33, No. 3, 2001, Pages 399–424.
72. M. Tanaka, GA-based decision support system for multicriteria optimization, In Proc. IEEE Int. Conf. Systems, Man and Cybernetics-2, 1995, Pages 1556–1561.

73. M. Iqbal, An introduction to solar radiation. Toronto: Academic press, 1983.
74. L.T. Wong, W.K. Chow, Solar radiation model, Applied Energy, Volume 69, 2001, Pages 191-224.
75. C. D. Ahrens, Meteorology Today. An Introduction to Weather, Climate, and the Environment. Eighth Edition. Thompson, Brooks/Cole. United States, 2006.
76. H. Akbari, A. Desjarlais, Cooling down the house: residential roofing products soon will boast "cool" surfaces, Journal Professional Roofing, 2005, Pages 32-38.
77. P. Berdahl, S.E. Bretz. Preliminary, Survey of the Solar Reflectance of Cool Roofing Materials, Energy and Buildings, Vol. 25, 1997, Pages 149-158.
78. J. A. Clarke, Energy Simulation in Building Design, 2nd Ed. Butterworth Heinemann: Oxford, 2001, ISBN-13: 978-0750650823.
79. T. l. Jackson, J. J. Feddema, K. W. Oleson, G. B. Bonan, J. T. Bauer, Parameterization of urban characteristics for global climate modeling, Annals of the Association of American Geographers Special Issue on Climate Change, 2010.
80. R. Levinson and A. Hashem. Effects of Composition and Exposure on the Solar Reflectance of Portland cement Concrete. Lawrence Berkeley National, 2001.
81. T. Muneer, Solar Radiation and Daylight Models for the Energy Efficient. Second edition. Elsevier Press, 2004, ISBN-13: 978-0750624954.
82. T. R. Oke, Boundary Layer Climates, 2nd edition. Methuen: New York, 2001, ISBN-13: 978-0415043199.
83. B. E. Psiloglou and H. D. Kambezidis, Estimation of the ground albedo for the Athens area, Greece, Journal of Atmospheric and Solar-Terrestrial Physics, Volume 71(8-9), 2009, Pages 943.954.
84. D. Thevenard, K. Haddad, Ground reflectivity in the context of building energy simulation, Energy and Buildings, Volume 38, Issue 8, 2006, Pages 972-980.
85. UCSB library. Material Emissivity. Institute for Computational Earth System Science, University of California, Santa Barbara. http://www.icess.ucsb.edu/modis/EMIS/html/em.html
86. A. Parkinson, C. Sorensen, N. Pourhassan, A General Approach to Robust Optimal Design, Journal of Mechanical Design, Vol. 115, 1993, Pages 74-80.
87. X. Gu, J. E. Renaud, 2002, Implementation Study of Implicit Uncertainty Propagation (IUP) in Decomposition-Based Optimization, AIAA-2002-5416, Proceedings of the 9th AIAA/ISSMO Symposium on Multidisciplinary Analysis and Optimization Conference, Atlanta, Georgia, Sep. 4-6.
88. X. Du, W. Chen, A Methodology for Uncertainty Propagation and Management in Simulation-Based Systems Design, AIAA Journal, Vol. 38, Issue 8, 2000, Pages 1471-1478.
89. X. Gu, J. E. Renaud, C. L. Penninger, Implicit Uncertainty Propagation for Robust Collaborative Optimization, Journal of Mechanical Design, Vol. 128, Issue 4, 2006, Pages 1001-1013.
90. A. Saltelli, S. Tarantola, K. Chan, A Role for Sensitivity Analysis in Presenting the Results from MCDA Studies to DMs, Journal of Multi-Criteria Decision Analysis, Vol. 8, Issue 3, 1999, Pages 139-145.
91. A. Balbas, M. Ballvé, P. J. Guerra, Sensitivity in Multi-Objective Programming under Homogeneity Assumptions, Journal of Multi-Criteria Decision Analysis, Vol. 8, Issue 3, 1999, Pages 133-138.

92. W.D. Wu, S. S. Rao, Uncertainty Analysis and Allocation of Joint Tolerances in Robot Manipulators Based on Interval Analysis, Reliability Engineering & System Safety, Vol. 92, Issue 1, 2007, Pages 54-64.
93. S. Ferson, L. R. Ginzburg, Different Methods Are Needed to Propagate Ignorance and Variability, Reliability Engineering & System Safety, Vol. 54, Issue 2-3, 1996, Pages 133-144.
94. S. Ferson, R. B. Nelsen, J. Hajagos, D. J. Berleant, J. Zhang, W. T. Tucker, L. R.Ginzburg , W. L. Oberkampf, "Dependence in Probabilistic Modeling, 181 Dempster-Shafer Theory, and Probability Bounds Analysis," Sandia National Laboratories, 2004, SAND2004-3072, Albuquerque, NM.
95. A. Saltelli, K. Chan, E. M. Scott, Sensitivity analysis, John Wiley & Sons, New York, USA, 2000, ISBN: 978-0-470-74382-9.
96. J. C. Helton, F. J. Davis, Latin Hypercube Sampling and the Propagation of Uncertainty in Analyses of Complex Systems, Reliability Engineering & Systems Safety, Vol. 81, Issue 1, 2003, Pages 23-69.
97. H. Simon, Models of Man. J. Wiley & Sons, Chichester, New York, 1957.
98. S. Sundaresan, K. Ishii, D. R. Houser, A robust optimization procedure with variations on design variables and constraints, Advances in Design Automation, Vol. 1, 1993, Pages 379-386.
99. W. Chen, J.K. Allen, K.L Tsui, F. Mistree, A procedure for robust design: minimizing variations caused by noise factors and control factors, ASME Journal of Mechanical Design, Vol. 118, 1996, Pages 478-485.
100. D. Bertsimas, D. Pachamanova, M. Sim, Robust linear optimization under general norms, Operations Research Letters, Vol. 32, 2004, Pages 510-516.
101. M. Kalsi, K. Hacker, K. Lewis, A comprehensive robust design approach for decision trade-offs in complex systems design, ASME Journal of Mechanical Design, Vol. 121, 2001, Pages 1-10.
102. K. M. Miettinen, Nonlinear Multiobjective Optimization. New York: Springer. Pesquisa Operacional Print version ISSN 0101-7438 Pesqui. Oper. Vol.32, No.3 Rio de Janeiro Sept./Dec. 2012.
103. O. B. Augusto, F. Bennis, S. Caro, A sensitivity analysis approach. Multiobjective engineering design optimization problems, Vol.32, No.3 Rio de Janeiro Sept./Dec. 2012.
104. M. Makowski, Multi-objective Decision Support Including Sensitivity International Institute for Applied Systems Analysis, Laxenburg, A-2361 Austria., http://www.iiasa.ac.at/~marek/ftppub/MM/eolss_mcma.pdf
105. L. Mian, Single and multidisciplinary applications. Robust optimization and sensitivity analysis with muti-objective genetic algorithms, 2007, PhD Dissertation, Department of Mechanical Engineering, University of Maryland, College Park.